Title

Phase and Shape Evolutions of Ion Beam Synthesized Ge Based Nanostructures

Author

Shin, Swanee

Publication Date

2009

Phase and Shape Evolutions of Ion Beam Synthesized Ge Based Nanostructures

by

Swanee Shin

A dissertation submitted in partial satisfaction of the

requirements for the degree of

Doctor of Philosophy

in

Engineering – Materials Science and Engineering

and the Designated Emphasis

in

Nanoscale Science and Engineering

in the

Graduate Division

of the

University of California, Berkeley

Committee in charge:

Professor Eugene E. Haller, Chair
Professor Daryl C. Chrzan
Professor Tsu-Jae King Liu

Fall 2009

The dissertation of Swanee Shin, titled Phase and Shape Evolutions of Ion Beam Synthesized Ge Based Nanostructures, is approved.

Chair Date

Date

Date

University of California, Berkeley

Fall 2009

Phase and Shape Evolutions of Ion Beam Synthesized Ge Based Nanostructures

by

Swanee Shin

Abstract

Phase and Shape Evolutions of Ion Beam Synthesized Ge Based Nanostructures

by

Swanee Shin

Doctor of Philosophy in Engineering – Materials Science and Engineering

and the

Designated Emphasis in Nanoscale Science and Engineering

University of California, Berkeley

Professor Eugene E. Haller, Chair

Synthesis and characterization of Ge based nanostructures are presented. Ion beam synthesis of pure Ge nanocrystals by $^{74}Ge^{+}$ implantation into a silica matrix is presented and the strategy to narrow the size distribution by controlling the substrate temperature during implantation is discussed. The size distribution of the sputter synthesized Ge nanocrystals is compared with that of ion beam synthesized Ge nanocrystals. Co-implantation of ^{74}Ge and ^{120}Sn forms binary eutectic alloy nanocrystals. The morphology of the nanocrystals is characterized with transmission electron microscopy and the thermodynamic implication of the equilibrium shape is discussed. It is demonstrated that nanocrystals with a metastable state can be formed with a single excimer laser pulse. The detailed structures and crystallinity of both equilibrium and metastable states are characterized using Raman spectroscopy, scanning transmission electron microscopy, and extended x-ray absorption fine structure spectroscopy. Initial composition dependent recovery of the equilibrium crystalline state upon heating of the metastable structure is investigated with *ex-situ* Raman spectroscopy and *in-situ* transmission electron microscopy equipped with a heating stage. The observed temperature tuning range extends from near room temperature to over 500 °C depending on the Sn content, indicating metal mediated lowering of the crystallization temperature. The phase maps of each phase transformation step of the GeSn alloy nanocrystals are shown using energy filtered transmission electron microscopy, and the position shift of the bulk plasmon peak is demonstrated. One dimensional binary eutectic alloy nanostructures, GeAu nanowires, are also synthesized and characterized. In GeAu nanowires, composition dependent post-growth engineering produced various types of morphologies due to the effectively infinite length for atomic diffusion in one direction. The possibility of creating nanostructures with a combination of ion beam implantation and electron beam irradiation is visited and remaining issues are discussed.

Contents

Acknowledgements

I am indebted to a countless number of people during my graduate career at Berkeley. First of all, I would like to thank my advisor Professor Eugene E. Haller. He provided me with continuous support, advices, and encouragements throughout my Ph.D. study, and set a great example as a scientist, a teacher, and a leader. I would also like to give many thanks to Professor Daryl C. Chrzan for his insightful suggestions and guidance for my research, always with plentiful sense of humor, and Dr. Joel W. Ager III for sharing his bright ideas and in-depth experimental knowledge. I appreciate Professor Oscar D. Dubon, Professor Junqiao Wu, Professor Ronald Gronsky, and Professor Tsu-Jae King Liu for serving on my qualifying exam and providing valuable feedback.

Many people contributed directly and indirectly to my research presented in this dissertation. Dr. Ian D. Sharp helped me to adapt myself to new facilities and research topics when I first joined the group. Dr. Chun-Wei Yuan and Cosima N. Boswell raised my level of understanding by providing great models and performing calculations. Peter R. Stone, Julian Guzman and Christopher Y. Liao were always available to give a hand and conduct collaborative experiments.

Dr. Masashi Watanabe at the National Center for Electron Microscopy[*] taught me and helped me in numerous aspects of electron microscopy, and Professor Andrew M. Minor, Dr. Zonghoon Lee, and Chengyu Song were always helpful when I faced equipment related difficulties. Dr. Kin M. Yu provided RBS data with great accuracy and speed, and Jeffrey Beeman performed time-consuming implants for us without losing a smile and a sense of humor under all circumstances.

I would also like to thank other members of the Haller group. Bill Hansen always willingly shared his wisdom and experience and David Hom always took care of my administrative matters with friendly jokes. My fellow graduate students Chris, Julian, Becca, Nate, Rob, Derrick, Marie, Erin, and Karen – they also deserve my special thanks to have maintained a supportive and friendly environment.

My old friends who shared the ups and downs of our graduate years - Chris, Johnny, Kyuoh, Sung, Tomoko, Fatima – it was a great pleasure and comfort to have you guys around. My special thanks go to my church members as well. The leaders of GFC and members of KBSK, you were truly my other half for the past few years.

Most importantly, I can never thank in a few words my parents and Him, for their unconditional love, for their consistent support, for their encouragements, for their prayers… I owe you what I am.

I would like to acknowledge the support from NSF IGERT program. The work was supported in part by the Director, Office of Science, Office of Basic Energy Sciences, Division of Materials Sciences and Engineering, of the U.S. Department of Energy under Contract No. DE-AC02-05CH11231, and in part by U.S. NSF Grant Nos. DMR-0405472 and DMR-0902179.

---

[*] now on the faculty of the Dept. of Mat. Sci. & Eng., Lehigh Univ., Bethelehem, PA

Chapter 1

Introduction

Nanoscale science and engineering have grown in a dramatic pace over the past few decades. Indeed, nanotechnology has existed since the early stage of human history. For example, the glass of the Lycurgus Cup that was made in the 4th century A.D. during the Roman Empire shows different colors depending on the position of the light source; green when seen through reflected light, and red when seen through transmitted light.[1] It was not until late 20th century that people revealed that the mysterious colors originated from the unique optical properties of the Ag-Au alloy nanoparticles embedded in the glass matrix.[2] Later they also found that in order to form such nanoparticles, parameters such as metal concentrations, proportions and oxidation states of the reducing agent, annealing time/temperature/atmosphere have to meet specific conditions, which have not been known to people until recently.

As in the case of Lycurgus Cup, new discoveries in modern physics along with the advancement of nanoscale characterization techniques have led to the emergence of nanoscience. People have found as materials are formed on decreasing length scale, the differences between the bulk and the small structures become increasingly pronounced due to two dominant effects: surface effects and quantum confinement effects. The former effects largely determine the physical and thermodynamic properties of the nanostructures such as melting temperature, phase transformation behavior and bulk modulus.[3-7] The latter influences the behavior of electrons, thus the electronic structure of the materials and have been proposed to be utilized in device applications ranging from nonlinear optical devices[8-10] to charge storage media.[11, 12] Tremendous research efforts have been spent on studying those nanoscale phenomena in one dimensionally confined quantum wells and superlattices,[13, 14] two dimensionally confined nanotubes and nanowires,[15-18] and all three dimensionally confined quantum dots and nanocrystals.[19-22]

Among the various materials candidates for forming nanostructures, group IV based materials are particularly attractive because they are compatible with the most popular current semiconductor technologies, are nontoxic, and are relatively inexpensive. Ge nanocrystals, in particular, have been proposed for both optoelectronic and non-volatile memory applications. Ge has a large excitonic Bohr radius compared to Si, which means stronger quantum confinement effects,[23] and it makes it a promising material for highly tunable light emission material. As an application for non-volatile memory, Ge or Si nanocrystals have been proposed to replace the floating gate in conventional flash memories as the charge storage medium.[11, 24, 25] By using discrete nanocrystals charge storage, the retention time could be prolonged while the tunneling oxide thickness can be reduced to increase the write/erase speed.

Ge based materials have been extensively studied for applications in another types of non-volatile memory, phase change memory, and media for optical data storage devices.[26] The typical materials widely in use are the alloy family of $Ge_2Sb_2Te_5$. In those devices, one material state transforms rapidly into the other using, for example, a tailored current or laser pulse, and resulting in a phase with markedly different optical or electrical properties.[27] The schematic structures and operating principles are displayed in Fig. 1.1.

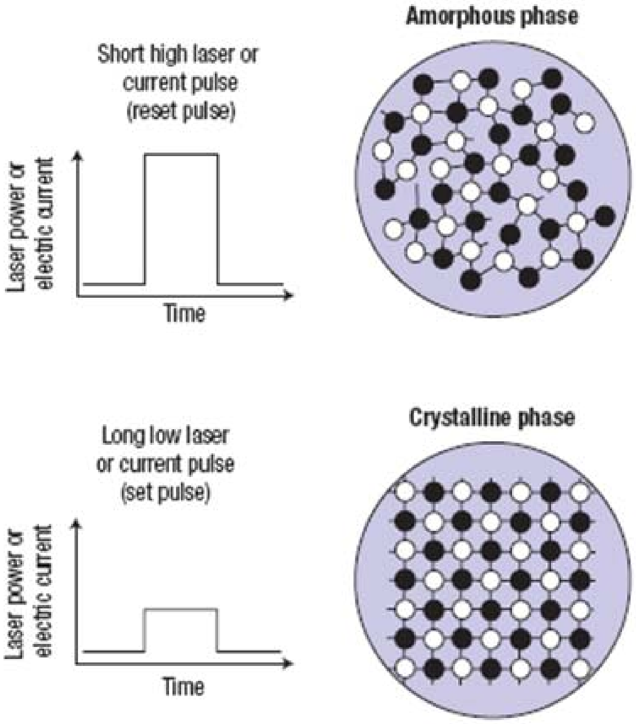

Figure 1.1. The concept of rewritable optical data storage and non-volatile memory using phase change materials.[26]

There is a substantial current research effort dedicated to understanding existing phase change materials,[28-31] and to identify new materials with improved properties. The focus of those studies is mostly on identifying the properties that make a single, bulk material suitable for phase change applications. However, as the dimensions of the devices become smaller, not only the precise understanding of the nanoscale phenomena is essential, but the motivation to take advantage of those unique characteristics is highly desirable.

In this dissertation, the phase change behaviour of the Ge based nanostructures fabricated mainly by ion beam synthesis is presented. First, the generic ion beam synthesis method is introduced in Chapter 2. The synthesis and characterization of Ge and GeSn nanocrystals embedded in a SiO_2 matrix are shown, and the thermodynamic implications of the alloy nanocrystal shape are discussed. In Chapter 3, phase transformation processes of the ion beam synthesized GeSn alloy nanocrystals are presented focusing on its equilibrium and kinetic aspects. The potential for application of this new concept as a phase change material by tuning the phase equilibria and transition kinetics at the nanoscale is suggested. In Chapter 4, composition dependent post-growth engineering of GeAu nanowires is shown. It produced various shapes of final morphologies, providing an additional knob for nanoscale engineering. In Chapter 5, ion beam and electron beam irradiation effects on nanostructure formation and modification are introduced.

Chapter 2

Synthesis and Structural Characterization of Nanocrystals

2.1. Ion Beam Synthesis

2.1.1. Ion Implantation

Ion implantation itself is a very broad topic. When restricted to artificially induced implantation of ions, it is believed to have been first performed by Rutherford in 1906, when he bombarded an aluminum foil with α-particles.[32] Other types of ion implantation include gas discharge equipment, ion sources producing a focused ion beam, both normally work at energies up to 5 keV, and an ion source followed by an accelerator used for metal surface treatment at higher energies. Ion implantation is widely used in semiconductor device manufacturing where it requires very precise parameter control. Shockley first filed his patent for "forming semiconductive devices by ionic bombardment" in 1954,[33] and defined the necessary equipment requirements for the ion implantation step: mass separation, electrical and mechanical scanning systems, the writing beam implanter and the mask projection implanter. Many accelerators and separators previously used in nuclear research already existed and could be used for the early stages of semiconductor research. Since then, ion implantation technology has advanced in a fast pace both in industry and research applications from doping to irradiation studies, smart cut techniques, and nanostructure formation.

2.1.2. Ion Beam Synthesis Procedure

Ion implantation followed by high temperature annealing, called ion beam synthesis (IBS) offers a promising approach to create metallic and semiconducting nanostructures. Since the first attempt by Arnold et al.[34] in 1977 to form Ag and Au nanocrystals embedded in a glass matrix, IBS related research has exploded in 1990s. The major attractive points of this method are its flexibility and compatibility. Essentially any element in the periodic table can be implanted into any host matrix as long as the source materials are practically available. This allows an extremely large range of nanostructure-host matrix combinations. Also, an ion implanter inherently acts as a mass spectrometer, therefore isotopically controlled implantation and nanostructure formation can be achieved. It is a unique advantage of the IBS method that it can be used for a variety of applications such as the formation of pn junctions at a nanoscale. Finally, ion implantation is already widely used in the semiconductor manufacturing industry for doping, so it is very compatible with existing production lines and other device processing steps.

In the present study, the IBS method was implemented to synthesize Ge and GeSn alloy nanocrystals embedded in an amorphous SiO_2 matrix. First, 500 nm thick SiO_2 layers were commercially grown (Process Specialties Inc.) on (100) Si wafer in a chemical vapor deposition (CVD) reactor. Then isotopically pure Ge and Sn were implanted into the grown SiO_2 layers. Natural Ge and Sn exist as 5 and 9 different stable isotopes, respectively as listed in Table 2.1. The most abundant isotopes, ^{74}Ge and ^{120}Sn, were selected for implantation because they produce the largest ion flux, thus can minimize the implantation time for the required doses. The Ge and Sn concentration distribution were predicted using the Trapping Range of Ions in Matter (TRIM) Monte Carlo software package[35] prior to implantation, and energies were selected based on that result. Implantation was performed using a Varian CF 3000 implanter. Germanium tetrafluoride (GeF_4) and Tin Chloride ($SnCl_2$) mixed with Ar as a plasma source were used as ^{74}Ge and ^{120}Sn ion sources, respectively. The samples were mounted on a water cooled stage and were kept effectively at room temperature (RT) during implantation unless otherwise stated. (Chapter 2.3.2)

Ge isotopes	Abundance (atomic %)	Sn isotopes	Abundance (atomic %)
^{70}Ge	20.38	^{114}Sn	0.66
^{72}Ge	27.31	^{115}Sn	0.34
^{73}Ge	7.76	^{116}Sn	14.54
^{74}Ge	36.72	^{117}Sn	7.68
^{76}Ge	7.83	^{118}Sn	24.22
		^{119}Sn	8.59
		^{120}Sn	32.58
		^{122}Sn	4.63
		^{124}Sn	5.79

Table 2.1. Atomic abundance of natural Ge and Sn. [36]

For post-implantation annealing, semiconductor grade quartz ampoules (purchased from GM Associates Inc.) were used. They consist of two parts- one larger tube (1.2 cm O.D., 1.0 cm I.D.) to contain the samples and one smaller plug (0.9 cm O.D., 0.7 cm I.D.) to seal with the larger one afterwards. Both parts were closed on one end, and open on the other end (see Fig 2.1.) They were thoroughly cleaned with acetone and DI water, etched with 5% HF for 2~3 min, then rinsed with DI water and methanol to prevent contamination from the ampoules during high temperature annealing. The samples were also cleaned with boiling xylene, warm acetone, and methanol for 2~3 min each, dried by blowing N_2 before being placed in the ampoule to remove possible surface contamination. The ampoule/sample/plug assembly was then connected to a turbomolecular pump system and was pumped down until the base pressure reached values below 10^{-5} Torr. (> 4 hrs) Once it reached the base pressure, the assembly was slightly heated with a hydrogen torch to outgas remaining moisture and solvents from the ampoule/plug, and was pumped for 10 more min. Finally, the assembly was isolated from the pump system, backfilled with Ar for better heat conduction, and the inner wall of the ampoule was sealed with the outer wall of the plug with a hydrogen/oxygen torch.

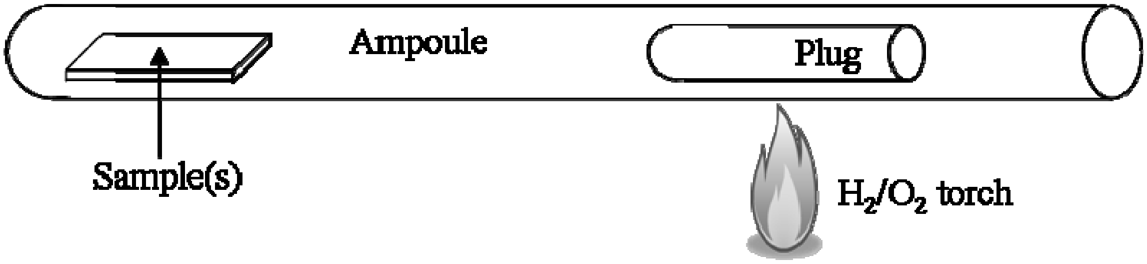

Figure 2.1. Schematic diagram of the ampoule/plug system for furnace annealing

Annealing was performed in a tube furnace (Lindbergh/Blue HTF55322A) at 900°C for 1 hour, and the sample was manually taken out of the furnace and quenched to room temperature under running cold water.

To verify the Ge/Sn concentration profiles after implantation compared with the original TRIM calculation and monitor any changes in the atomic distribution during thermal annealing, Rutherford Backscattering Spectrometry (RBS) measurements were performed before and after annealing. The raw data were obtained and processed by Dr. Kin Man Yu of the Materials Sciences Division (MSD) at Lawrence Berkeley National Laboratory (LBNL) using a 1.92 MeV He^+ beam generated from a 2.5 MeV single ended Van de Graaff accelerator. The sample was typically mounted at an angle of 50° to the beam normal to improve depth resolution, and the backscattered ions were collected at 165° with a Si detector.

Fig 2.2. shows the Ge and Sn profiles after sequential implantation of ^{74}Ge and ^{120}Sn, and after annealing at 900°C for 1hour. ^{74}Ge was implanted at 150 keV, and ^{120}Sn at 120 keV with a target dose of 4×10^{16} cm^{-2} and 1×10^{16} cm^{-2}, respectively. The total integrated concentrations are 3.8×10^{16} cm^{-2} for ^{74}Ge and 8.5×10^{15} cm^{-2} for ^{120}Sn, and the changes after annealing is minimal. The losses of ~10% of the implanted ions are thought to have bombarded to the surface atoms of the SiO_2 layers and contributed to the sputter loss of SiO_2 surface. A certain amount of sputter loss is inherent in the implantation process, yet the actual amount at the current implantation dose level was empirically proven to be small. (<10 nm). One thing to note is that there is a slight shift of the Ge profile toward the surface after annealing, which was not observable for Ge-only implantation. It is due to the diffusion of Ge atoms when they form nanocrystals, in this case GeSn mixture. We can therefore infer that the presence of Sn lowers the chemical potential of that region (~70 nm in depth) and drive the diffusion of the Ge atoms and form GeSn alloy nanocrystals. The results and the involved thermodynamic aspects will be discussed in Chapter 2.4., and the principles and analysis of the RBS data are described in appendix A. in more detail.

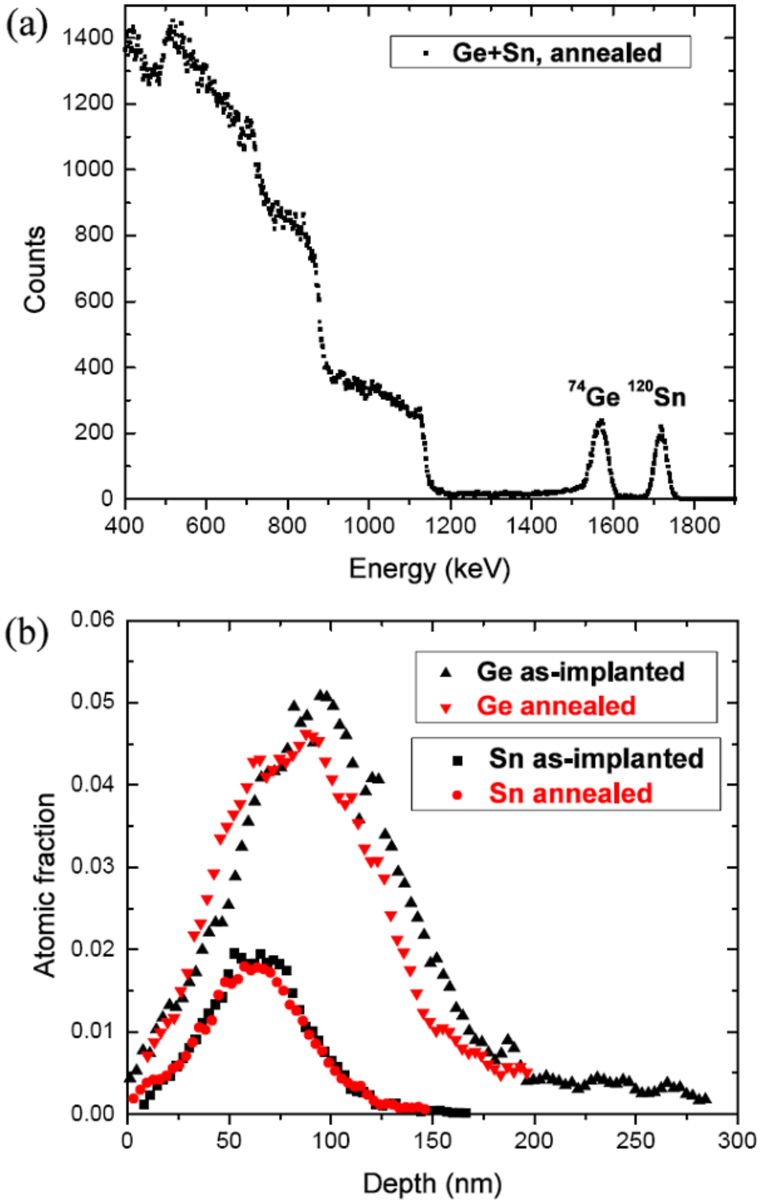

Figure 2.2. (a) Raw RBS spectrum of 500 nm thick SiO_2 layers implanted with ^{74}Ge and ^{120}Sn at 150 keV, 4×10^{16} cm^{-2} and 120 keV, 1×10^{16} cm^{-2}, respectively and annealed at 900°C for 1hour. (b) Processed ^{74}Ge and ^{120}Sn distribution profiles before (as-implanted) and after (annealed) annealing.

2.2. Sputtering

An alternative method to synthesize nanocrystals is through sputtering.[37-40] It involves sputtering of either the desired element (e.g. Ge) alone between sputtered matrix layers (e.g. SiO_2) or co-sputtering of both materials. Nanocrystals are formed in the sputtered layers by thermal annealing above 900°C in an inert atmosphere. They are formed because there are concentrations of deposited element(s) above the solubility limit in the desired layers. The elements precipitate out of the supersaturated layers, forming nanocrystals. The size of the crystals can be roughly controlled by the thickness of deposited elemental layers or the ratio of the sputtered element to matrix material target area or the gas mixture used to form the plasma. In general, for a planar array of nanocrystals, the diameters of the nanocrystals are approximately the same as the thickness of the deposited layer provided the deposited layer thickness is within a few nanometers. Along the same idea, the aerial density of the nanocrystals can be tuned by varying the element to matrix ratio while depositing the active nanocrystal layer. For 3 dimensional arrays of nanocrystals, a relatively thick film of element and matrix material mixture is grown. In this case, the size and volume density of nanocrystals are governed by the concentration of the supersaturated element material(s) and the following annealing conditions that affect the effective diffusion length of individual atom. Although precise control of the size and density of nanocrystals by sputtering is still not fully achieved, this method offers the advantage of simplicity, high throughput, and low cost.

As part of the nanocrystals synthesis study, sputtering method was pursued to synthesize 3 dimensional arrays of Ge nanocrystals embedded in co-sputtered SiO_2 matrix as an alternative or complementary to the IBS method. 5 mm × 5 mm natural Ge pieces were attached to a 12” silica target using a silver epoxy, and Ge/SiO_2 was co-sputtered on a Si wafer (Perkin-Elmer sputtering system model 2400). Pure Ar gas was used as a plasma source with varying background pressure from 40 mTorr to 80 mTorr. The sputtered samples were annealed at temperatures above 900°C either in a tube furnace for 1 hour or in a rapid thermal annealing (RTA) system (AG Associates Heatpulse 210) for 2 min under flowing dry nitrogen.

2.3. Ge Nanocrystals Size Distributions

2.3.1. Sputtered Ge Nanocrystals

Structure and size distributions of ion beam synthesized Ge nanocrystals both exposed and embedded in a SiO_2 matrix have been extensively characterized by a former graduate student Ian Sharp.[41, 42] The same methods were used to characterize the size distribution of Ge nanocrystals synthesized by sputtering deposition.

Ge nanocrystals synthesized by Ge/SiO_2 co-sputtering at 300 W power and a 40 mTorr pure Ar plasma atmosphere, as described in the previous section, were characterized by AFM and Raman spectroscopy. Annealing was performed in a tube furnace at 900°C and 1000°C. Note that sputtering at 60 and 80 mTorr Ar pressure had been attempted, but no crystalline Ge Raman signals were detected.

Although the Ge nanocrystal formation mechanism in sputtered films is not well understood, it could be related to the initial film stoichiometry, hence bonding types of the Ge atoms. In case of the IBS method where Ge atoms were implanted into a thermally grown pure SiO_2, implanted Ge atoms are less likely to bond with the existing silicon or oxygen atoms in the matrix. Rather, they tend to form small amorphous clusters with other Ge atoms. Ge is chemically more noble than Si.[43] In fact, the total amount of Ge did not changed during annealing, as shown in Fig 2.2. (b), and approximately 70% of the implanted atoms were incorporated in crystalline Ge nanocrystals. For co-sputtering, however, the matrix materials silicon and oxygen are deposited simultaneously with Ge atoms, thus the stoichiometry and bonding type of each atom are determined by the sputter yield of each element and any additional impurities in the system. The stoichiometry of the sputter deposited films at 40, 60 and 80 mTorr Ar pressure before and after 900 °C, 1000 °C 1hour annealing are measured with RBS and the results are presented in Table 2.2. The silicon to oxygen ratios are far from that of thermally grown, stoichiometric SiO_2 or the target material, 1:2 possibly due to residual oxygen incorporation from the chamber or the gas line. It suggests that great portions of Ge atoms are bonded with oxygen atoms and form GeO_x that is stable in the matrix and does not precipitate out when annealed at high temperature. The Ge atoms incorporated as GeO_x, as a consequence, will not contribute to the formation of Ge nanocrystals. Indeed, SiO_2 and GeO_2 are fully miscible. For samples deposited at 60 and 80 mTorr Ar pressure, excess Ge atoms with (Si+Ge):O ratio greater than 1:2 are less than ~5 at% compared with ~15 at% for samples deposited at 40 mTorr, therefore, may not be sufficient to form crystalline nanocrystals. As a result, a 40 mTorr Ar pressure was selected to be the optimal condition for Ge nanocrystal formation by sputtering and the size distribution was characterized by atomic force microscopy (AFM) and Raman spectroscopy.

First, AFM was used to measure the size distribution. In order to make individual nanocrystal accessible to the AFM tip, hydrofluoric acid (HF) etching followed by ultrasonic cleaning was performed. 1:1 ratio 49% HF:H_2O liquid solution was used for etching, then the sample was transferred to a methanol bath for 40 kHz ultrasonic cleaning for 30 min. Ultrasonic cleaning provided enough energy to overcome the attractive van der Waals forces in-between nanocrystals and nanocrystals and the substrate, and left a single sparse layer of non-overlapping nanocrystals on a smooth underlying Si substrate. The root mean square (rms) roughness of the etched substrate is approximately 0.1 nm, therefore, has negligible effects on the measurement

Ar pressure	40 mTorr	60 mTorr	80 mTorr
	Si : Ge : O ratio		
As-deposited	0.44 : 1.1 : 2.0	0.4 : 0.7 : 2.0	0.2 : 0.8 : 2.0
900°C 1hr annealing	0.43 : 1.03 : 2.0	0.5 : 0.78 : 2.0	0.25 : 0.9 : 2.0
1000°C 1hr annealing	0.5 : 1.2 : 2.0	-	0.3 : 0.95 : 2.0

Table 2.2. Si:Ge:O ratios of as-deposited and 900°C, 1000°C 1hour annealed films deposited by SiO_2/Ge co-sputtering. Relative oxygen stoichiometry was fixed to 2 for convenience.

data. AFM (Digital Instruments Dimension 3100) was performed in tapping mode with an etched Si tip with a resonant frequency of approximately 325 kHz and a force constant of 40 N/m. Due to the realistic limit of the tip radius (~10 nm), only the height (z-direction) profile provided accurate size information. Using this method, IBS Ge nanocrystals with the same implantation condition followed by 900°C 1hour annealing were measured to have a mean diameter of 5.1 nm with a full-width at half maximum (FWHM) of 3.4 nm, which were proved to be in an excellent agreement with the TEM results.[41]

The size distributions of sputter deposited Ge nanocrystals obtained by the previously described method are shown in Fig 2.3. For the sample annealed at 900°C, the distribution peak position is at 1.5 nm and the majority of the nanocrystals are smaller than 3 nm. When annealed at 1000°C, a bimodal distribution appears; large nanocrystals peaked at ~5 nm and small ones below ~3 nm. These results suggest a model for nanocrystal formation and size evolution. Contrary to IBS, Ge atoms are less likely to form small clusters at the as-deposited state since incoming atoms do not have high enough energy to penetrate into the substrate and move around by random walk until they form small clusters to lower the local free energy. Rather, they will be homogeneously mixed with the matrix atoms in the film until excess Ge atoms start to precipitate at elevated temperature. A homogeneous distribution of Ge atoms could provide a high density of nucleation sites, and each nucleus goes through a growth and coarsening process. 900°C annealing is believed to be sufficiently high to initiate nucleation and limited growth, but substantial coarsening does not seem to happen at this temperature. 1000°C annealing further provides increased mobility to the Ge atoms and small clusters, and results in significant coarsening. However, there still remains a certain amount of small (< 3 nm) Ge crystallites in the matrix that were probably formed at the initial stage.

To assist the AFM analysis, Raman spectroscopy was used to characterize both samples. Since the Raman spectrum is very sensitive to the bonding type, the crystallinity of the material and the size of the nanocrystals due to the phonon confinement effect,[37, 44-46] Raman spectroscopy is very useful to characterize the size and chemical nature of small Ge nanocrystals (< 5 nm). The Raman spectra are shown in Fig 2.4. Peaks at ~300 cm^{-1} with asymmetric broadening to the lower energy side clearly indicate that crystalline Ge nanocrystals are mostly smaller than 10 nm in diameter, a size to which the phonon confinement effect is applicable. FWHM of the spectrum has increased by 3.9 cm^{-1} from (a) to (b).

A number of attempts have been made to calculate the average size of the nanocrystals from the Raman spectrum alone,[47] but the uncontrolled or unknown parameters, e.g. the uncertainty of the boundary condition to set the phonon weighting function of the nanocrystals,

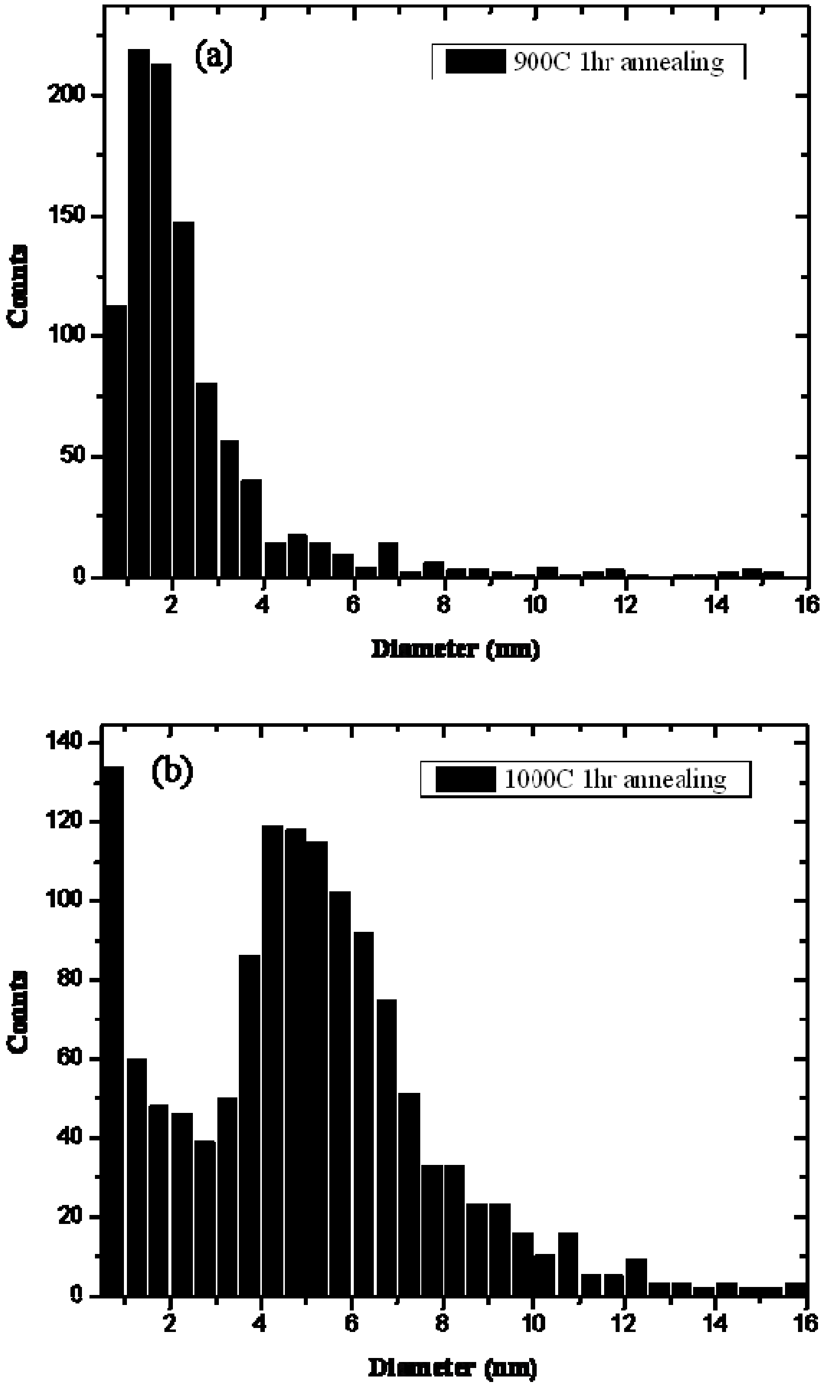

Figure 2.3. Size distribution of sputter deposited Ge nanocrystals obtained by HF etching and ultrasonic cleaning. Annealing was performed at (a) 900°C and (b) 1000°C

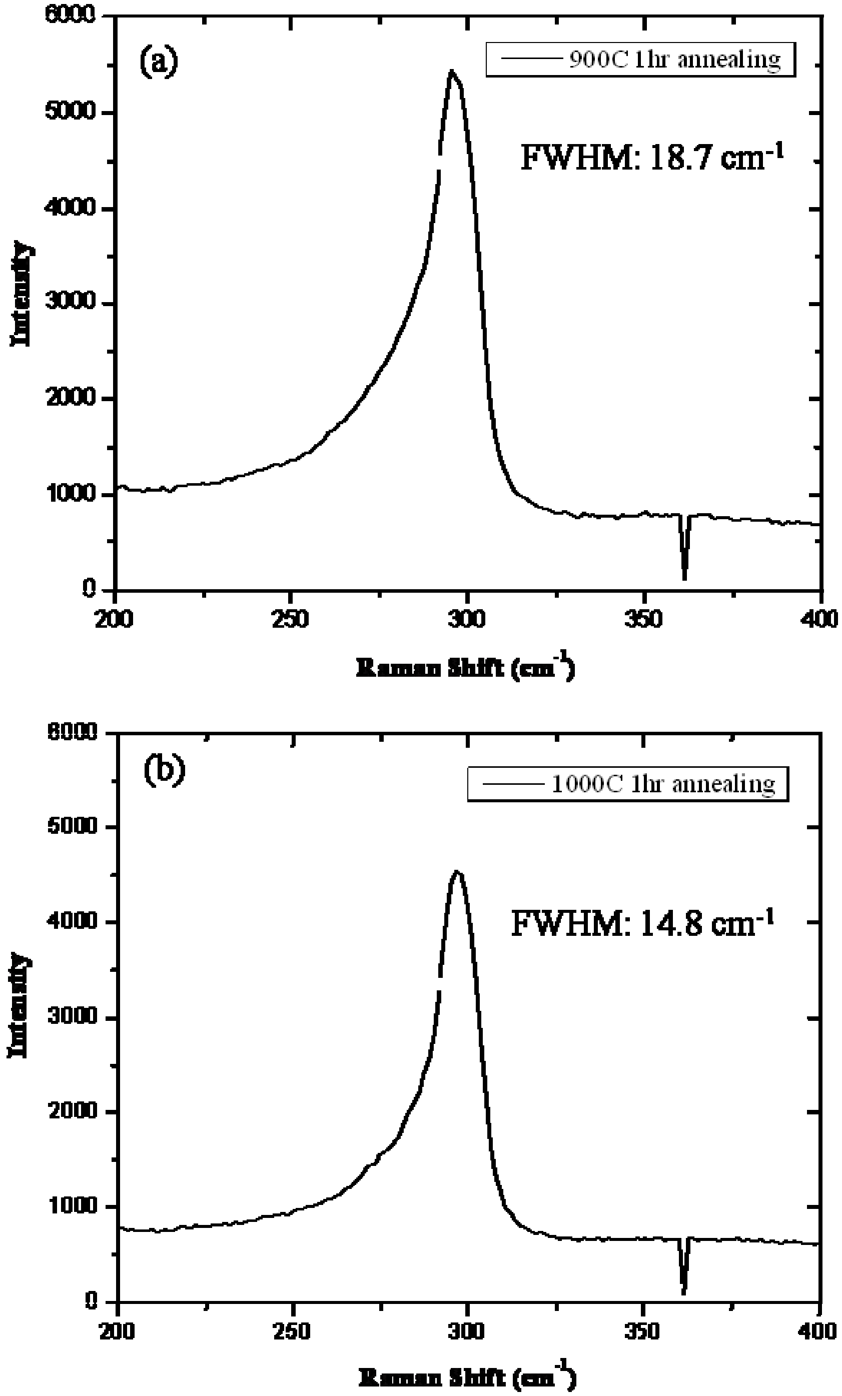

Figure 2.4. Raman spectra of sputter deposited Ge nanocrystals followed by annealing at (a) 900°C and (b) 1000°C for 1 hour each.

the anisotropy of the phonon dispersion curves, and the non-spherical shape of the Brillouin zone, make the solutions non-unique. In addition, light-nanocrystals resonant effect could be different for different size of nanocrystals which may cause sampling problem. As a consequence, only a rough estimate and a comparative statement can be derived from the Raman spectrum alone.

With the same measurement setup, the FWHM of bulk Ge was 11.6 cm^{-1} and IBS Ge nanocrystals (mean diameter 5.1 nm) was 15.0 cm^{-1} which is very close to Fig 2.4.(b) when a sputter deposited sample was annealed at 1000°C. Peak broadening is enhanced when annealed at 900°C, meaning nanocrystals are still significantly smaller than samples annealed at 1000°C. Although still qualitative, the Raman results are very consistent with the size distributions obtained with AFM, and clearly show the existence and strong size effects of the nanocrystals smaller than ~3 nm.

2.3.2. Control of the Ion Beam Synthesized Ge Nanocrystals

Although IBS and sputtering provide easy, convenient ways to produce embedded nanocrystals, both methods bear fundamental limits in the size control. As shown in the previous sections, synthesized nanocrystals have a wide size distribution, which is detrimental for efficiencies of nanocrystals based devices. For example, for precise tuning of the optical bandgap and reliable charge storage, narrowing the size distribution is essential.

As a first step, a comprehensive understanding of the IBS process is required. The final size distribution is governed by the nanocrystal evolution during the implantation process.[48, 49] A theory was developed in our group to understand this process by Dr. Chun-Wei Yuan,[50] a former graduate student of Professor Daryl C. Chrzan. Kinetic Monte Carlo (KMC) simulations and the mean-field self-consistent solution to a set of coupled rate equations showed that nanoclusters size distribution asymptotes to a steady state and the state was governed by two key parameters: the characteristic length, L, and the interface energy, γ, between the implanted species and the matrix. Empirically, γ was found to affect only the average size of the nanoclusters, therefore, when scaled by the average size, the distribution was governed exclusively by L. The characteristic length L was defined as the following:

$$L \equiv \left(\frac{Dn_\infty}{F}\right)^{\frac{1}{2}}, \quad \text{where,} \quad \begin{array}{l} D: \textit{effective diffusivity during implantation} \\ n_\infty: \textit{solubility of the implanted species} \\ F: \textit{volumetric implantation flux} \end{array}$$

When fitting the experimentally measured as-implanted size distribution, an estimate of L could be made. In case of Ge nanocrystals in a SiO_2 matrix, L was estimated to be 1.38 Å, which is 26.4 times larger than the value predicted by using the normal diffusion coefficient. In other words, the estimate of $\frac{Dn_\infty}{F}$ exceeded the expected value by a factor of 700, which could be attributed to the effect of transient enhanced diffusion (TED).[51] Calculations suggest that as L decreases, so does the relative FWHM of the size distribution curve. Experimentally, L can be decreased by either increasing the implantation flux F or decreasing Dn_∞. Practically, it is difficult to modify F in the current experimental setup, therefore, decreasing Dn_∞ by temperature control was selected to be the most appropriate and practical route for decreasing L, thus narrowing the size distribution.

First, a KMC simulation was performed to predict the effect of temperature control. The parameters were chosen that are appropriate for ^{74}Ge implantation into amorphous SiO_2 at 120 keV.[52] F was set to be 1.5×10^{12} cm^{-2} s^{-1}, and the characteristic displacement distance of collision cascades was λ=3.5 Å as determined by TRIM calculations.[50] The temperature dependence of D and n_∞ was assumed to be $D = D_o \exp[-E_m / k_B T]$ and $n_\infty = n_o \exp[-E_b / k_B T]$, respectively, where D_o is the diffusivity at infinite temperature, E_m is the migration energy, k_B is the Boltzmann constant, n_o is the solute site density in the matrix, and E_b is the binding energy. The values used for calculation were D_o = 3.1 cm^2 s^{-1}, E_m = 0.4 eV, n_o = 8.0×10^{-3} Å^{-3}, and E_b = 0.816 eV. With these parameters, the simulated implantation dose-temperature profile is as follows; Ge implantation of N (dose) = 5×10^5 cm^{-2} at liquid nitrogen temperature, linear increase of the temperature up to final temperature T_f in 30 min duration while continuing implantation, and finish the implantation with total dose $N = 4.5\times10^{16}$ cm^{-2}. The simulation results are presented in Fig 2.5. The predicted size distribution is substantially narrower (~20 % of the scaled width) than the typical constant temperature IBS (~70 % of the scaled width), and pure coarsening case. The effect of γ and T_f on the width is almost negligible.

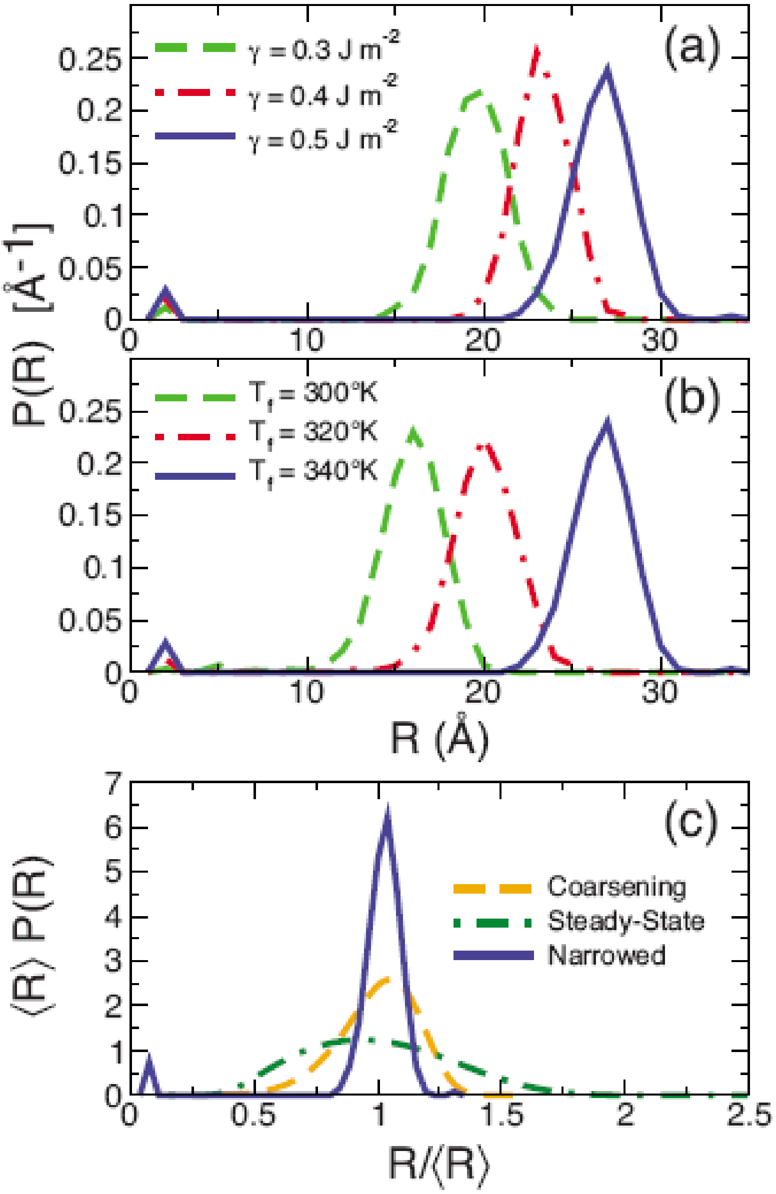

Figure 2.5. IBS clusters size distributions with different (a) γ's and (b) T_f's. (c) A comparison of cluster size distributions predicted by the proposed narrowing process, constant temperature IBS (steady state), and a self-consistent coarsening theory.[52] The integrated area under the curves was set to 1 for all cases.

Second, a set of experiments were performed to verify the temperature effect. In order to minimize the variables in its initial investigation process, a cold implantation process was performed at a fixed liquid nitrogen temperature without increase of the temperature during implantation. Size distribution of the references samples were implanted at room temperature and the post-implantation annealing conditions were identical. The implantation energy and dose were 150 keV, 2×10^{16} cm^{-2}, respectively. The results are shown in Fig. 2.6. The average nanocrystals size increases with higher annealing temperature for both cases, reaching a typical coarsening distribution. One distinction is the distribution between RT implantation with 900 °C annealing and that of cold implantation with 900 °C annealing as shown in Fig. 2.6.(b). Although not very significant, a cold implant distribution resulted in a narrower distribution as compared to the distribution of RT implanted nanocrystals. To better observe this effect and quantify it with more reliability, a set of experiments is in progress with lower annealing temperature and with temperature increase during implantation process as designed in the original simulation.

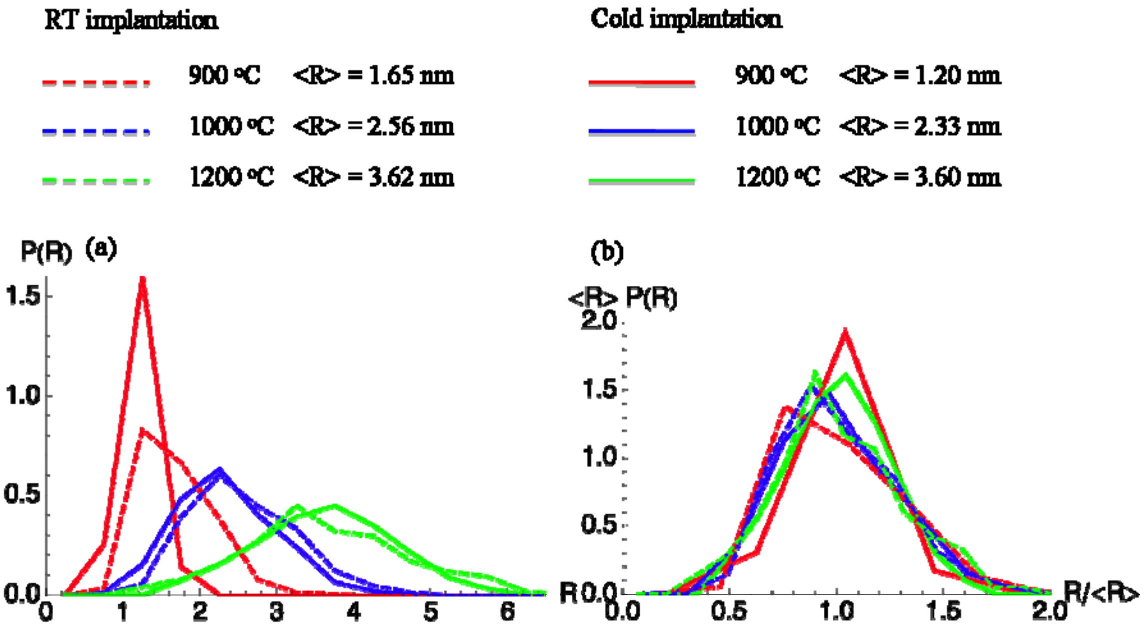

Figure 2.6. Experimental size distributions of Ge nanocrystals. ^{74}Ge was implanted at room temperature and liquid nitrogen temperature followed by annealing at 900, 1000 and 1200 °C for 1 hour.

2.4. GeSn Nanocrystals

2.4.1. Transmission Electron Microscopy

Along with attempts to synthesize and accurately characterize single elemental nanocrystals using the IBS method, significant endeavors have been made to apply IBS to two or more elements to make alloy or compound nanocrystals.[53, 54] There are multiple phases and geometries possible that are determined by the significant surface and interface effects at the nanoscale as well as the inherent bulk properties of the constituent elements.[55, 56]

Among many nanoscale alloy materials, $Ge_{1-x}Sn_x$ alloys, in particular, have been studied intensively as a promising material for light emitting devices due to the reported indirect to direct bandgap transition at $x \approx 0.1$,[57-59] and at the nanoscale, GeSn quantum dots showed a size dependent quantum confinement effect.[60, 61] Additionally, we can expect composition dependent phase transformation behavior for these materials, in a similar way it was demonstrated for phase change materials used for memory device and/or optical storage media. Several nonequilibrium growth methods have been attempted for films[58, 59] and quantum dots,[60, 61] most of which used epitaxial growth on an underlying substrate. Investigations on IBS nanocrystals followed by detailed characterization, however, are lacking. In the present study, the IBS method was used to form GeSn nanocrystals in amorphous SiO_2, and the detailed structure was characterized with transmission electron microscopy (TEM).

Isotopically controlled ^{74}Ge and ^{120}Sn ions were sequentially implanted at room temperature into 500nm thick SiO_2 layers grown commercially on (100) Si wafers via wet oxidation. The energy and dose were selected to be 150 keV, $4\times10^{16}cm^{-2}$ for ^{74}Ge, and 120 keV, $1\times10^{16}cm^{-2}$ for ^{120}Sn, such that the peak positions of the implantation profiles approximately match each other at 80 nm below the surface based on the prediction of the TRIM Monte Carlo calculation. Annealing to form nanocrystals was performed in a tube furnace at 900°C for 1 hour, and the sample was quenched to room temperature under cold running water. Detailed sample preparation procedures are described in Chapter 2.1.

The elemental distribution profiles obtained by RBS were presented in Fig 2.2. It indicated that there was little loss or change in the profiles during the annealing process. To observe directly the synthesized nanocrystals, TEM samples were prepared in both cross sectional and planview geometry,[43] and the images were taken using the 300 kV JEOL 3010 microscope at the national center for electron microscopy (NCEM), Lawrence Berkeley National Laboratory. Fig 2.7. shows the distribution of GeSn nanocrystals in the amorphous SiO_2 matrix. It clearly demonstrates that two phase nanocrystals with bi-lobe shape were formed and the sizes are approximately 10~20 nm in diameter. Note that there also exists a small, single phase nanocrystals deeper (> 100 nm) in the matrix. This is due to the slight offset between ^{74}Ge and ^{120}Sn implantation profiles: the ^{74}Ge profile is peaked at ~90 nm in depth, about 20 nm deeper than the ^{120}Sn peak. The size and composition of each nanocrystal directly reflects these profiles, and as a result, pure Ge nanocrystals with smaller average diameters are formed deeper in the SiO_2, where there are no Sn atoms. We confine our interest to the region near the implantation peaks (~60 nm) where both ^{74}Ge and ^{120}Sn atoms are present.

In order to investigate the crystallinity and the microstructure in more detail, high resolution transmission electron microscope (HRTEM) images were taken with 200 kV FEI Tecnai TF-20. Fig 2.8. (a) and (b) show images from a single nanocrystal taken at slightly different tilt angles to find a zone axis perpendicular to a lattice plane of each phase.

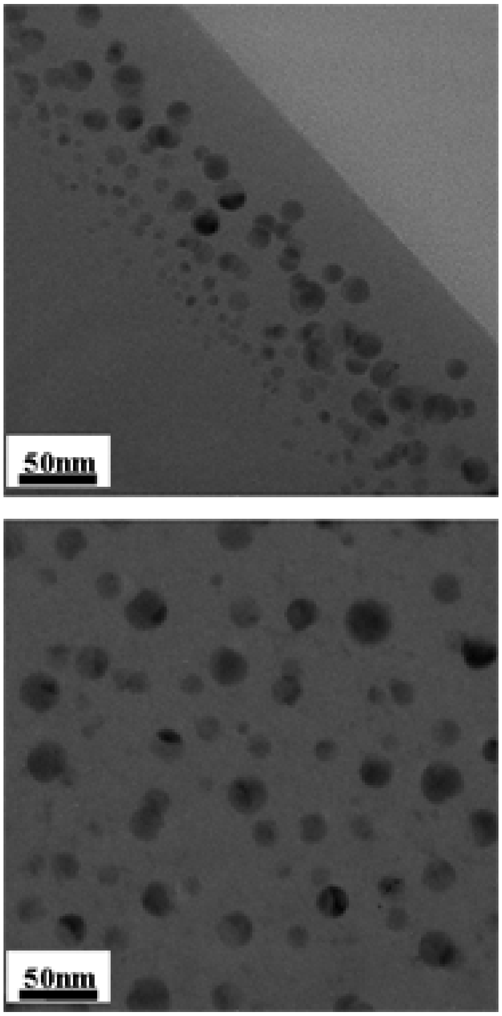

Figure 2.7. Bright field (BF) TEM images of GeSn nanocrystals in (a) Cross sectional, (b) Planview sample geometry. ^{74}Ge was implanted at 150keV with 4×10^{16}cm^{-2} dose and ^{120}Sn at 120keV with 1×10^{16}cm^{-2} dose. Annealing was performed at 900°C for 1 hour.

From the images, each phase is found to be single crystalline, and no defects could be found. Measured interplanar distances of Fig 2.8 (a) (top right phase) and (b) (bottom left phase) are 3.24 Å and 2.00 Å, which respectively correspond to Ge (111) and β-Sn (211) planes. This measurement shows that each phase consists of nearly pure Ge or pure Sn. Also, it appears that the two phases are oriented to cause minimum lattice mismatch at the interface, and thus form almost defect-free single crystalline phases on both sides.

Detailed structural information including phase identification could be obtained using a combination of conventional imaging techniques as shown so far, however, it is not only very limited in coverage (1~2 nanocrystal at a time) but also very time consuming and requires some luck in tilting to the right zone axis. Diffraction, another widely used conventional technique, also has a significant limitation: spatial resolution that is usually defined by the aperture size is limited to the order of microns and not convenient to resolve phases in a single nanocrystal.

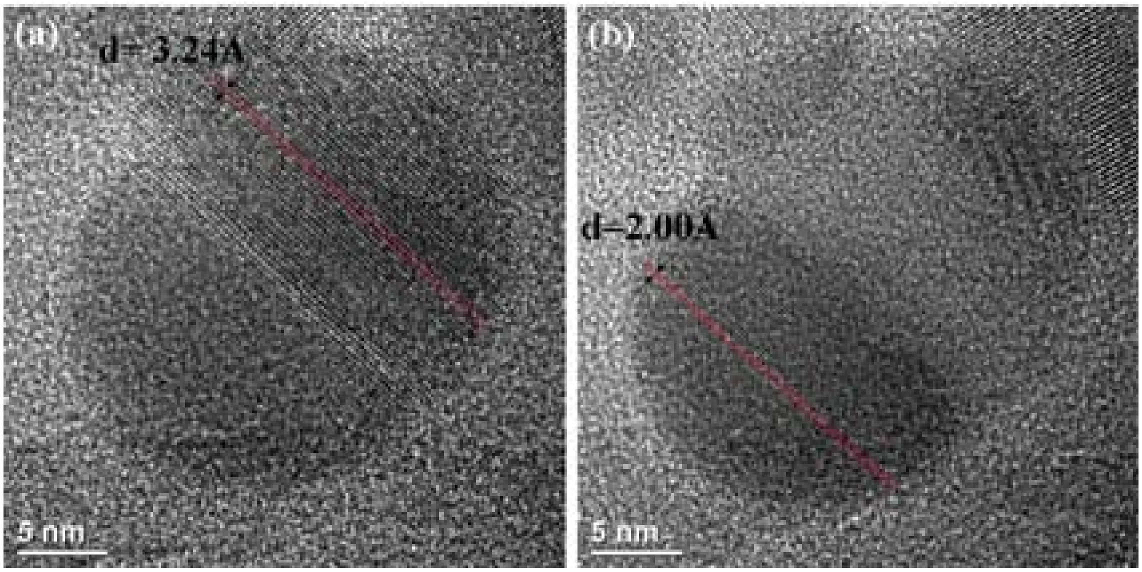

Figure 2.8. HRTEM images of GeSn nanocrystals at slightly different tilt angles. Lattice fringes from (a) Ge (111) planes and (b) β-Sn (211) planes are shown.

Therefore, another complementary TEM mode operating with a different imaging mechanism is introduced; scanning transmission electron microscopy (STEM) with a high angle annular dark field detector (HAADF), often called HAADF-STEM. A schematic of the beam optical column of a HAADF-STEM is presented in Fig 2.9. as compared with conventional TEM, and characteristics of two modes are summarized in Table 2.3. Two main components of HAADF-STEM are deflection coils and a HAADF detector. A convergent beam is scanned on the specimen by adjusting the scan coils, and these same coils are used to scan the CRT or CCD synchronously. The electron detector acts as the interface between the electrons coming from the specimen and the image viewed on the computer screen.[62] The detector is usually placed in a conjugate plane to the diffraction pattern in the same manner an objective aperture is placed directly in the back focal plane of the objective lens. The HAADF detector specifically collects electrons that are incoherently scattered at high angles (> 50 mrad) by Rutherford scattering, of which the number is proportional to the square of the atomic number Z. ($\sim Z^2$). The high collection angle of the HAADF detector prevents contrast contribution from Bragg scattering (diffraction contrast), therefore, it is convenient to use for elemental mapping of randomly oriented crystalline materials as in the current case.

Fig 2.10.(a) shows an equivalent HAADF-STEM image of GeSn alloy nanocrystals as in Fig 2.7.(a) using FEI Tecnai TF-20. Since Ge and Sn are hardly miscible, we readily know that phase separated bi-lobe nanocrystals with Sn (bright, Z=50) and Ge (dark, Z=32) are formed. An X-ray energy dispersive spectrometry (XEDS) line scan across a single bi-lobe nanocrystal was performed using a Philips CM200/FEG, and it confirmed the formation of GeSn binary bi-lobe alloy nanocrystals as shown in Fig 2.10.(b).

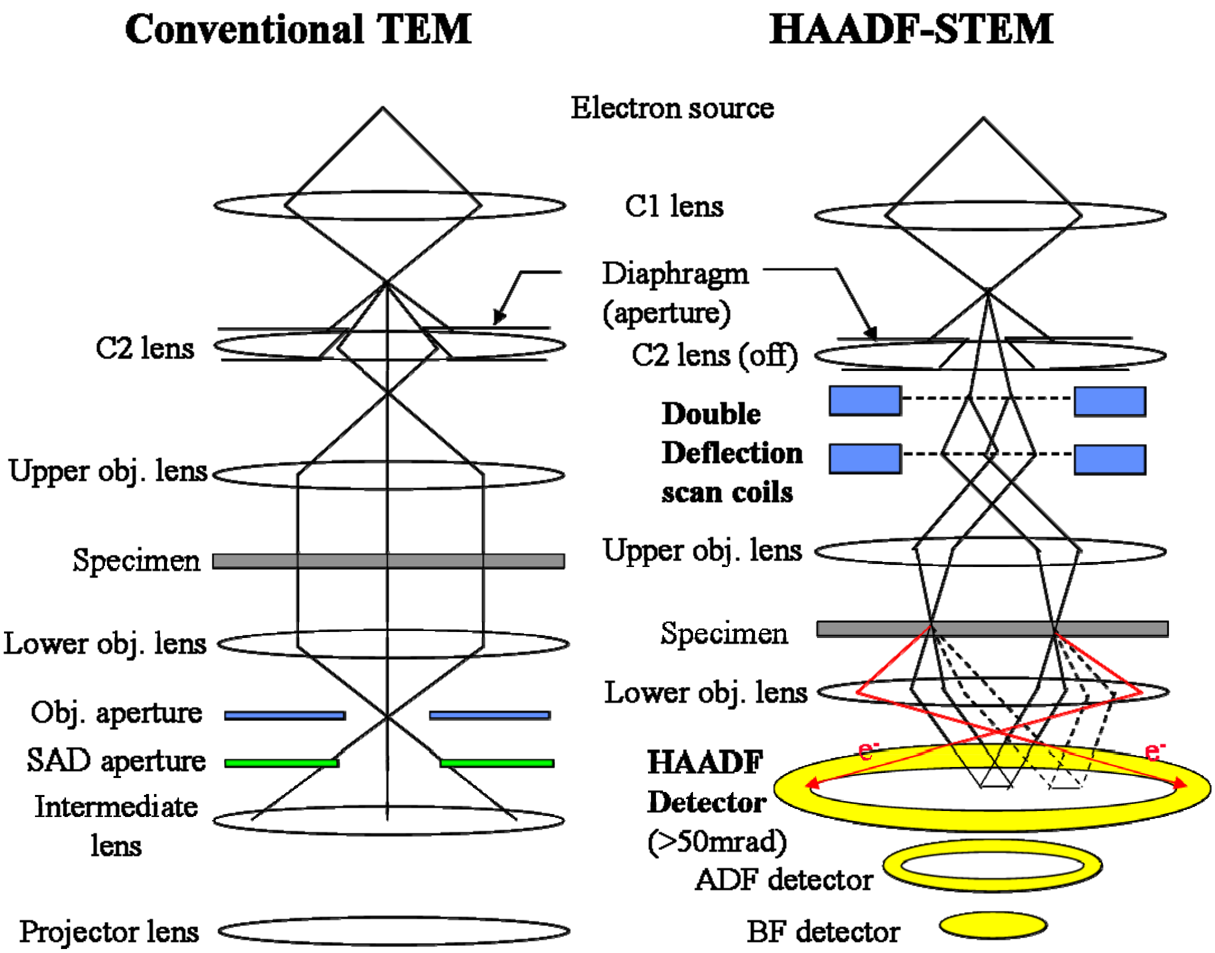

Figure 2.9. Shematic diagrams of the electron beam optical columns of (a) conventional TEM and (b) HAADF-STEM.

	Conventional TEM (BF/DF)	HAADF-STEM
Specimen illumination	Parallel beam	Focused beam (scanning)
Contrast mechanism	Diffraction contrast (Bragg scattering)	Z-contrast (Rutherford scattering)
Information	Sensitive to grain orientation	Sensitive to Z and thickness t

Table 2.3. Comparison of the characteristics of conventional TEM and HAADF-STEM

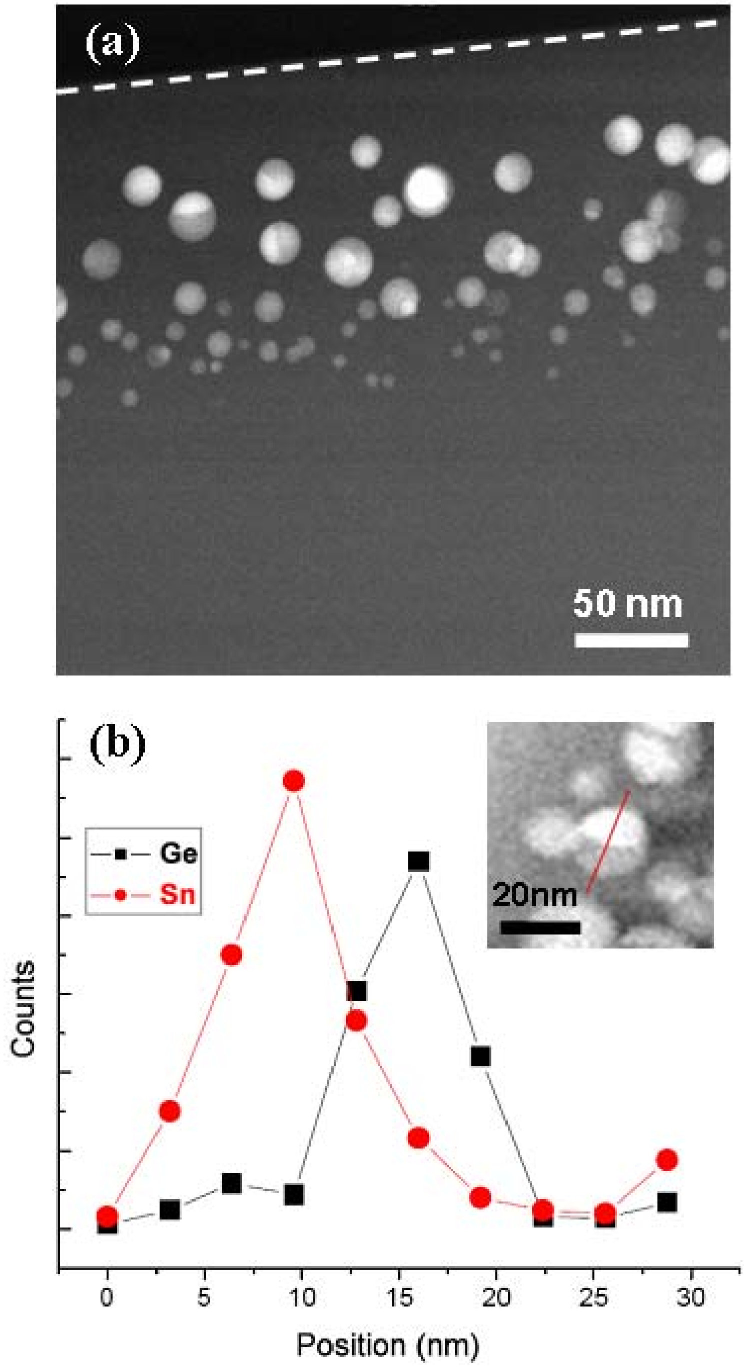

Figure 2.10. (a) Cross-sectional HAADF-STEM image of the GeSn nanocrystals after thermal annealing at 900°C for 1hr. The dotted line indicates the sample surface. (b) XEDS line scan across a single bi-lobe nanocrystal.

2.4.2. Thermodynamic Implications

In order to understand the equilibrium morphology of embedded nanocrystals formed from a strongly segregating binary alloy system, we developed a model to describe it using the relative magnitudes of the interface energies between two adjacent phases, $\gamma_{A/B}$, as governing parameters.[56] The compositions within each phase were assumed to be uniform, all interfaces were assumed to be stress-free and to have isotropic interface energies. The matrix is presumed to enable relaxation to the equilibrium shape. In the model, the free energies of competing structures were computed and compared.

In segregating binary alloy systems, four types of nanocrystal morphologies can be predicted: core-shell, inverse core-shell, two separated nanocrystals, and bi-lobe structures. If we define two phases as α and β and the matrix as M, the total interface energy of two core-shell structures and two separated nanocrystals can be expressed by the following equations:

$$\alpha \text{ core- } \beta \text{ shell: } E_{\alpha c/\beta s} = \sum_i A_i \gamma_i = 4\pi R_0^2 \gamma_{\beta/M} + 4\pi r_0^2 \gamma_{\alpha/\beta}$$

$$\beta \text{ core- } \alpha \text{ shell: } E_{\beta c/\alpha s} = 4\pi R_0^2 \gamma_{\alpha/M} + 4\pi r_0^2 \gamma_{\alpha/\beta}$$

$$\text{Two separated nanocrystals: } E_{sep} = 4\pi r_1^2 \gamma_{\alpha/M} + 4\pi r_2^2 \gamma_{\beta/M}$$

Where, R_0 and r_0 are the radii of the shell and core of the nanocrystals, respectively. r_1 and r_2 are the radii of two separated nanocrsystals.

For bi-lobe nanocrystals, Young's equation and volume conservation law are applied to calculate the total interfacial energy:

$$\gamma_{\alpha/M} \cos\theta_1 + \gamma_{\beta/M} \cos\theta_2 = \gamma_{\alpha/\beta}$$

$$\gamma_{\alpha/M} \sin\theta_1 = \gamma_{\beta/M} \sin\theta_2$$

$$\sum V = \frac{4\pi}{3} R_0^3$$

where $V_{cap}(r,\phi) = \frac{2\pi}{3} r^3 (1-\cos\phi) - \frac{\pi}{3} r^3 \cos\phi \sin^2\phi$, ϕ: polar angle characterizing the volume fraction of the cap.

The total interface energy of the bi-lobe structure can then be computed as the following:

$$E_{bi-lobe} = \sum_i A_i(r_i, \phi_i)\gamma_i$$

For convenience, all energies are scaled by $4\pi R_o^2 \gamma_{\alpha/\beta}$ to be converted to dimensionless interfacial free energies, and two dimensionless parameters $\gamma_1 = \gamma_{\alpha/M} / \gamma_{\alpha/\beta}$, $\gamma_2 = \gamma_{\beta/M} / \gamma_{\alpha/\beta}$ are also newly defined.

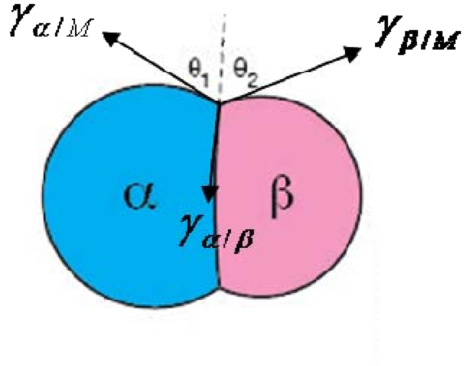

Figure 2.11. Bi-lobe nanocrystals geometry and parameters used to calculate the total interface energy

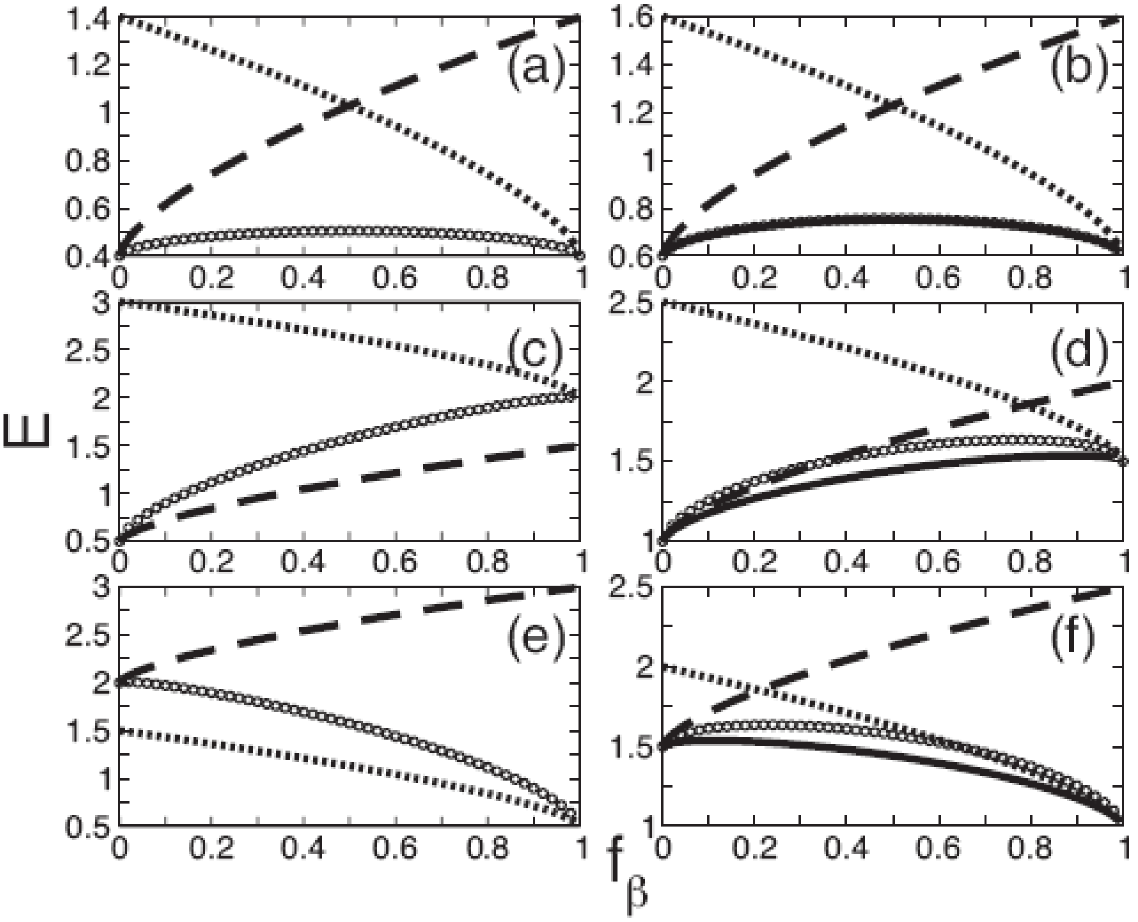

Figure 2.12. Dimensionless interfacial free energy curves as a function of f_β for four types of binary alloy nanocrystals morphologies with $\{\gamma_1,\gamma_2\}$= (a) {0.4, 0.4}, (b) {0.6, 0.6}, (c) {0.5, 2.0}, (d) {1.0, 1.5}, (e) {2.0, 0.5}, and (f) {1.5, 1.0}. Dotted curve: α-core-β-shell, broken line: β-core-α-shell, open circle: two separate nanocrystals, solid line: bi-lobe structure.[56]

Fig 2.12. shows dimensionless interfacial free energy curves of the four possible structures as a function of f_β, the volume fraction of the β phase. Within our model, it is generally true that whenever a stable triple point can be defined, where the interface energies relationships among phases are set by Young's equation, the bi-lobe structure minimizes the interfacial free energy, irrespective of the value f_β. Similarly, when a stable triple point cannot be defined, a unique structure minimizes the free energy for all f_β. The fact that the stable morphology is independent of f_β enables one to develop a structure map that holds for embedded nanocrystals as Fig 2.13.

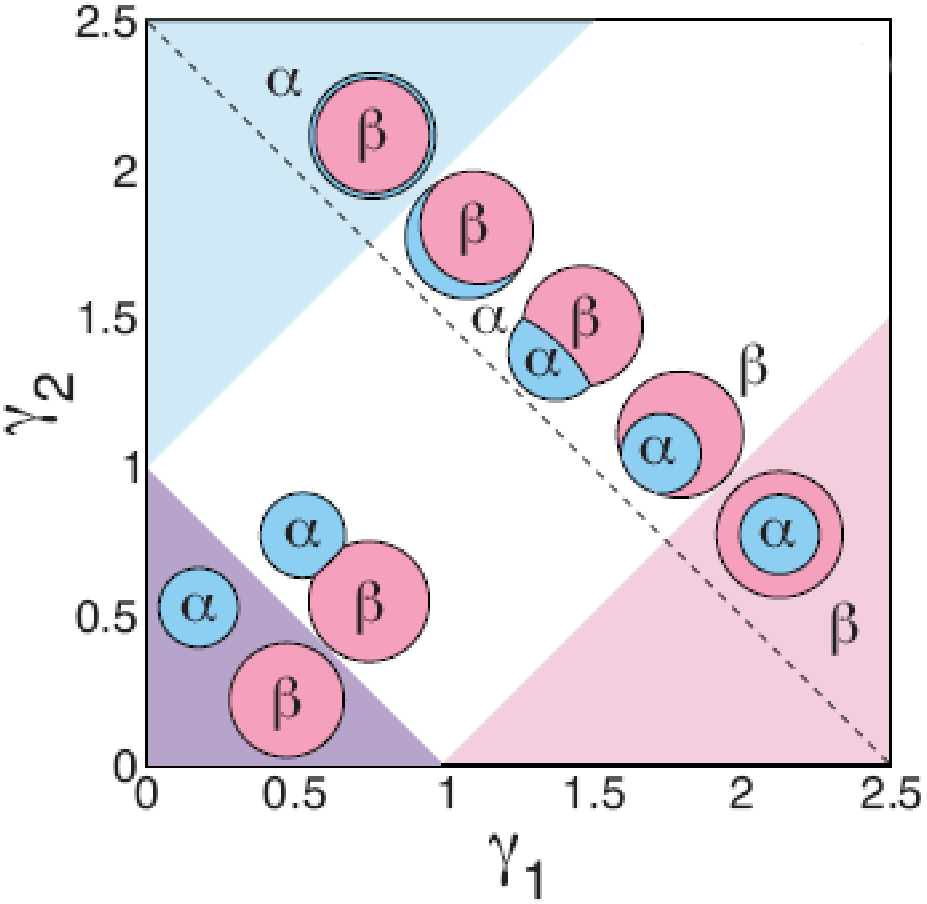

Figure 2.13. Structure map of binary alloy nanocrystals with f_β=0.75. The structures are located at the respective (γ_1, γ_2) coordinates.[56]

2.4.3. Simulation Results

The arguments used to develop an equilibrium structure map of binary nanocrystals in the previous section can be applied to GeSn nanocrystals to estimate the interface energies between two phases, $\gamma_{A/B}$. Given the small volume of an individual nanocrystal and relatively slow speed of the quenching process (a few seconds), we assume the as-formed bi-lobe nanocrystals have reached the equilibrium structure during the synthesis process. The defect-free, crystalline nature of the bi-lobe nanocrystal, as shown in the HRTEM images (Fig 2.8.), also provides evidence of local internal equilibrium.

The structure map predicts that in order to form a bi-lobe type nanocrystal, the sum of any two interface energy values of γ_{Ge/SiO_2}, γ_{Sn/SiO_2}, and $\gamma_{Ge/Sn}$ has to be greater than the other one, satisfying Young's equation at the triple point. The white colored area in Fig 2.13. represents parameter space that satisfies such condition, where $\gamma_1 = \gamma_{Sn/SiO_2}\gamma_{Ge/Sn}$ and $\gamma_2 = \gamma_{Ge/SiO_2}\gamma_{Ge/Sn}$. Moreover, depending on the magnitudes of the interface energies, the morphology of the bi-lobe nanocrystal can vary from dumbell shape to nearly spherical shape as shown in Fig. 2.14.(a)-(c).

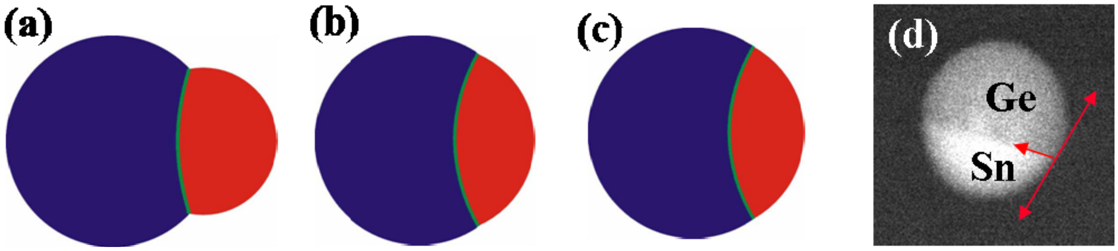

Figure 2.14. Calculated equilibrium geometry of a GeSn nanocrystal with Ge:Sn=4:1 volume ratio. Interface energies $\gamma_1 = \gamma_{Sn/SiO_2}\gamma_{Ge/Sn}$ and $\gamma_2 = \gamma_{Ge/SiO_2}\gamma_{Ge/Sn}$ are set as (a) $\gamma_1 = \gamma_2 = 1$, (b) $\gamma_1 = \gamma_2 = 3$, (c) $\gamma_1 = \gamma_2 = 10$. (d) HAADF-STEM image of a bi-lobe GeSn nanocrystal. (Ge:Sn=4:1) Interfaces are marked with arrows

Careful measurements of the contact angles or the circularity of a single bi-lobe nanocrystal are convenient ways to roughly determine the unknown interface energy, $\gamma_{A/B}$. Nearly perfect spherical shape of the bi-lobe nanocrystals with ~90° contact angles at $\gamma_{Ge/Sn}/\gamma_{Ge/SiO_2}$ and $\gamma_{Ge/Sn}/\gamma_{Sn/SiO_2}$ are observable as shown in Fig 2.10.(a) and Fig 2.14. (d), which indicate γ_{Ge/SiO_2} and γ_{Sn/SiO_2} are much larger than $\gamma_{Ge/Sn}$, and close in their values within the magnitude of $\gamma_{Ge/Sn}$, still satisfying Young's equation. Since γ_{Ge/SiO_2} has been experimentally determined to be 0.91 J/m^2,[63] γ_{Sn/SiO_2} is similar to this value, while $\gamma_{Ge/Sn}$ can be estimated to be ~ 0.1 J/m^2. Additional studies may be required to improve the accuracy of the measurements to accommodate, for example, stress relaxation at the interface.[64] But it is worth noting that interface energies play important roles in nanoscale phenomena, and this method provides a convenient way to estimate the interface energies among materials, especially because of the small dimension comparable to the element diffusion length in the matrix, isotropic nature of the amorphous matrix, and facile replacement of the source material.

Chapter 3

Phase and Shape Evolutions of GeSn Alloy Nanocrystals

3.1. Introduction

In the previous chapter, it was shown that ion beam synthesized $Ge_{1-x}Sn_x$ nanocrystals in a SiO_2 matrix have binary phase bi-lobe morphology as the equilibrium structure. Equilibrium phase and structure at a given temperature are uniquely determined by thermodynamics, and they can be predicted if all the necessary parameters are known. (see chapter 2.4.2.)

However, several factors slow the materials approach to equilibrium. For nanocrystals, for example, strain energy from underlying substrates,[58-61] an energy barrier at the kinetic pathway[63] can prevent the nanocrystals from reaching the equilibrium structure at the given temperature. In addition, kinetics itself can play a major role by controlling cooling or heating rate to keep the material in a metastable state at a certain temperature. From a more practical application point of view, metastable-stable phase transformations principles have been the most extensively used to apply to devices with phase change materials (PCM) such as $Ge_2Sb_2Te_5$ (GST). These compound materials can exist at room temperature in either a stable crystalline state or a metastable amorphous state, and either an optical (e.g. reflectance) or electrical (e.g. resistance) property is markedly different between the two states.[65, 66] For all cases, the elements that consist of the compound materials are miscible, form a single phase, and the way a specific material responds to the heat source, typically tailored current pulse or laser pulse, are fixed.

For a segregating alloy system with eutectic behavior, such as Ge-Sn, this metastable-stable type phase transformation has not been investigated. It is well known that in bulk eutectic alloys the melting point of the alloy can be substantially lower than that of elemental phases of either component. Also, when they are mixed together at high temperature and quenched to room temperature to stay as a metastable state they can form a mixture of any composition by tuning the initial composition of the equilibrium structure. Further, metals are known to influence the recrystallization temperature of amorphous thin films.[67, 68] The implication is that alloying may offer the opportunity to further tune phase equilibria and transition kinetics at the nanoscale, and thereby enable the development of a new type of phase-change material.

Fig. 3.1 illustrates conceptually the envisioned behavior. Heating an embedded binary eutectic-alloy nanostructure (BEAN) to above its melting point yields a liquid droplet with a homogeneous composition. Upon cooling, two types of paths are accessible: (1) For slow cooling, the BEAN can crystallize at temperature T_m, leading to the equilibrium bi-lobe structure. (2) For rapid cooling, the liquid can supercool, then freeze at temperature T_g into an amorphous structure with homogeneous composition as in the liquid state. Upon reheating, the amorphous structure can recrystallize at temperature T_{crys}. Each of the relevant temperatures can be tuned by altering the composition, the cooling rate, or both.

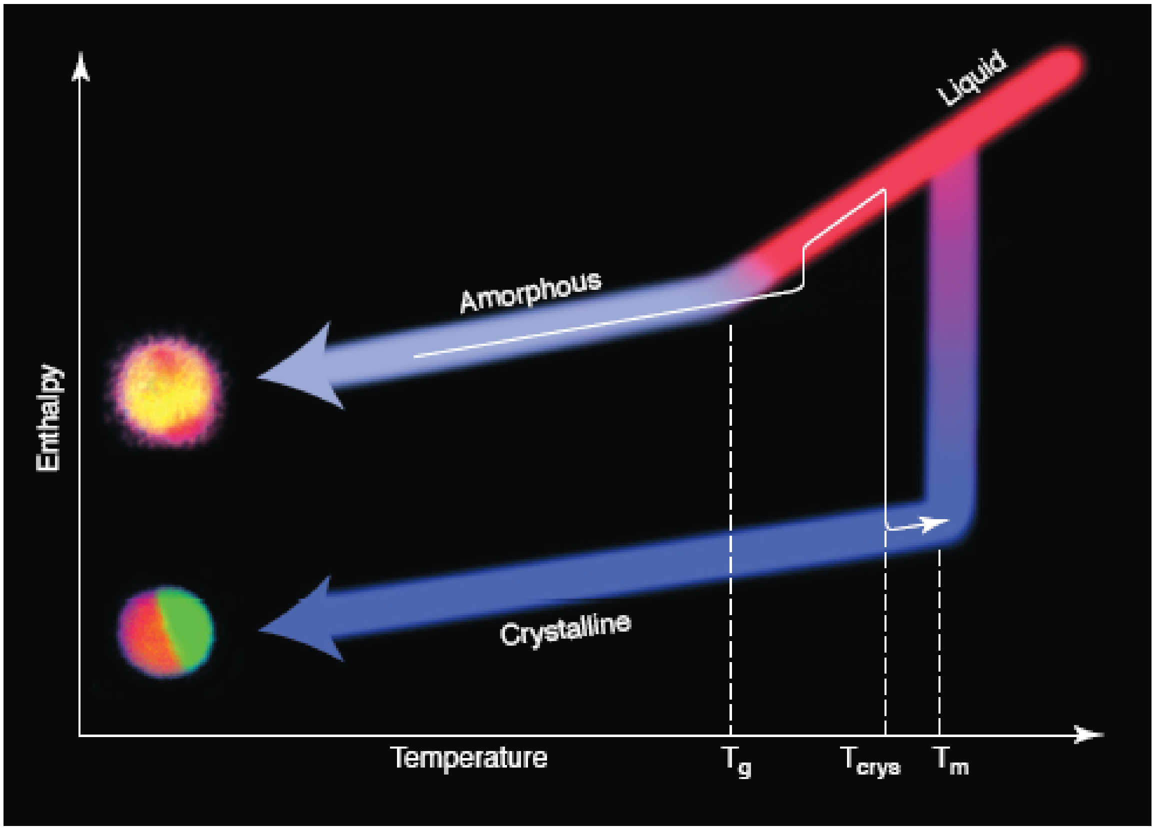

Figure 3.1. A schematic of the operating principle of the phase change nanostructures. Enthalpy curves are sketched for the liquid, crystalline and amorphous phases.

3.2. Pulsed Laser Melting

To form a metastable state of $Ge_{1-x}Sn_x$ nanocrystals, a single pulse from a KrF excimer laser was used to melt the alloy nanocrystals, a process known as pulsed laser melting (PLM). The laser wavelength was 248 nm, and the duration was 30 ns with FWHM of 18 ns. The energy fluence was empirically selected to be 0.3 J/cm^2, and at the laser wavelength and pulse energy used, the particles absorb the laser energy and melt while the silica matrix is relatively unaffected.

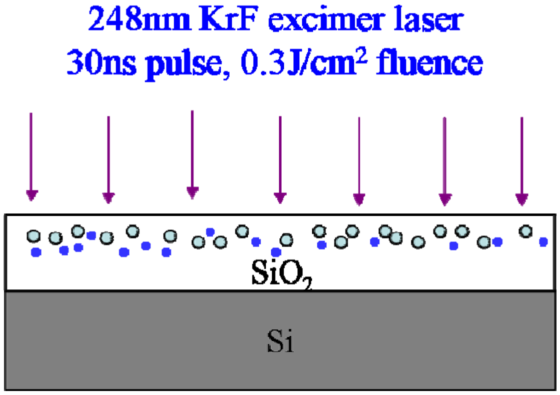

Figure 3.2. A schematic diagram of the PLM process. Laser pulse and the geometry of the embedded nanocrystals are illustrated.

In order to roughly estimate the temperature the nanocrystals reach upon heating by the laser pulse, the heat transfer from laser pulse to the nanocrystals was calculated by solving a simple heat equation: 1 dimensional, non-linear 2nd order partial differential equation.

$$\rho C_p \partial_t T(z,t) = -Q_{in}(z) + \partial_z (K \partial_z T(z,t))$$

Where, ρ : density [g/cm^3], C_p : specific heat [J/g·K], z : depth from the surface [cm]

$K(T)$: thermal conductivity [W/cm·K]

$Q_{in}(z) = -I_o(1-R)\alpha \exp(-\alpha z)$ [W/cm^3]: heat absorbed at depth z

Several simplified assumptions have been made for the calculation: i) Major reflections occur at the Si/SiO_2 interface. ii) Multiple reflection effects are ignored. iii) The heat is absorbed by a 9 nm thick film which is equivalent in volume to nanocrystals formed from Ge implantation at a 4×10^{16} cm^{-2} dose. Physical parameters and boundary conditions (b.c.) used are as follows:

ρ (Ge): 5.32 [g/cm^3], C_p (Ge): 0.32 [J/g·K]

$K_{Ge}(T) = 214T^{-1.03}$: fitted to raw data of ref [36]

$I_o = \dfrac{fluence}{t_{pulse}} = 1.0\times10^7$ [W/cm^2]

n_{Ge} : 1.394,[36] k_{Ge} : 3.197,[36] n_{Si} : 1.570,[36] k_{Si} : 3.565[36]

$$\alpha_{Ge} = \frac{4\pi k}{\lambda} = 1.62\times10^{6}\ [\mathrm{cm}^{-1}],\ R_{Ge} = \frac{(n-1)^2+k^2}{(n+1)^2+k^2} = 0.65,\ R_{Si} = 0.675$$

$$\text{b.c.: } T(z,0) = 300\ \text{K},\ T(10^{-3},t) = 300\ \text{K},\ \partial_z T(0,t) = 0$$

The original Mathematica script and temperature profile results are displayed in Fig 3.3.

```
 d=5.32;
 cp=0.32;
 K_var[Temp]:=214*Temp^-1.03;
 K_room:=0.599;
 K_melt:=0.174
 n=1.394;
 k=3.197;
 R=((n-1)^2+k^2)/((n+1)^2+k^2);
 R
 0.650452
 λ=248*10^-7;
 α=(4 π k)/λ;
 α
 1.61995 10^6


 fluence=0.3;
 tpulse=30*10^-9;
 I_0:=fluence/tpulse
 I_0
 1. 10^7
 I_inc[z_]:=I_0*(1-R)*Exp[-α*z];
 I_inc[0]
 3.49548 10^6
 I_inc[9*10^-7]
 813440.
 R_si=0.675;
I_1=I_inc[0]*R_si
 2.35945 10^6
 Qin[z_]:=-I_0*(1-R)*α*Exp[-α*z]-I_1*(1-R)*α*Exp[-α*z];
 Qin[0]
 -6.99852 10^12
 Qin[9*10^-7]
 -1.62864 10^12
 NDSolve[{d*cp*∂t Temp[z, t] == -
Qin[z]+∂z (214 * Temp[z, t]^-1.03 * ∂z Temp[z, t]) ,Temp[z,0]==300,Temp[1*10^-
3,t]==300,Derivative[1,0][Temp][0,t]==0},Temp,{z,0,1*10^-
3},{t,0,30*10^-9},MaxStepSize → 5*10^-8]
Plot3D[Evaluate[Temp[z,t]/.First[%]],{z,0,10*10^-6},{t,0,30*10^-9},
PlotPoints→30 ,AxesLabel→{"z(cm)","t(sec)","T(K)"},
PlotRange→All]
```

The calculation shows that the maximum temperature reaches ~2000 K, and the temperature drop across 9 nm (0.9×10^{-6} cm) thickness is minimal. It is significantly higher than the melting point of Ge nanocrystals embedded in SiO_2 (1409 K)[63] as well as that of bulk Ge (1210 K), and we can conclude the laser pulse with current parameters provides enough heat to melt the nanocrystals.

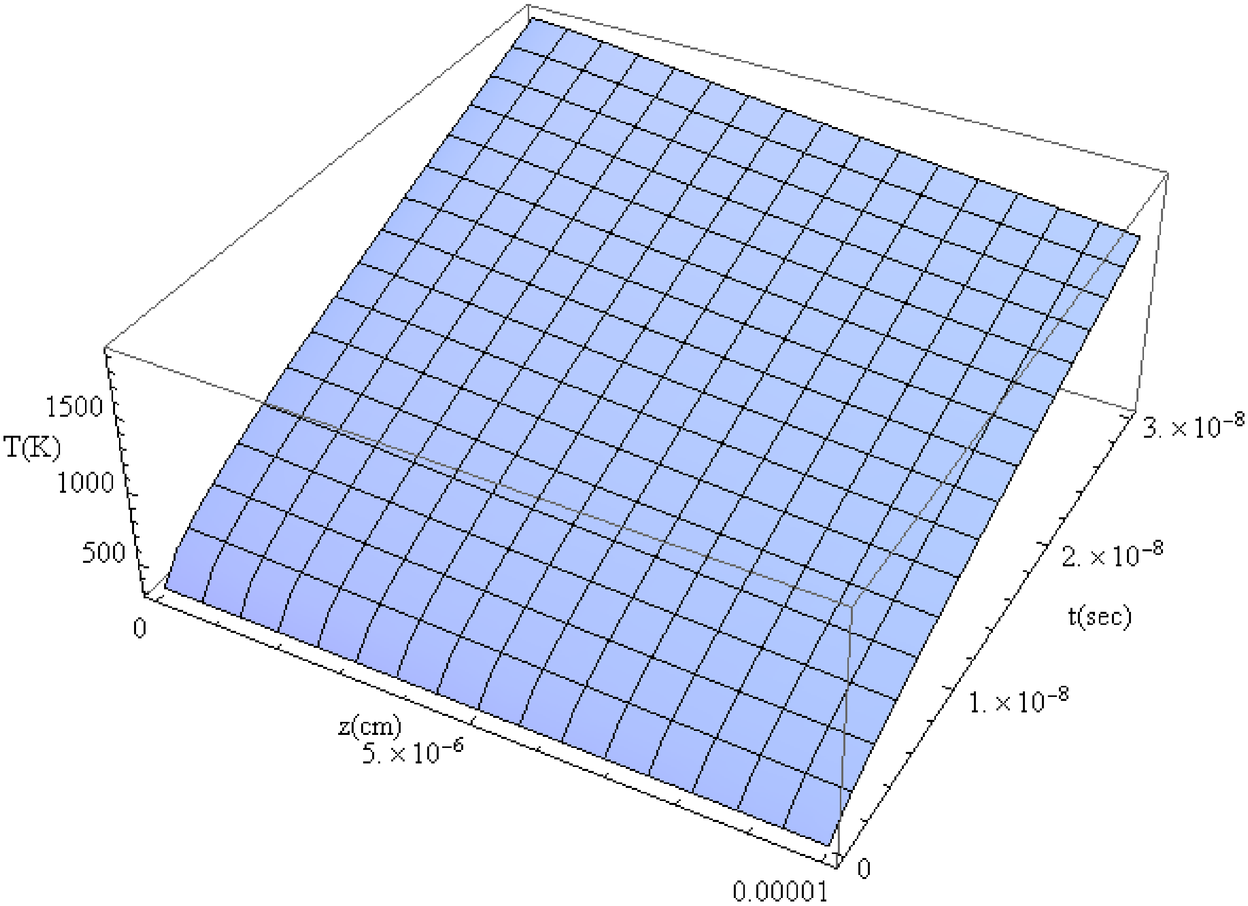

Figure 3.3. The calculation result of the temperature profile (T) of SiO_2 embedded Ge nanocrystals as a function of thickness (z) and time (t), [T(z,t)], upon KrF laser pulse irradiation. The pulse duration is 30 ns, and the energy fluence is 0.3 J/cm^2.

3.3. Structural Characterization

3.3.1. Transmission Electron Microscopy

In order to characterize the PLM processed $Ge_{1-x}Sn_x$ nanocrystals, several characterization methods including advanced TEM were used. As a confirmation step, RBS profiles were obtained before and after PLM. As shown in Fig 3.4., no changes were observed in the profiles after PLM, which means all atoms are retained in the matrix without out-diffusion or ablation, and most probably within the original as-formed nanocrystals. More details about the local structures and atoms in the matrix will be discussed later.

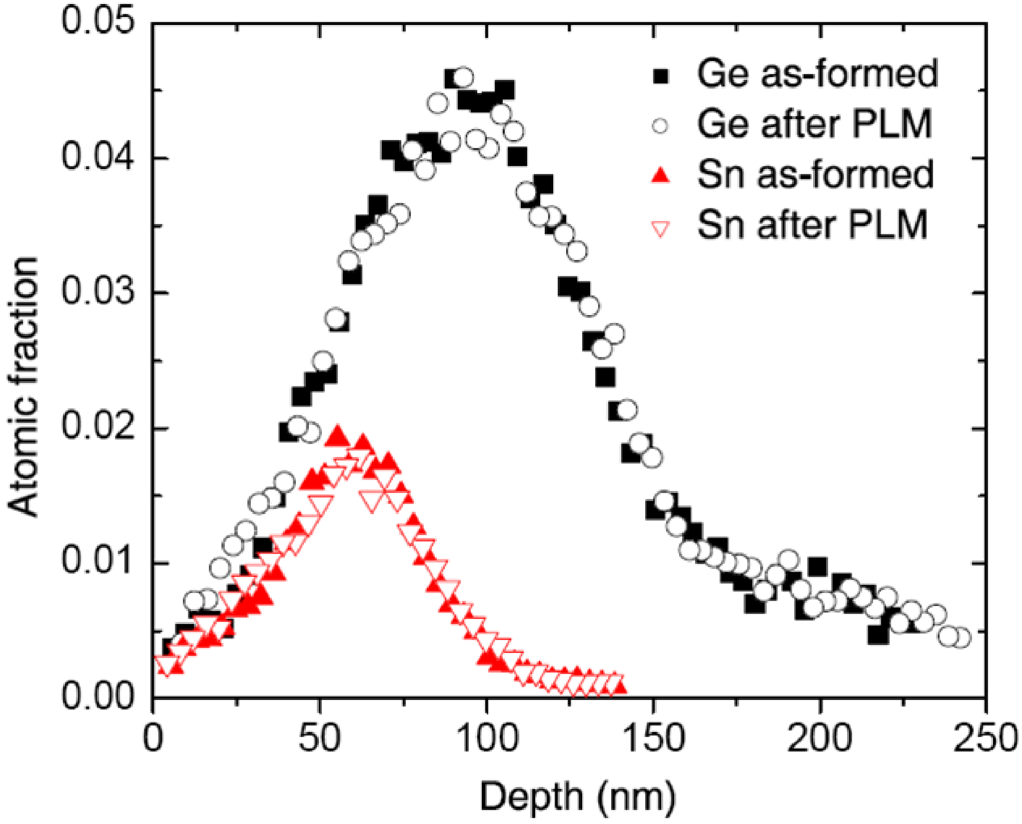

Figure 3.4. RBS profiles of $Ge_{0.8}Sn_{0.2}$ nanocrystals. As-formed nanocrystals were formed by annealing of as-implanted samples at 900 °C for 1hr as described in Chapter 2.4. PLM was performed at 0.3 J/cm^2 energy fluence.

A HAADF-STEM image and an XEDS line scan profile of $Ge_{0.8}Sn_{0.2}$ nanocrystals after PLM process are shown in Fig. 3.5. As Fig. 3.5.(b) indicates, both Ge and Sn atoms are retained in individual nanocrystal. However, the clear Z-contrast that was present within individual bi-lobe nanocrystal as in Fig.2.10. has disappeared, indicating homogeneously mixed alloy nanocrystals have been formed. Given the fact that Ge and Sn are hardly miscible through the entire composition range, and the slow cooling rate of the furnace annealing process (~100°C/sec) compared to the typical liquid to solid phase transformation rate, it can be concluded that $Ge_{1-x}Sn_x$ nanocrystals embedded in the SiO_2 matrix have bi-lobe shape as the equilibrium configuration, and the homogeneously mixed nanocrystals are in a metastable state, kinetically limited by the fast cooling rate of the PLM process.

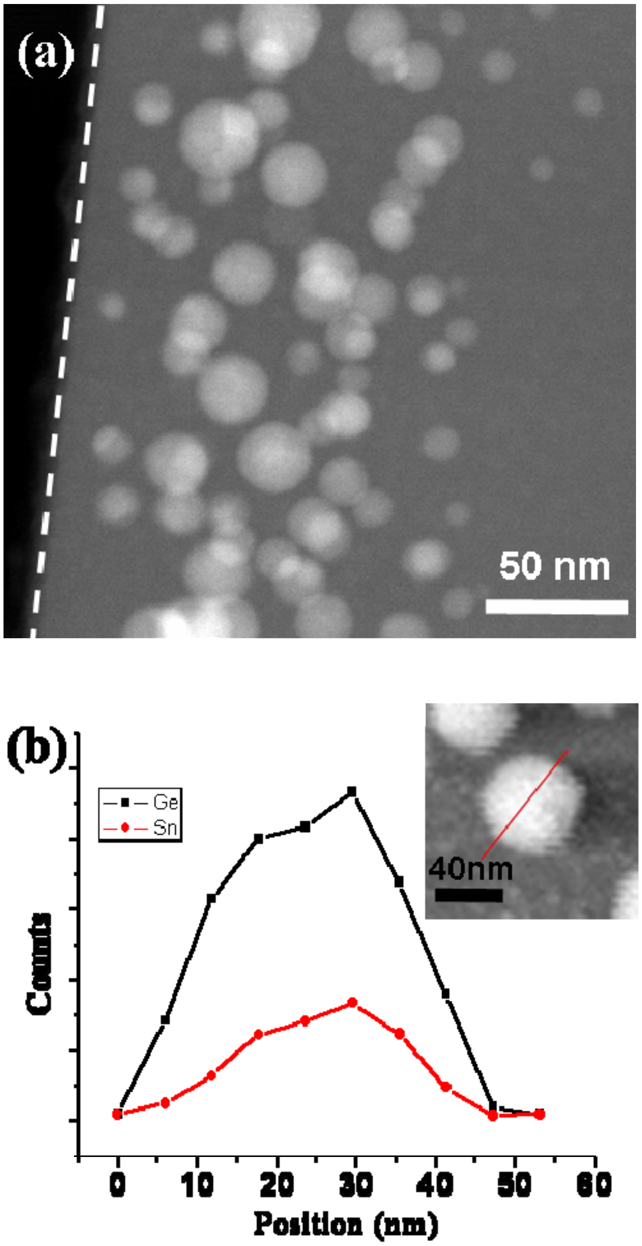

Figure 3.5. (a) Cross-sectional HAADF-STEM image of the $Ge_{0.8}Sn_{0.2}$ nanocrystals after PLM process following thermal annealing at 900°C for 1hr. The dotted line indicates the sample surface. (b) XEDS line scan across a single homogeneously mixed nanocrystal.

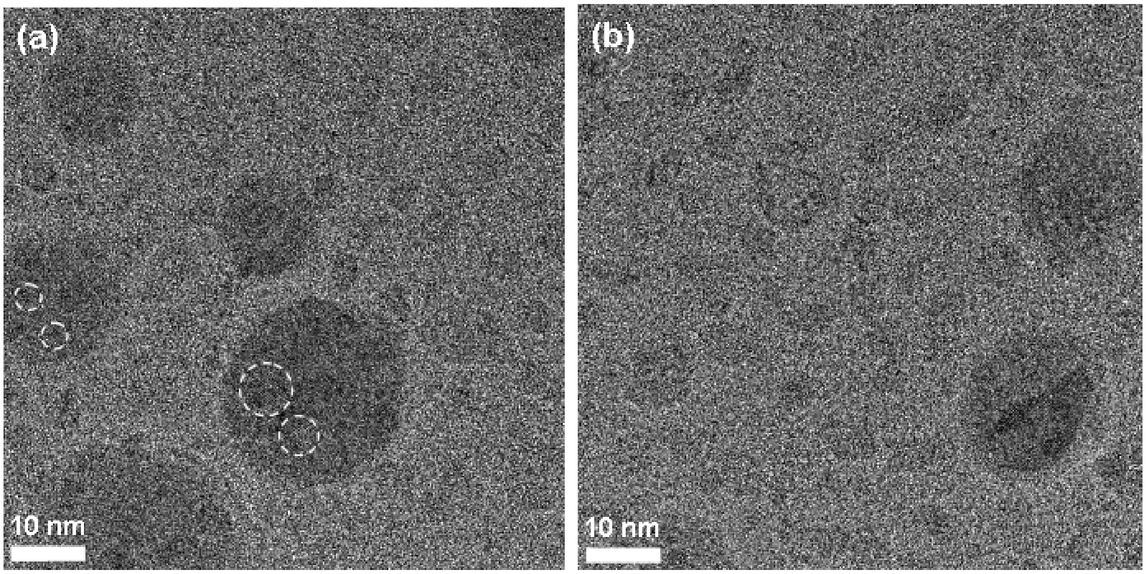

Figure 3.6. HRTEM images of $Ge_{0.8}Sn_{0.2}$ nanocrystals after PLM process. Dotted circles in (a) indicate regions showing lattice fringes.

To investigate crystallinity and microstructure in more detail, HRTEM images were obtained as shown in Fig. 3.6. Lattice fringes or phase segregations were hardly observed except for occasional small regions within some nanocrystals. Together with HAADF-STEM and XEDS results, it indicates that the mixed nanocrystals have an amorphous structure, and lack a long-range order. The small regions that show fringes might be due to local non-perfect mixing or crystallization during the fast cooling process, or some electron beam irradiation effect during the TEM investigation.

3.3.2. Extended X-ray Absorption Fine Structure Analysis

Extended X-ray Absorption Fine Structure (EXAFS) measurements were performed on the bi-lobe and homogeneously mixed $Ge_{0.8}Sn_{0.2}$ nanocrystals as well as on Ge nanocrystals before and after the PLM process to confirm and complement the previous results. TEM in general is a very powerful and accurate technique to determine the local structure of the sample; however, it can probe a very limited area at a time, and often causes electron beam irradiation damage. EXAFS, on the other hand, can still probe local structure at the atomic level, while also provide macroscopic structural information over the entire sample in a non-destructive way. Also, it does not require crystalline materials or specific crystal symmetry for in-depth investigations as TEM or Raman spectroscopy, therefore it is a very attractive technique to investigate amorphous materials.

The measurements were performed at 10 K using a continuous-flow liquid-helium cryostat in fluorescence mode at beamline 7.3 of the Stanford Synchrotron Radiation Laboratory (SSRL). A double-crystal Si (220) monochromator was used and the fluorescence spectra at the Ge K-edge were collected using a 30-element Ge detector. Energy calibration was performed using the absorption edge of a reference Ge foil placed between two ionization chambers located after the sample. The pre-edge, edge, and EXAFS regions were measured at constant energy steps of 10 eV, 0.35 eV and 0.05 eV, respectively. EXAFS data analysis was performed using both SixPACK and ATHENA/ARTEMIS.[69] The theoretical phases and amplitudes were calculated *ab initio* using FEFF 8[70] in a photoelectron momentum (*k*) range of 3-13.5 $Å^{-1}$.

Fig. 3.7. shows the magnitudes of the Fourier transformed EXAFS spectra as a function of the non-phase-corrected radial distance. Four peaks can be observed. The first peak, located at about 1.2 Å, is due to Ge-O bonding and is absent in the reference sample as expected. This Ge-O peak originates from the Ge atoms located at the SiO_2/Ge interface. The remaining three peaks at around 2.1 Å, 3.8 Å, and 4.3 Å correspond to the first, second, and third Ge-Ge nearest neighbor locations, respectively. The second nearest neighbor is only observed in the Ge reference, Ge and $Ge_{0.8}Sn_{0.2}$ nanocrystals. However, after PLM is performed, this peak is no longer observed on the Ge and $Ge_{0.8}Sn_{0.2}$ nanocrystal samples. This indicates the lack of long range order of the Ge atoms after PLM, which is consistent with the Raman spectra showing amorphous Ge peaks.

Table 3.1. shows the refined fitting parameters from EXAFS analysis. The change in coordination number (N) clearly reflects the change of the local environment of the Ge atoms. It is observed that the coordination number (N) for the first nearest Ge-Ge neighbor is lower for the samples containing nanocrystals compared to the bulk Ge reference. This is because atoms at the surface are only partially coordinated.[54] There is a slight decrease of N after PLM, but for $Ge_{0.8}Sn_{0.2}$ nanocrystals, the Ge-Ge bond configuration of the bi-lobe nanocrystals was found to be similar to that of pure Ge nanocrystals. This was expected since the Ge and Sn phases are separated and only a small fraction of the Ge-SiO_2 interface has been replaced by Ge-Sn interface. On the other hand, $Ge_{0.8}Sn_{0.2}$ nanocrystals after PLM are mixtures of Ge and Sn, therefore the N value is expected to decrease significantly. This was confirmed experimentally; the measured N for the bi-lobe structure was 3.5 while the N of the mixed phase was 2.3.

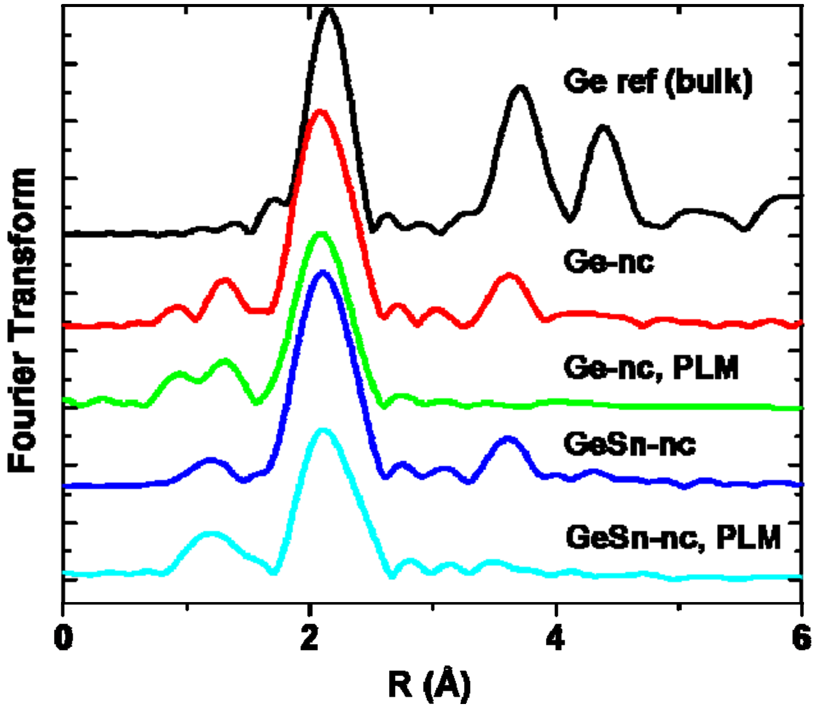

Figure 3.7. Non-phase-corrected Fourier transformed EXAFS spectra of bulk Ge, pure Ge nanocrystals, Ge nanocrystals after PLM, $Ge_{0.8}Sn_{0.2}$-nc, and $Ge_{0.8}Sn_{0.2}$-nc after PLM. The original *k*-space plot was multiplied by k^2 before the Fourier transform.

Sample	Bond type	N	R (Å)	$\Delta\sigma^2(10^{-3}$ Å$^2)$
Ge ref. (bulk)	Ge-Ge	4 (fixed)	2.44 ± 0.01	1.8 ± 0.4
Ge nc	Ge-Ge	3.7 ± 0.2	2.44 ± 0.01	3.3 ± 1.2
Ge nc, PLM	Ge-Ge	3.4 ± 0.2	2.44 ± 0.01	4.9 ± 0.5
GeSn nc	Ge-Ge	3.5 ± 0.3	2.45 ± 0.02	2.7 ± 0.4
GeSn nc, PLM	Ge-Ge	2.3 ± 0.4	2.43 ± 0.01	2.5 ± 0.9

Table 3.1. Refined fitting parameters from EXAFS analysis of the Ge-Ge first coordination shell of the samples in Fig. 3.7. N: coordination number, R: bond length, $\Delta\sigma^2$: variance in the absorber-scatterer distance.

3.4. Recrystallization of GeSn nanocrystals

3.4.1. *Ex-situ* Raman Spectroscopy

To complete a reversible phase transformation cycle, the metastable amorphous phase created by the PLM process must return to the original equilibrium crystalline state. In phase change materials, it is achieved through moderate heating with a tailored current or laser pulse of intermediate intensity. To mimic such processes, rapid thermal annealing (RTA) was carried out for 10 seconds for the PLM-amorphized GeSn nanocrystals, and the RTA temperature dependent crystallization behavior was investigated by *ex-situ* Raman spectroscopy.

Backscattering geometry was used for the Raman measurements where incident and scattered photons are in opposite (180°) directions. It is important to note that in the current sample geometry, Raman scattering from underlying Si substrate as well as that from nanocrystals has to be taken into account. Temple and Hathaway[71] obtained Si Raman spectra in backscattering geometry with several different polarization configurations. They showed that not only one-phonon peak ~520 cm^{-1} but a number of weaker peaks were observed, which were identified with two-phonon Raman scattering. Obviously all those peaks show up in a normal setup without using a polarizer, and the two-phonon Si peak ~300 cm^{-1} overlap with the zone-center optical phonon peak of crystalline Ge. To quench the two-phonon Si peak ~300 cm^{-1}, $x'(y',z')\bar{x}'$ scattering configuration, as defined in Ref.[71] ($x' = (100)$, $y' = (011)$ $z' = (0\bar{1}1)$), was used such that the Raman signal ~300 cm^{-1} could be entirely attributed to Ge component of the randomly oriented GeSn nanocrystals. By convention, the scattering geometry is expressed by four vectors: $k_i(e_i,e_s)k_s$, where k_i, k_s are the directions of the incident and scattered photons, and e_i, e_s are the polarizations of the incident and scattered photons, respectively.

Fig. 3.8. shows the RTA temperature dependent Raman spectra of $Ge_{0.8}Sn_{0.2}$ nanocrystals. As-formed $Ge_{0.8}Sn_{0.2}$ bi-lobe nanocrystals show a strong crystalline Ge peak at ~300 cm^{-1}, and the peak is asymmetrically broadened to the lower energy side due to the phonon confinement effect. After the PLM process, however, the crystalline Ge peak is significantly suppressed, and the spectrum shows a broad peak at ~275 cm^{-1}. This feature has been observed from a sputtered Ge film, free-standing Ge nanocrystals exposed to air[41, 64] and embedded Ge nanocrystals after PLM (Chapter 3.4.3), and it is attributed to disordered Ge-Ge bonds in the amorphous Ge phase.[72] At low RTA temperatures (e.g. the 323 °C), the Raman peak is intermediate in width between the as-formed and amorphous cases and is starting to develop the characteristic asymmetric peak. This indicates the formation of small crystalline Ge clusters. As the RTA temperature increases, the peak narrows and eventually resembles that of the as-formed state, showing that larger Ge clusters have recrystallized.

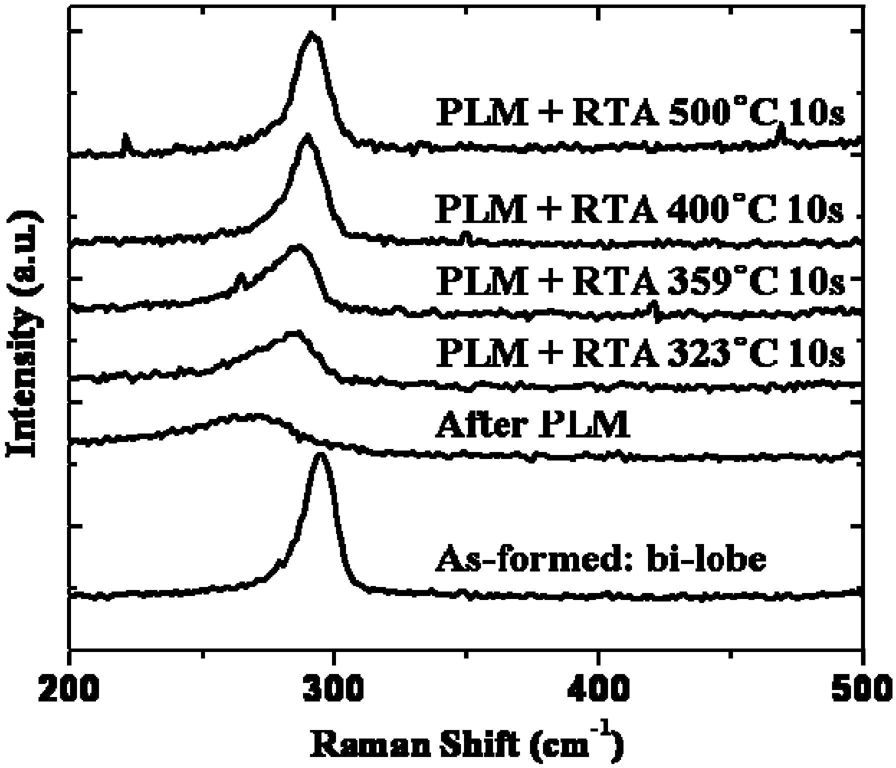

Figure 3.8. RTA temperature dependent Raman spectra of PLM-amorphized $Ge_{0.8}Sn_{0.2}$ nanocrystals. Raman spectrum of as-formed (900 °C, 1hour annealing without PLM) is also shown.

3.4.2. *In-situ* TEM Observations

The recrystallization process of $Ge_{0.8}Sn_{0.2}$ nanocrystals was directly observed in an *in-situ* TEM (JEOL 3010) equipped with a heating stage. Images captured as a function of temperature are shown in Fig. 3.9.

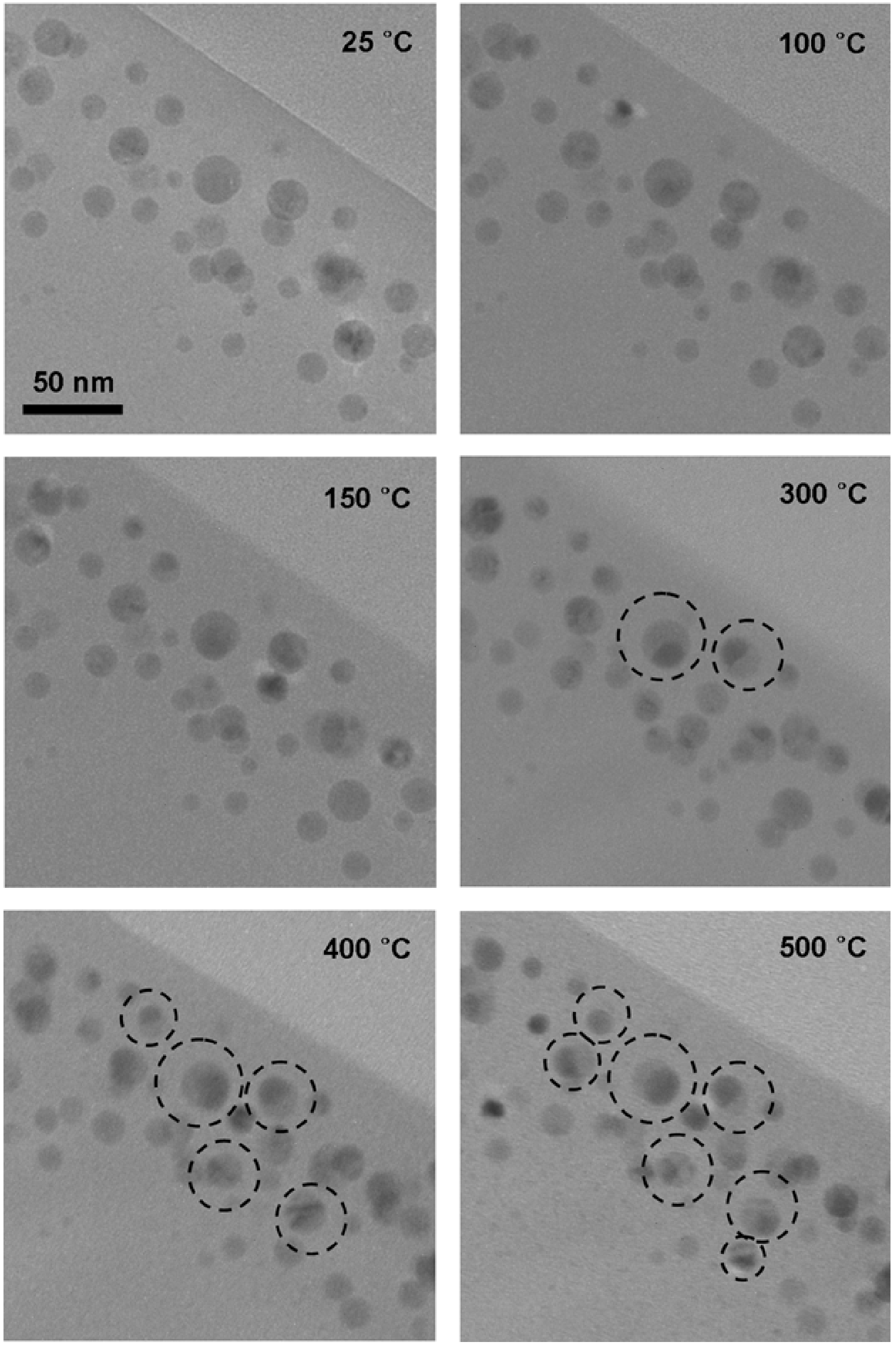

Figure 3.9. *In-situ* TEM micrographs of amorphized $Ge_{0.8}Sn_{0.2}$ nanocrystals at elevated temperature. Nanocrystals with a dashed circle show clear phase separation between Ge and Sn phases.

Since the initial structure is in a homogeneously mixed amorphous state, each nanocrystal is in a single phase as represented by single contrast. Phase separated bi-lobe nanocrystals can be first observed at 300°C, and most of the phase segregation occurs between 300 °C and 400°C. These temperatures are in excellent agreement with the Raman result presented in Fig. 3.8 that indicates a crystallization temperature (T_{crys}) ~320 °C. Nanocrystals with a dashed circles show clear phase separation between Ge and Sn phases. Note that some overlapped, but still single phase nanocrystals can be also observed at low temperatures (<150 °C).

HAADF-STEM images of the $Ge_{0.8}Sn_{0.2}$ nanocrystals after PLM+RTA at 500 °C for 10 seconds are also shown in Fig. 3.10. Z-contrast between Ge and Sn phases can be clearly observed, and the morphologies of the nanocrystals are the same as as-formed bi-lobe nanocrystals. Taken the Raman and the TEM results together, it is confirmed that $Ge_{0.8}Sn_{0.2}$ nanocrystals follow a reversible crystalline – amorphous – crystalline path.

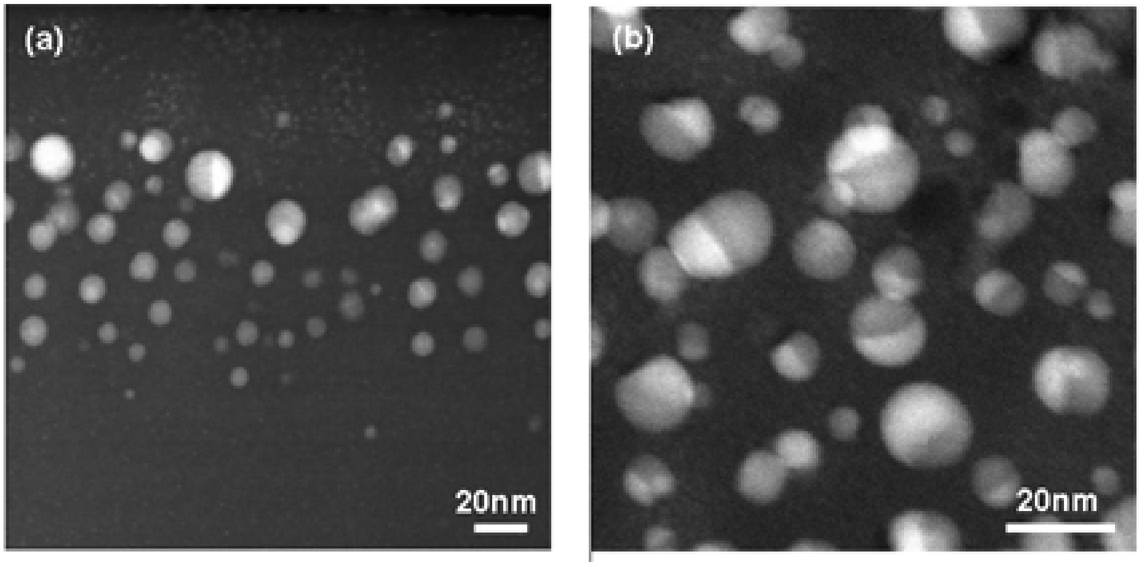

Figure 3.10. HAADF-STEM images of $Ge_{0.8}Sn_{0.2}$ nanocrystals after PLM followed by RTA at 500 °C for 10 seconds. (a) Cross-sectional view and (b) planview TEM sample

3.4.3. Ge:Sn Ratio Dependent Recrystallization

Having established that one can induce a phase change within binary eutectic alloy nanocrystals, we now turn our attention to controlling the transformation. In particular, we will consider how the composition can be used to change the recrystallization kinetics in order to tune the recrystallization temperature.

Starting with PLM-amorphized pure Ge nanocrystals without any Sn content, a 10 second rapid thermal annealing step was performed over a range of temperature and the degree of crystallization was monitored by *ex-situ* Raman spectroscopy, the same way it was carried out for $Ge_{0.8}Sn_{0.2}$ nanocrystals. Fig. 3.10.(a) shows the RTA temperature dependent Raman spectra of pure Ge nanocrystals. The recrystallization begins near 500 °C and reaches completion around 600 °C. Pure Ge nanocrystals are known to be approximately 5 nm in diameter from the earlier study of Sharp et al.,[41] and the current result is in good agreement with the reported recrystallization temperature (T_{crys}) of amorphous Ge/SiO_2 superlattices with 5 nm thickness.[73]

For the Sn composition dependent study, ^{74}Ge was implanted first with fixed energy and dose, 150 keV and 4×10^{16} cm^{-2}. It was followed by ^{120}Sn implantation at 120 keV with 1×10^{16}, 2×10^{16}, and 4×10^{16} cm^{-2} doses for $Ge_{0.8}Sn_{0.2}$, $Ge_{0.67}Sn_{0.33}$, and $Ge_{0.5}Sn_{0.5}$ nanocrystals, respectively. PLM was performed at the same energy fluence, 0.3 J/cm^2. As demonstrated with $Ge_{0.8}Sn_{0.2}$ nanocrystals (Fig. 3.8) and pure Ge nanocrystals (Fig. 3.10.(a)), the width of the Raman peak is very useful to characterize the extent of the observed recrystallization. Fig. 3.10.(b) displays the full width at half maximum (FWHM), scaled by the FWHM at 25 °C for each data set plotted as a function of RTA temperature for nanocrystals of varying compositions. The lines are guides to the eye, constructed by fitting the data to an empirical functional form:

$$\frac{FWHM}{FWHM_{25\,^\circ\mathrm{C}}} = \frac{\left(1 - w_{\mathrm{avg}}\right)}{2}\left[1 - \tanh\left(\frac{T - T_{\mathrm{crys}}}{\Delta T}\right)\right] + w_{\mathrm{avg}}$$

w_{avg} is the average width of the crystalline Raman peaks for all of the samples, $FWHM_{25\,^\circ C}$ is the width of the peak after pulsed laser melting for the specific sample being fitted, ΔT is a parameter that adjusts the temperature range over which the peak width is changing, and T_{crys} is the characteristic recrystallization temperature for the sample. We define the characteristic T_{crys} as the point for which the scaled FWHM is reduced by one-half of its total magnitude of reduction upon complete recrystallization. These temperatures are plotted versus composition in Fig. 3.10.(c). As shown, as the Sn composition, x, is increased, T_{crys} of $Ge_{1-x}Sn_x$ decreases. For example, T_{crys} is lowered to approximately 150 °C in nanocrystals with composition near 50 atomic percent Sn (Ge:Sn=1:1).

The observed dependence of the recrystallization temperature on Sn content merits discussion. It is well known that amorphous semiconductors, such as Si and Ge, crystallize at temperatures well below the normal crystallization temperature when in contact with metals.[67, 68] This phenomenon, known as metal-induced crystallization (MIC), has been observed for both semiconductor-metal bilayer structures,[74-77] and co-deposited composites.[78, 79] Wang et al.[75] observed that MIC of amorphous(*a*)-Ge/ crystalline(*c*)-Al bilayer structure resulted in Ge/Al layer exchange, and ascribed the microscopic steps to Al diffusion into *a*-Ge, *c*-Ge grain formation at the Al grain boundaries, and Ostwald ripening of the *c*-Ge grains mediated by Al atoms. Also, Kono et al.[74] directly observed nucleation of single phase *c*-Si at Al grain

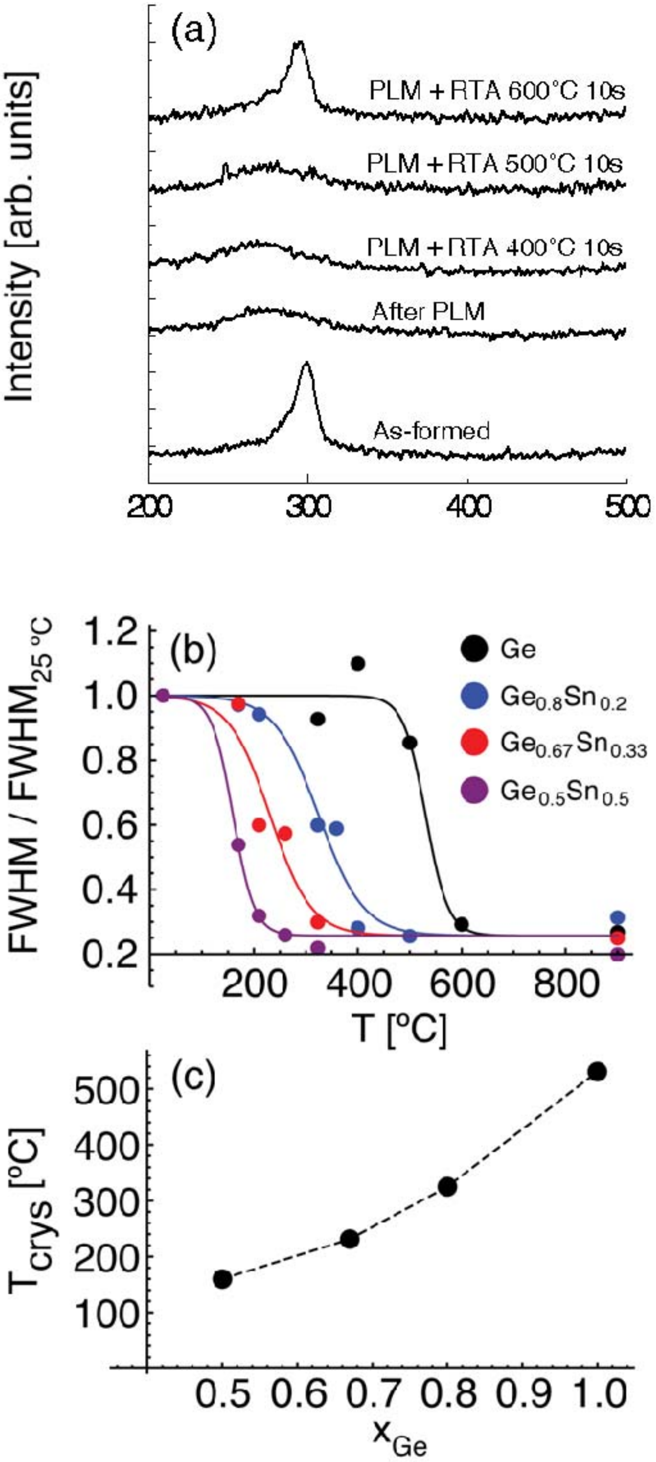

Figure 3.10. Temperature dependent crystallization of amorphized Ge$_{1-x}$Sn$_x$ nanocrystals. (a) RTA temperature dependent *ex-situ* Raman spectra of pure Ge nanocrystals, (b) Plot of the FWHM of the Raman peak vs. RTA temperature for different compositions, (c) T_{crys} versus composition in atomic percent as estimated from (b). The dashed line is a guide for the eye.

boundaries at elevated temperature on *a*-Si/*c*-Al multilayer structure with *in-situ* HRTEM. Tan et al.[78] studied MIC of Ge/Au on codeposited film, and suggested that Au-Ge bonding is critical in the MIC process based on the EXAFS data. In the Si/Au system,[80] segregation of Au at the moving crystal-amorphous interface of Si was also directly observed, supporting the semiconductor-metal bond breaking, metal diffusion, and grain growth by mass transport argument. The decreased coordination number N of Ge-Ge of the amorphized $Ge_{0.8}Sn_{0.2}$ nanocrystals strongly supports the increased number of Ge-Sn bonds, and therefore effective source of Sn induced crystallization of *a*-Ge. Evidently, GeSn nanocrystals embedded in silica display a similar phenomenon. Certainly, the recrystallization is influenced by the number of GeSn bonds in the structure. Although the precise origins of the composition dependence of T_{crys} remain to be understood, it is clear and significant that the observed tuning range extends from near room temperature to over 500 °C.

3.5. Phase Map Construction: EFTEM Spectrum Imaging

One way to quantitatively characterize the distribution of different phases in the TEM specimen is to use the energy filtered transmission electron microscopy (EFTEM) technique. EFTEM utilizes one of the electron energy-loss spectrum features either to enhance the contrast by selecting only zero-loss elastic electrons or to tune the contrast by selecting only low-loss electrons or to create a specific elemental map by selecting only high-loss electrons near the electron shell edge energies. In particular, in the EFTEM spectrum imaging (SI) mode one collects the full spectrum at each individual pixel for the chosen energy-loss range (x, y, ΔE: 3-D collection), therefore it reduces the chance to miss minor peaks and enables post acquisition processing to create a chemical map.

To apply this technique to create a chemical map of the $Ge_{0.67}Sn_{0.33}$ alloy nanocrystals at each phase transformation step (bi-lobe crystalline– mixed amorphous – bi-lobe crystalline), EFTEM SI data collection followed by post acquisition data processing was performed. For the current experiment, slightly different energies were used for ^{74}Ge and ^{120}Sn implantation to improve the overlap between the distribution profiles. ^{120}Sn and ^{74}Ge were sequentially implanted at room temperature into 500 nm thick SiO_2 with energies and doses of 170 keV, 2×10^{16} cm^{-2} for ^{120}Sn, and 120 keV, 4×10^{16} cm^{-2} for ^{74}Ge, respectively. The initial annealing, PLM, and post-PLM RTA conditions were identical to the previous $Ge_{1-x}Sn_x$ nanocrystal experiments. The RBS profiles of Ge and Sn are presented in Fig. 3.11 for the as-implanted and as-formed states, showing an excellent match in their peak positions. (~80 nm below the surface)

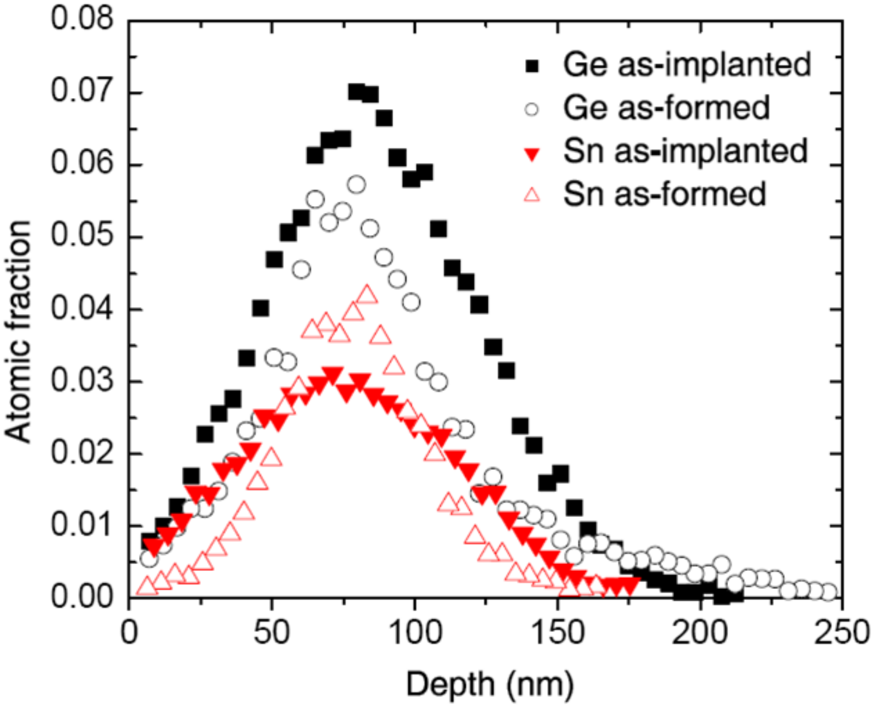

Figure 3.11. RBS spectra of Ge and Sn atoms for as-implanted and as-formed samples. Implantation energies and doses are 170 keV, 1×10^{16} cm^{-2} for ^{120}Sn and 120 keV, 4×10^{16} cm^{-2} for ^{74}Ge (Ge:Sn=2:1).

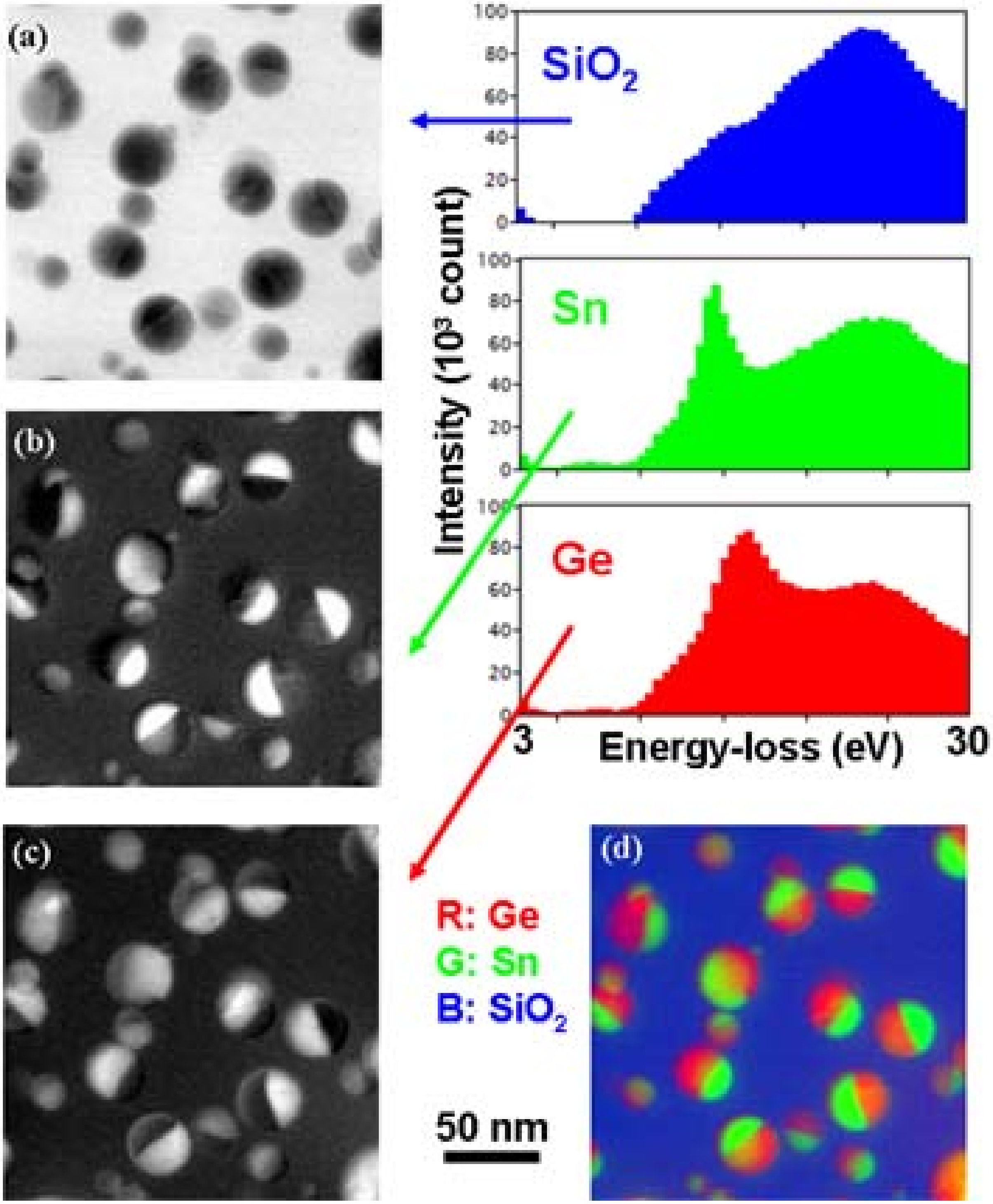

Figure 3.12. Phase maps of the as-formed $Ge_{0.67}Sn_{0.33}$ nanocrystals. (a) SiO_2, (b) Sn, (c) Ge maps are extracted from the EFTEM SI dataset. Three images are combined in (d) where the contribution of each phase is indicated with colors.

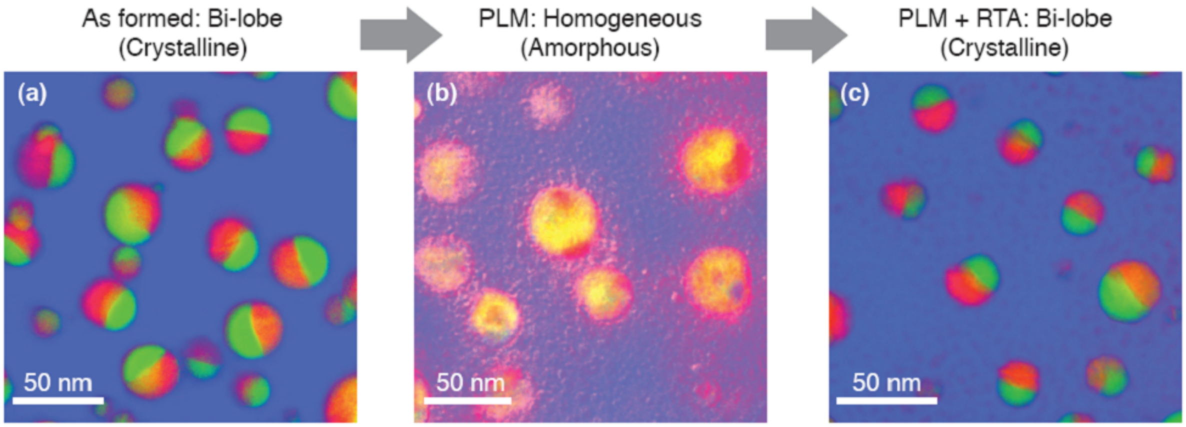

Figure 3.13. Phase maps of phase-changed $Ge_{0.67}Sn_{0.33}$ nanocrystals. Phases of (a) as-formed bi-lobe , (b) PLM processed homogeneously mixed amorphous, and (c) bi-lobe after PLM and RTA (400 °C 10sec) are indicated using colors.

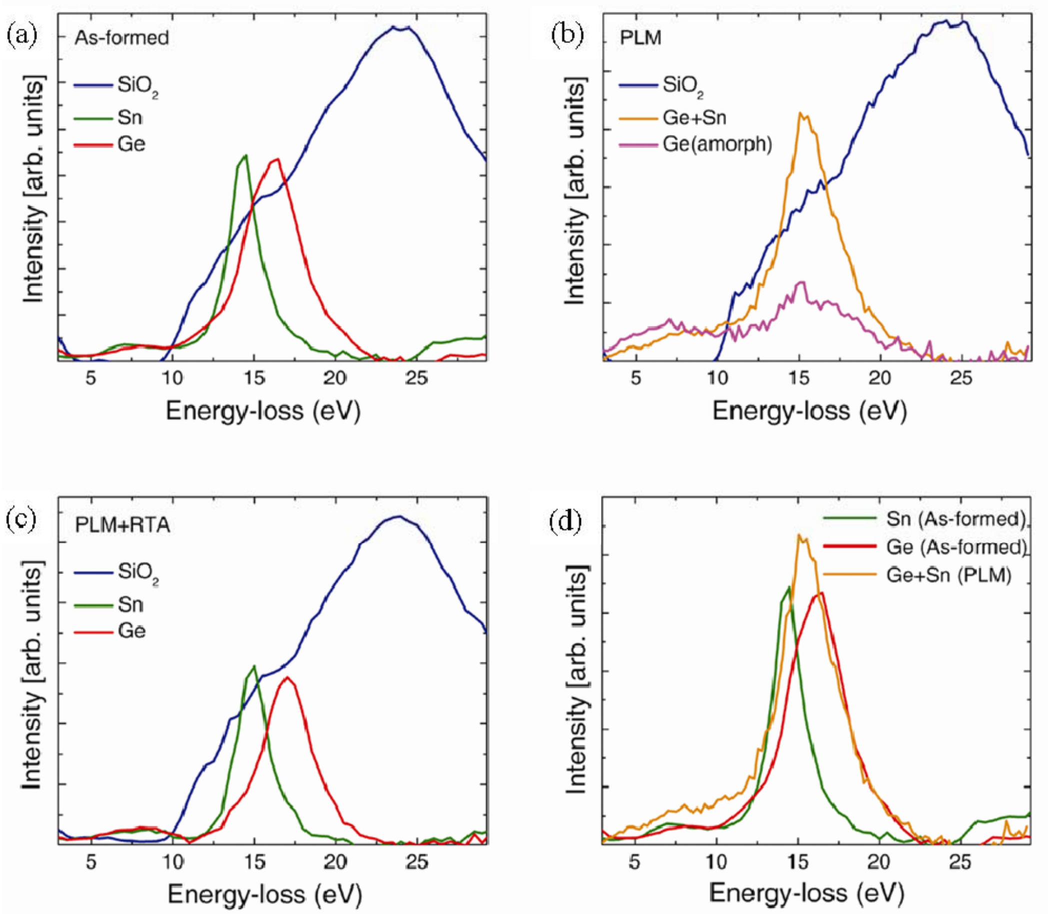

Figure 3.14. (a)-(c) phase-specific EELS spectra of the phases that are present in Fig. 3.13.(a)-(c), respectively. (d) Ge and Sn EELS spectra from (a) and Ge+Sn spectrum from (b) are overlapped to show that the plasmon resonance for the mixed phase lies between those of Ge and Sn.

Individual phase maps of the as-formed $Ge_{0.67}Sn_{0.33}$ nanocrystals are shown in Fig. 3.12 as an example of the extraction process. First, EFTEM SI datasets were obtained in the 3~30 eV electron energy loss range using a 0.5 eV step and a 0.5 eV energy slit width. Then in order to construct the individual phase maps, reference EELS spectra were extracted from the selected areas of the image (e.g. from regions rich in SiO_2, Ge, and Sn, respectively). Finally, multiple linear least squares (MLLSQ) fitting was applied to the image using the reference spectra thereby determining the contribution of each phase to the observed EELS spectrum. In the individual phase map, the contribution is indicated using pixel brightness (Fig. 3.12.(a)-(c)), and in the final combined image contributions of each phase are indicated using colors.(Fig. 3.12.(d))

Phase maps were constructed for the PLM processed and PLM+RTA samples in the same way as for the as-formed bi-lobe sample. The maps and the reference spectra used are presented in Fig. 3.13 and Fig. 3.14, respectively.

Note that in Fig. 3.14, the SiO_2 bulk plasmon peak (blue) was also superimposed on other phases' characteristic EELS spectra that were used for MLLSQ fittings, since nanocrystals are surrounded by SiO_2 matrix materials in thickness (z) direction as well as in the in-plane directions. The EELS spectrum from pure SiO_2 materials (blue) was normalized and subtracted from each spectrum to obtain pure phase specific spectra as shown with different colors. Specifically, Fig. 3.14.(d) shows that the plasmon resonance for the mixed phase (orange) lies between that of nanocrystalline Ge and nanocrystalline Sn. Since this plasmon energy is determined by the valence electron density, it could be concluded that the valence electron density of the PLM structure lies between that of the Ge and Sn structures.

Chapter 4

Nanoscale Phase Segregation of GeAu Nanowires

4.1. Introduction

In Chapter 3, we showed phase transformation behavior of binary eutectic alloy nanocrystals. The key parameter that determined the final phase structure was the cooling rate following heating above the melting point of the mixed alloy. On the other hand, there was no composition dependent morphological change in the structure of each state: phase segregated bi-lobed crystalline nanocrystals for the equilibrium state, and homogeneously mixed amorphous phase for the kinetically limited state. Also, *in-situ* heating TEM investigations shown in Fig. 3.9. displayed only two such types of nanocrystals while heating up to 500 °C; there are no intermediate states. The reason behind this simple behavior is related to the small dimension of the 3 dimensionally confined nanocrystals. Melting/solidification or solid state diffusion that are essential to phase segregation occur at sufficiently large length scales not to be limited by atomic diffusion length within a single nanocrystal to reach the global equilibrium.

When the confinement is relaxed in one direction, as in nanowires (NWs) for example, there could exist multiple composition dependent stable structures, although it may not be in a global equilibrium state, due to the effectively infinite length for atomic diffusion in one direction. Since NWs present an ideal platform for elucidating these kinds of nanoscale phenomena while also having high potential for technological applications, it has attracted many researchers in the past decade.[81-85] In a structural engineering perspective, they have demonstrated the synthesis of NW materials with tailored composition by altering the precursors during the growth process, resulting in superlattice structures with unique electrical and optical properties.[86, 87]

In the current study, we present a different approach, involving the composition dependent post-growth engineering of the NW structure through alloying and phase segregation of binary eutectic compounds induced by thermal annealing. The study was led by Professor Ali Javey in the EECS department, and we participated in the *in-situ* heating experiments and the modeling. As an example, we utilized the Ge-Au system which has a low eutectic temperature (361 °C) with negligible Au solid solubility ($<10^{-3}$ at. %) in Ge at room temperature. In this approach, Ge-Au core-shell NWs with HfO_2 capping layer are first prepared, and then thermally annealed during which a wide range of nanostructures are controllably formed depending on the initial Au content and the annealing conditions. This approach presents a novel route for controlling the NW composition and structure with potential implications for applications in phase change memory, optoelectronic, and electronic devices.

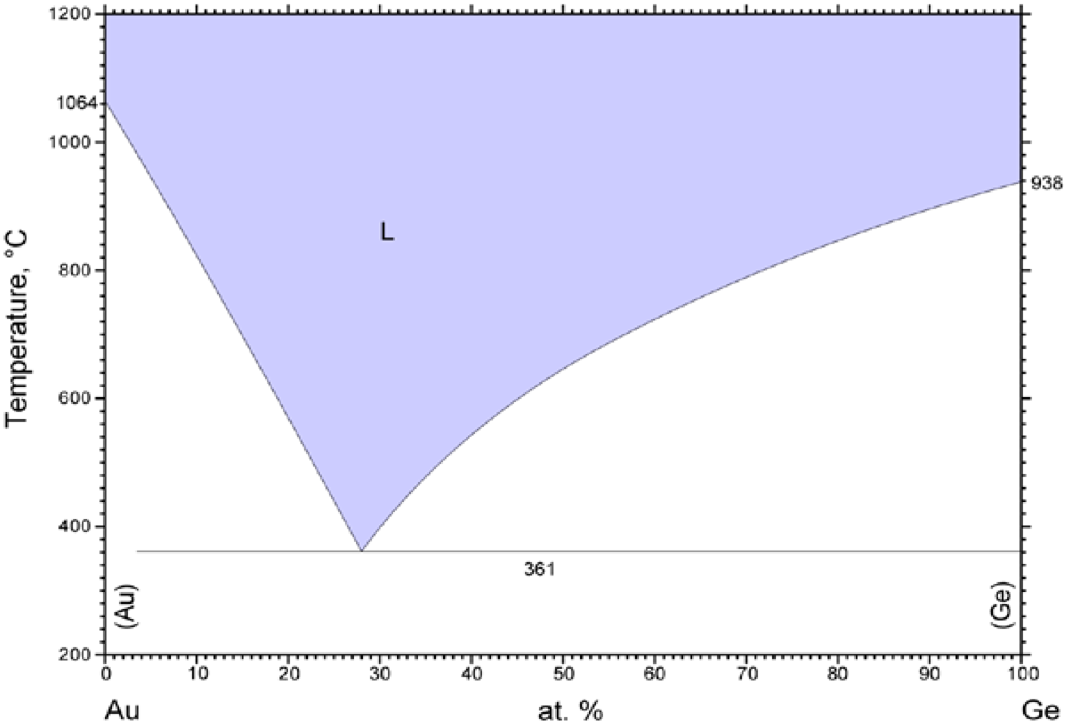

Figure 4.1. Ge-Au binary eutectic phase diagram.[88]

4.2. Composition Dependent Phase Segregation

The NWs with varying compositions were grown in the Microlab at UC Berkeley and the as-grown structures were characterized with HAADF-STEM at the Molecular Foundry, Lawrence Berkeley National Laboratory by our collaborator Dr. Yu-Lun Chueh in Professor Ali Javey's group. The overall concept of this structural engineering process is illustrated in Fig. 4.2. Single crystalline Ge NWs are first synthesized by the vapor-liquid-solid process as previously reported in the literature[89] with diameters d=50~60 nm. (Fig. 4.2.(a)) Then, a Au layer is sputtered on the surface of the Ge NW arrays with a thickness of t_{Au}=2~15 nm. (Fig. 4.2.(b)) The thickness of the sputtered Au layer determines the overall Au:Ge atomic ratio of the NWs by taking into account the calculated volumes from TEM images and known densities of Au and Ge. The NWs are then capped with ~10 nm thick HfO_2 deposited by atomic layer deposition (ALD). (Fig. 4.2.(c)) Finally, thermal annealing at 450 °C for 5 minutes is performed in forming gas (95 % Ar and 5 % H_2) with heating and cooling rates of approximately 7.5 °C/sec and 1.5 °C, respectively. Note that the HfO_2 capping layer is essential for serving as a nanoscale template for the controlled formation of the GeAu nanostructures. Without the HfO_2 template, the overall shape and structure of the NWs are uncontrollably altered during the annealing step due to the partial or full melting of the NWs at elevated temperatures.

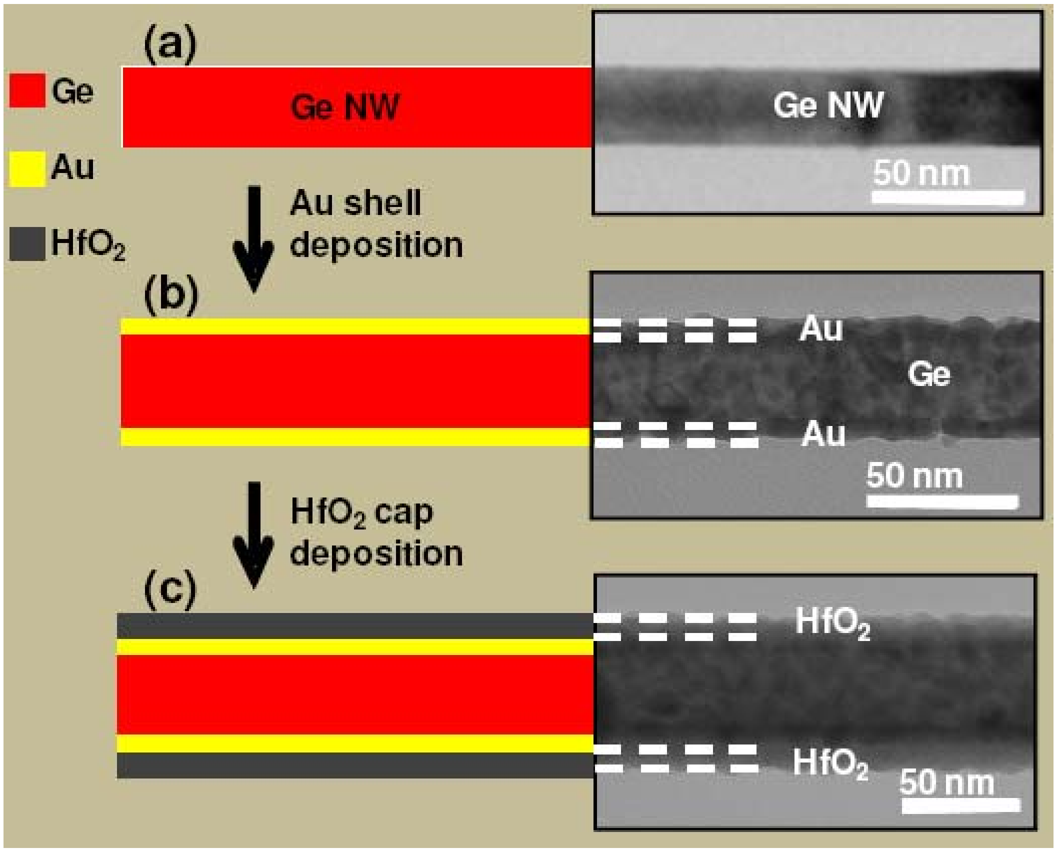

Figure 4.2. Schematic illustration of the fabrication scheme and the corresponding TEM images of the initial GeAu core-shell NWs with a 10 nm HfO_2 capping layer. (Courtesy of Dr. Yu-Lun Chueh)

Fig. 4.3. shows the representative transmission TEM images of a series of GeAu nanostructures formed via the described process for NW samples from low to high overall Au atomic concentration. At low Au concentrations (<25 at. %), pyramid shaped, Au-rich (~97 at. % from an EDX quantitative analysis, Table 4.1) islands are formed on the outer surface of the NWs, beneath the HfO_2 capping layer (Fig. 4.3.(a)). In contrast, near periodic nanodisk patterns are formed as the Au concentration is increased to 29-37 at. % (Fig. 4.3.(b)). These periodic structures are composed of alternating Ge-rich (96 at. %) and Au-rich (99 at. %) regions. As the Au concentration is further increased to 38-50 at. %, most structures exhibit Au-Ge core-shell characteristics (Fig. 4.2(c)). Finally, once the Au content increases to 70-80 at. %, NWs are fully transformed to Au_xGe_{1-x} alloys (Fig. 4.2(d)).

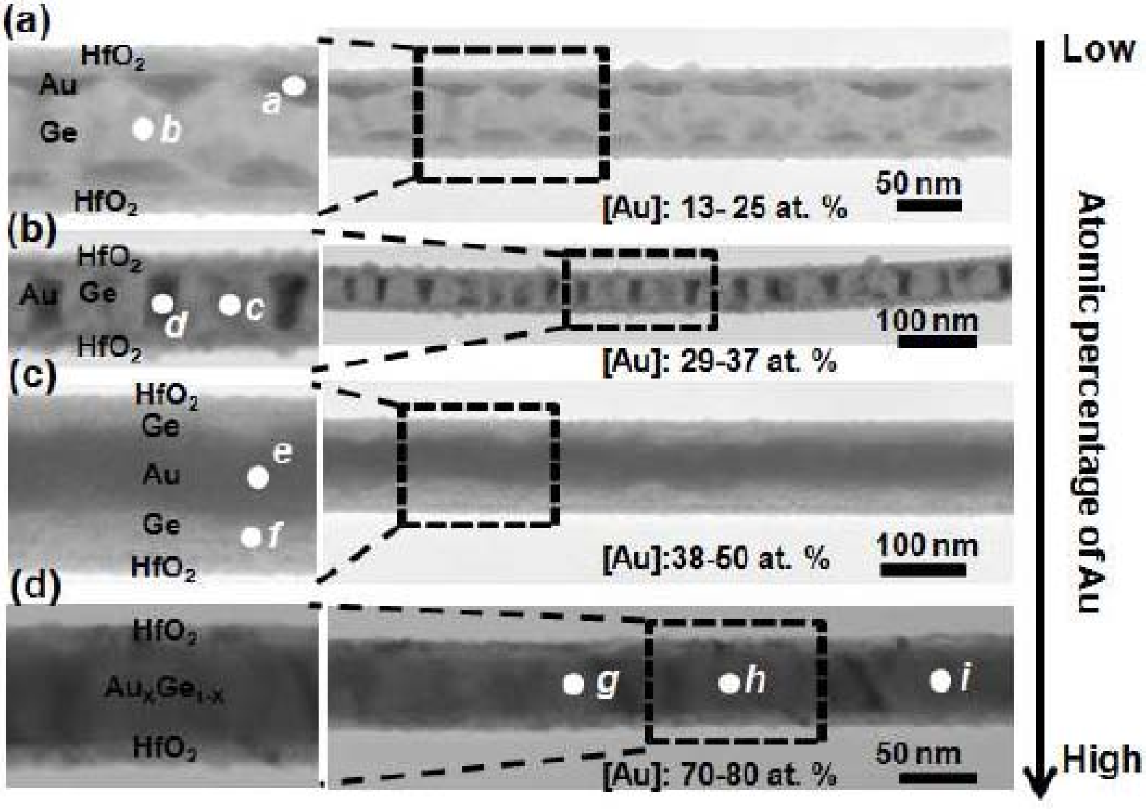

Figure 4.3. HAADF-STEM images of the enabled GeAu nanostructures after thermal annealing at 450 °C for NWs with (a) 13-25 at. %, (b) 29-37 at. %, (c) 38-50 at. %, and (d) 70-80 at. % Au. respectively.

Position	a	b	c	d	e	f	g	h	i
Ge (at.%)	3	98	96	1	6	82	23	28	20
Au (at.%)	97	2	4	99	94	18	77	72	80

Table 4.1. EDX composition analysis of different NW regions as labeled in Fig. 4.3.

4.3. Phenomenological Model

The formation of various NW structures may be understood through consideration of the phase diagram of the Ge-Au system (Fig. 4.1.) and the eutectic solidification and/or solid state diffusion of the corresponding atoms during the cooling step. Specifically, upon heating, a volume fraction of the NWs is molten, the extent of which depends on the Au content and the annealing temperature as governed by the phase diagram. During the subsequent cooling step, phase segregation and, perhaps, solid diffusion of Ge atoms take place for certain structures, resulting in the formation of Au-rich and Ge-rich patterns.

A schematic representation of the proposed formation mechanism of the GeAu nanostructures is shown in Fig. 4.4. Thermal annealing of the samples with low Au concentration (<25 at. %) results in the formation of Au_xGe_{1-x} liquid droplets (Fig. 4.4.(a1)) with the bulk of the Ge remaining in the solid phase. During the cooling step, Au_xGe_{1-x} droplets are solidified and Ge atoms are segregated out of the Au_xGe_{1-x} droplets, resulting in pyramidal shaped features that are Au-rich (Fig. 4.4.(a2)). For samples with 29-37 at. % Au, the resulting Au_xGe_{1-x} droplets are larger in size since a larger volume fraction of the NWs is molten during the thermal annealing step, resulting in the formation of disk-like structures (Fig. 4.4.(b1)), a configuration that presumably minimizes, at least locally, the interfacial free energy.[56] During the cool-down step, Ge atoms segregate out of the Au_xGe_{1-x} regions, resulting in the formation of alternating Ge-rich (96 at. %) and Au-rich (99 at. %) regions (Fig. 4.4.(b2)). For samples with 38-50 at. % Au, Au-Ge core-shell structures were observed. Using the HAADF-STEM image in Fig. 4.3.(c), the radius of the inner Au-rich core and the thickness of the Ge-rich shell were measured to be $r_{Au} = 28.1$ nm and $t_{Ge} = 17.5$ nm, respectively. From this, it was calculated that the NW is composed of ~ 45 at. % Au, consistent with the initial Au sputtering condition. Based on the bulk phase diagram, at 450 °C, this NW consists of 57-75 vol. % Au_xGe_{1-x} liquid alloy with $x \sim 0.67$. The remaining volume is pure Ge solid. In this case, a continuous Au_xGe_{1-x} molten core is formed with a solid Ge shell (Fig. 4.4.(c1)). It is not immediately clear that the observed

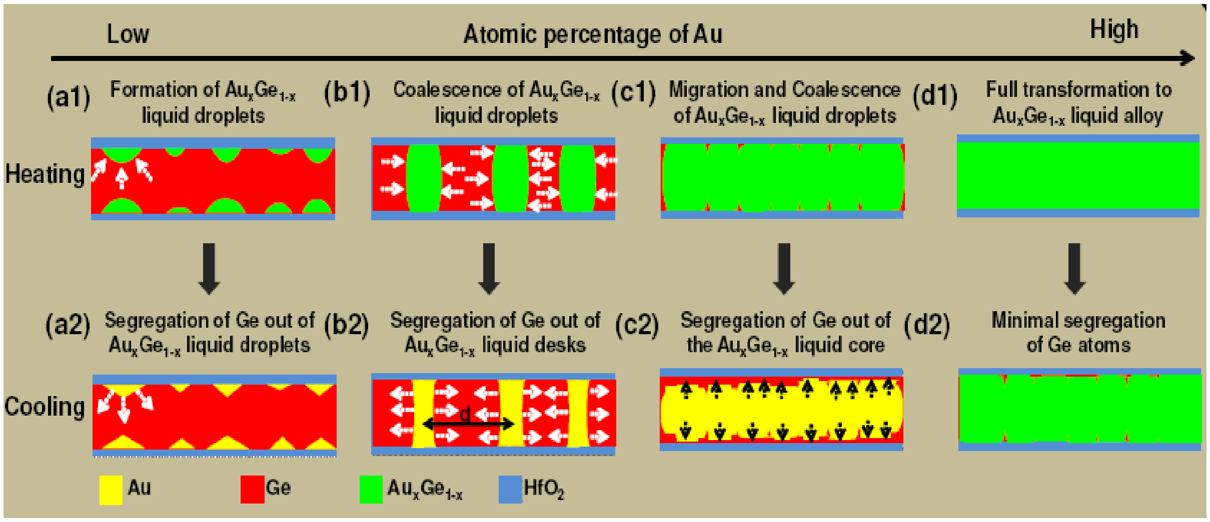

Figure 4.4. Schematic of the proposed formation mechanism for various GeAu nanostructures enabled by thermal annealing process for NW with (a) 13-25 at. %, (b) 29-37 at. %, (c) 38-50 at. %, and (d) 70-80 at. % Au, respectively. (Courtesy of Dr. Yu-Lun Chueh)

configuration represents a global free energy minimum with respect to interfacial free energy, as one might expect the Rayleigh instability to intervene.[90] However, the Rayleigh instability may be suppressed by the constraint of the outer shell, and/or the observed configuration may well be a local free energy minimum. Once again, during the cool-down step, solid-state diffusion of Ge out of the Au_xGe_{1-x} core takes place, resulting in the formation of a Au-rich core and a Ge-rich shell (Fig. 4.4.(c2)). Finally, when the Au content is increased to 70-80 at. %, which is near the eutectic point for the bulk Ge-Au system, the NWs are fully molten at 450 °C, resulting in the formation of fully alloyed NWs (Fig. 4.4.(d1)). In this case, minimal phase segregation and solid-state diffusion of Ge from the alloy is observed during the cool-down step presumably due to the lack of solid Ge nucleation sites to facilitate the process (Fig. 4.4.(d2)). Apparently, the cooling rate is fast enough, and the solidification temperature is low enough such that the structure is kinetically limited to remain alloyed.

To further investigate the segregation behavior during the cool-down step, *in-situ* TEM studies of NW samples with 29-37 at. % Au were conducted using the JEOL 3010 microscope equipped with a heating stage. In this case, the total volume of regions 1, 2, and 3 (Au_xGe_{1-x} nanodisk regions) in Fig. 4.5.(a1) at different temperatures was measured, summed, and plotted, as shown in Fig. 4.5.(b). The total volume of the disk patterns decreased by ~2 times as the temperature was reduced from 500 °C to ~200 °C, beyond which minimal volume change is observed. Notably, the phase diagram governing our NWs appears near that of the bulk eutectic alloy as determined from the temperature dependency of the volume of Au_xGe_{1-x} droplets.

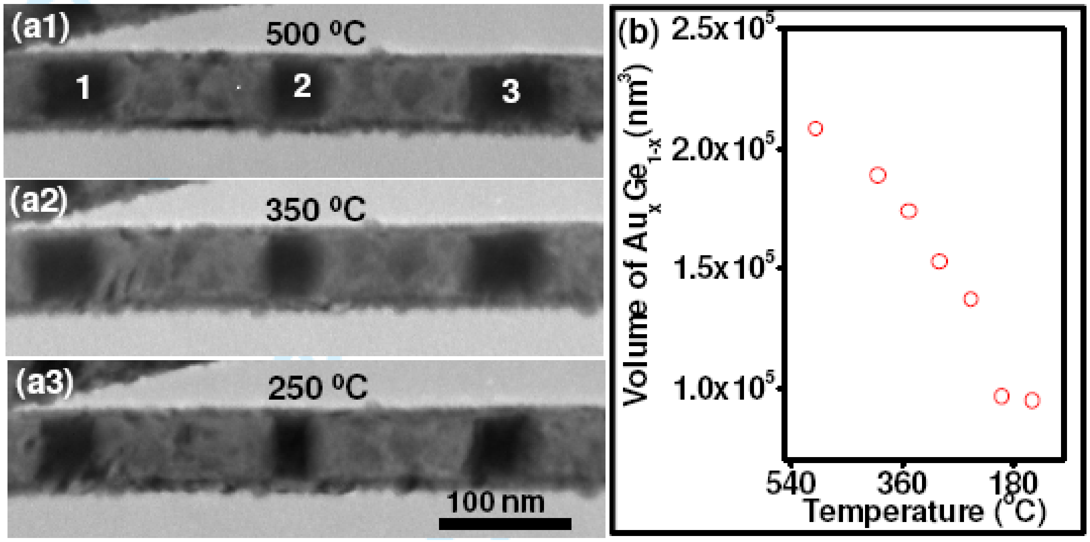

Figure 4.5. *In-situ* TEM analysis for a NW with 29-37 at. % Au at different temperatures. The images were captured during cool-down step. (b) The total volume of regions 1, 2, and 3 as a function of temperature.

The volume vs. temperature curve varies smoothly between 500 ºC and 200 °C suggesting that the eutectic liquid may be supercooled, as has been observed in free standing Au-Ge alloys.[91] The strong segregation likely occurs upon solidification of the supercooled liquid eutectic alloy. We note that the solid-state diffusion of Ge atoms out of the Au_xGe_{1-x} regions may also account for the observed segregation. In either case, the result is the formation of crystalline, lens-shaped regions of nearly pure Au. At lower temperatures (<200 °C), the diffusion of Ge atoms is minimal, and the Au_xGe_{1-x} volume remains constant (Fig. 4.5.(b)). This result provides a strong support for the proposed mechanism of the GeAu nanostructure formation, involving first the formation of liquid Au_xGe_{1-x} alloys at elevated temperatures, followed by the segregation of Ge out of the alloy during the cool down step. Furthermore, the *in-situ* TEM analyses confirm that the alloyed droplets remain in their original positions up to a temperature of 500 °C, even when the annealing time is 1 hour, and also during the cooling process (Fig. 4.5.(a2),(a3)).

Chapter 5

Radiation Induced Nanostructure Formation

5.1. Electron Beam Induced SiO_2/Ge Nanorods Formation

5.1.1. Introduction

As introduced in Chapter 1, significant portions of embedded nanocrystal studies have been motivated by its potential application to optical devices[92-94] and charge storage devices.[40, 95, 96] Among various synthesis methods, IBS has a great advantage in its compatibility with existing large scale semiconductor production technology. However, the nanocrystal formation process is governed by diffusion and coarsening of the implanted species in the matrix during post-implantation annealing, and it is difficult to control the final size, density, and distribution of the nanocrystals. To better understand the cluster forming mechanism and elucidate the governing process parameters are in that sense very important as described in Chapter 2.3.2.

On the other hand, more direct methods to control the size and distribution of the nanocrystals have been attempted.[97-99] For example, Sharp et al.[100] used a stencil mask and oxygen co-implantation to form patterned arrays of Si nanocrystals. The chemical deactivation was achieved by oxygen co-implantation, and the average nanocrystal size could be controlled by tuning the Si/O or Ge/O ratios, while the nanocrystal location could be chosen with the mask. The scalability when using a patterning mask, however, is limited by the mask edge effect due to the lateral straggling of the implanted species, typically in ~100 nm range.

Here, we try another direct method to fabricate nanostructures using direct electron beam lithography (EBL) patterning onto the sample. An electron beam will be used to nucleate the implanted species instead of performing a high temperature post-implantation annealing. It was shown earlier that electron beam can cause moving of clusters or atoms on a surface[101] or solid state reactions.[102] Precipitation of Ge nanoclusters by e-beam irradiation was also reported by Klimenkov et al.[103] in Ge implanted SiO_2 thin films, and by Jiang et al.[104] in Ge-doped SiO_2 glass. The observations were all made under TEM electron beam irradiation.

In the current study, we use the focused electron beam of an e-beam writer to locally induce nucleation of the implanted Ge atoms. The focused electron beam typically used for EBL is on the order of a few nm, much smaller than the spatial limit of mask patterning, and if we use an electron beam for forming nanocrystals, it may open up the possibility to form nanocrystals at low temperature without high thermal budget.

5.1.2. Experimental Procedure

^{74}Ge was implanted into 500 nm thick thermally grown SiO_2 layers on a Si substrate. The lowest reliable implantation energy for Varian CF 3000 implanter, 32 keV, was used with a total dose of 5×10^{15} cm^{-2}. It was reported that 20 keV, 5×10^{15} cm^{-2} implantation provides enough Ge concentration for nanocrystals formation.[103] The expected ^{74}Ge distribution profile simulated using PC-257 Profile Code^{TM} is presented in Fig. 5.1. The electron beam energy of the e-beam writer, 100keV, has lower energy than the 200~300 keV TEM beam reported in the literature. The lowest ion beam energy was used to maximize irradiation effects near the surface.

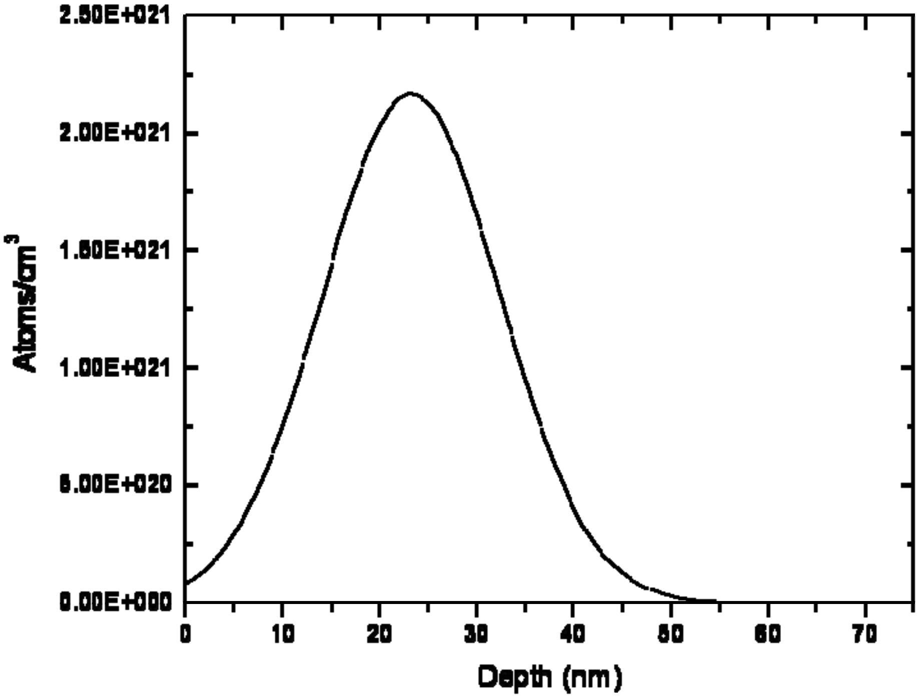

Figure 5.1. Expected ^{74}Ge profile in 500nm SiO_2 layer simulated with PC-257 Profile Code^{TM}. Implantation energy and dose were 32 keV, 5×10^{15} cm^{-2}, respectively.

Alignment marks patterning and electron beam irradiation experiments were conducted in the center for X-ray optics (CXRO) at Lawrence Berkeley National Laboratory under supervision of Dr. Erik Anderson and Dr. Alexander Liddle. Three rectangular (4μm× 2μm) Au alignment marks were patterned to find the irradiated area with an atomic force microscope (AFM) and a scanning electron microscope (SEM) after irradiation. First, 300 nm thick KRS-XE positive e-beam resist was spin coated and baked for 3 minutes. As a second step, the electron beam irradiated 4μm× 2μm rectangular patterns using the Leica VB6-HR Nanowriter, and the resist film was developed in LDD 26W solution to etch off the irradiated area. For the last step, a 5 nm Cr adhesion layer and 50 nm Au pattern layer were deposited by thermal evaporation, and the remaining resist was lifted off with acetone to finally reveal the rectangular shaped Au alignment marks. Finally, the 100 keV Nanowriter electron beam was directed to the active area (2μm×2μm) to nucleate implanted Ge atoms. We exposed 10×10 spots with a 10 nm diameter beam, and the spots were located 100 nm apart. The total dose for each spot was set to 3.2×10^4 C/cm^2, giving 64 seconds resident time for each spot with a beam current of 500 pA.

For the characterization, we used Raman spectroscopy to detect Ge crystallization inside SiO_2. To directly observe the nanocrystals with AFM and SEM, matrix SiO_2 was etched away by 1:1 ratio of 49% HF:H_2O solution.[64] Energy dispersive X-ray spectroscopy (EDX) measurements were also performed for chemical analysis.

5.1.3. Results and Discussions

An AFM image of the e-beam irradiated sample after HF etching is shown in Fig. 5.2.(a). Surprisingly, it shows that nanorod structures, instead of expected nanocrystals, were formed. For comparison, an image of the as-implanted sample after HF etching, and an implanted and annealed (900 °C, 1 hour) sample after HF etching are shown in Fig. 5.2.(b) and (c), respectively. Random shape debris or impurities possibly from non-etchable Ge or SiO_2 phases are present in Fig. 5.2.(b), and agglomerated Ge nanocrystals that were observed in typical IBS Ge nanocrystals grown by thermal annealing[42] can be seen in Fig. 5.2.(c). This observation implies that the original amorphous SiO_2 phase transformed into another phase or material upon irradiation which is HF resistive.

Since the height of the Au alignment marks was only 50 nm, we know from comparing the height of exposed Si substrate and that of Au patterned regions that even the SiO_2 below Au layers was totally etched away through undercutting. This confirms the argument that the nanorod structure is not the same amorphous SiO_2 anymore. The diameter of the rod increases from ~10 nm at the top section, which corresponds to the e-beam spot size, to ~100nm, which is the spacing between each spot. However, considering the fundamental limitation of AFM measurements due to the tip geometry, especially for high aspect ratio structures, image dimensions of the side walls and trenches between the rods are not reliable. To complement this limitation, a SEM image was taken as shown in Fig 5.4. The nanorods with a uniform aspect ratio can be clearly observed, which verifies the uniform rod-like geometry. It can be also seen that the total thickness is reduced to below 200 nm from the original 500nm SiO_2 thickness. It suggests that part of the SiO_2 matrix, which is not affected by the electron beam, is either desorbed or etched away. It can also be used to get additional information about the effective penetration depth of the electron beam in the current system.

We performed Raman spectroscopy and EDX measurements to investigate the chemical nature of the structure. From the Raman measurement, we could not detect any crystalline Ge Raman signal, meaning Ge nanocrystals are not formed at least by detectable amounts. An EDX result is shown in Fig. 5.5. Ge is hardly detected as in Raman, and more importantly, the O peak is also invisible. Although a more sensitive measurement is necessary, we can suggest the formation of an oxygen deficient structure by e-beam irradiation.

Electron-SiO_2[105-108] and electron-Ge embedded SiO_2[103] interactions have long been studied. The former studies were all performed with a 100 keV electron beam, which is the same as in the current experimental condition. Chen et al.[105, 106] observed an EELS plasmon peak shifted from SiO_2 22.9eV to Si 16.7eV, and Si L-edge from 108eV to 99eV as electron beam dose increases up to 3×10^5 cm^{-2}. Takeguchi et al.[107] acquired the same EELS result with quartz single crystal SiO_2 at 850 K. Single crystal SiO_2 was first amorphized and then formed Si-phase nanocrystals at beam dose of 1.6×10^5 C/cm^2. They both attributed this effect to electron stimulated desorption (ESD) mechanism suggested by Knotek and Feibelman.[109]

When implanted Ge was additionally involved,[103] Ge nanoclusters were formed at a 3.2×10^4 C/cm^2 dose and nanocrystals at 8×10^4 C/cm^2 at the peak region of the distribution profile. The shrinkage of the SiO_2 layer mainly caused by oxygen out-diffusion was also observed, which is consistent with the cases without Ge. Since Ge is much heavier than Si and O, and has a smaller energy transfer per electron collision, Ostwald ripening of Ge clusters subsequent to Si, O displacement is the most persuading mechanism for nanocrystal formation as in the case of the widely studied electron-beam-induced epitaxial recrystallization (EBIEC).

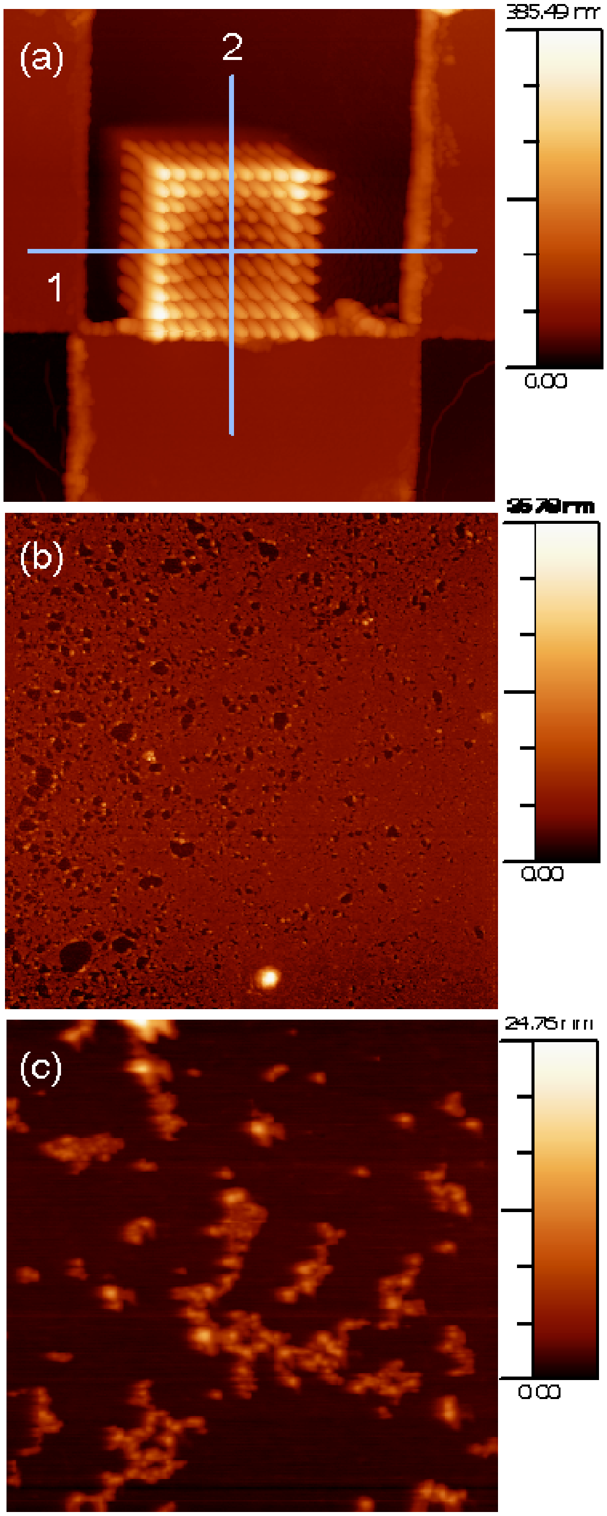

Figure 5.2. AFM images of (a) irradiated sample after etching (3µmx3µm), (b) non-irradiated part of the sample after etching (5µmx5µm), (c) non-irradiated part of the sample, annealed at 900 °C for 1hour and etched (5µmx5µm).

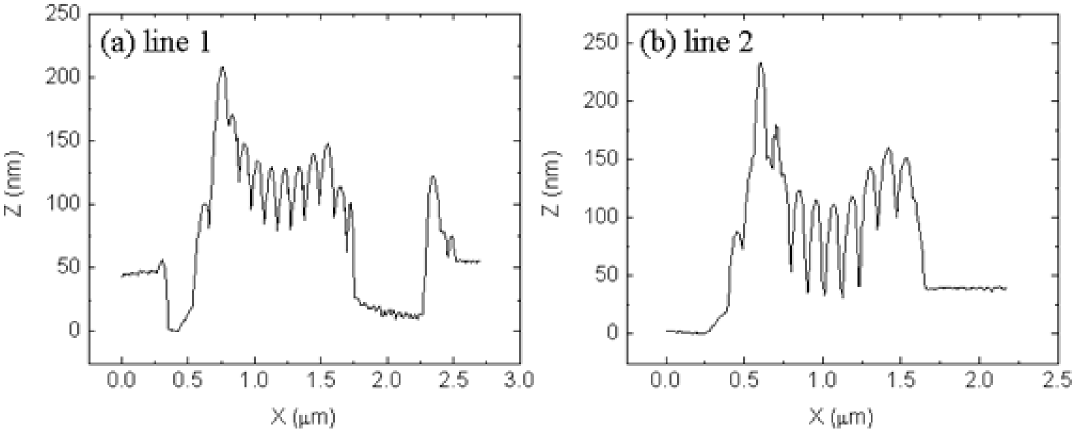

Figure 5.3. AFM line profile of line 1 and line 2 in Fig. 5.2.(a).

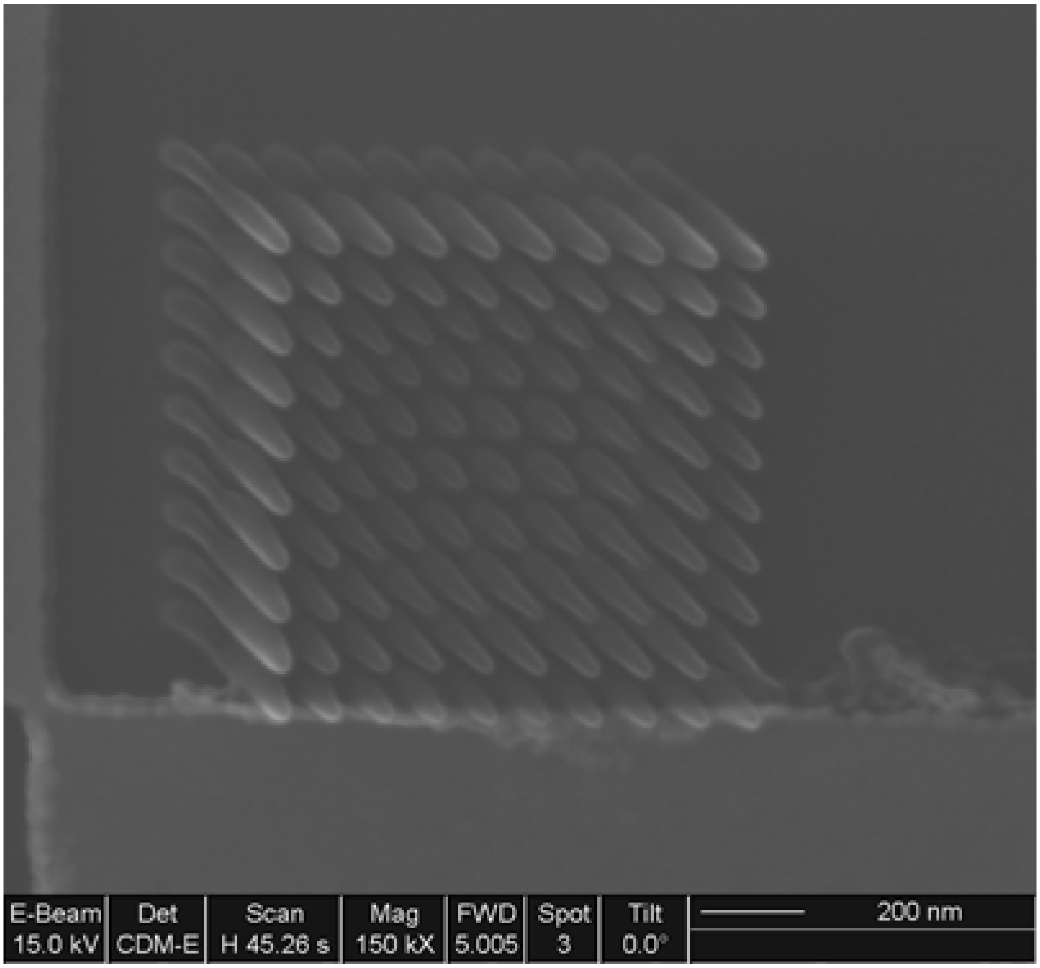

Figure 5.4. SEM image of Fig. 5.2.(a). Rods with a uniform aspect ratio can be clearly observed.

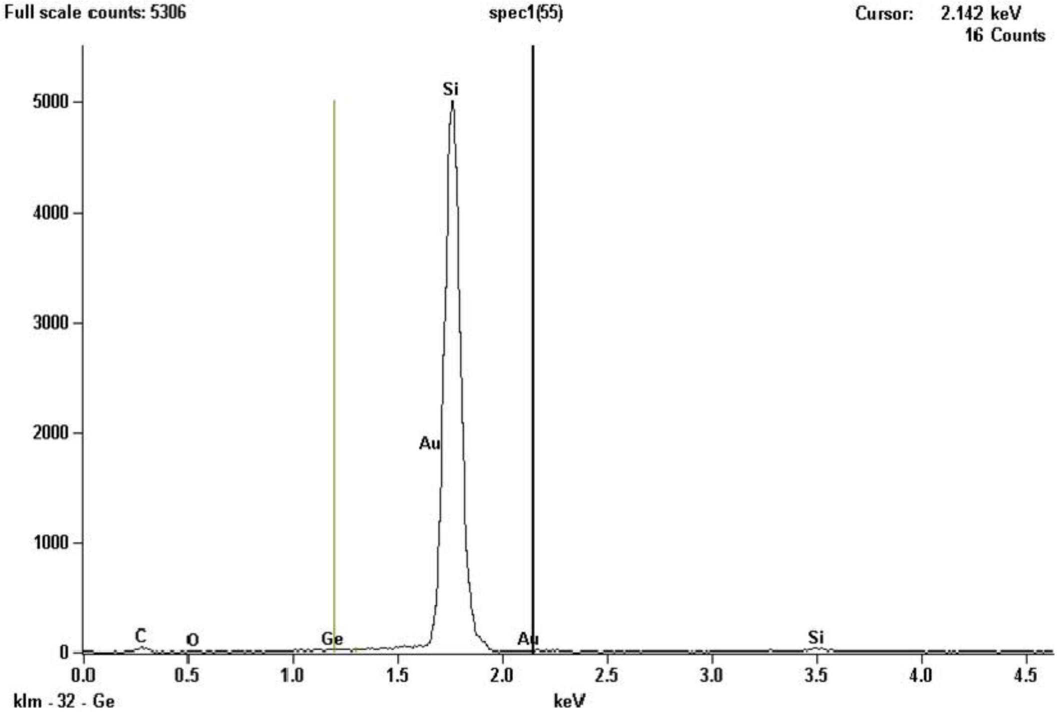

Figure 5.5. EDX spectrum of the e-beam induced nanorods. 32 keV beam energy was used.

From the previous studies, we can suggest the formation mechanism and deduce a chemical nature of the nanorod structure. The electron energy is thought to be transferred foremost to Si and O atoms, and cause atomic displacement, and form a new oxygen deficient phase which is HF resistive. Implanted Ge atoms are expected to ripen and form non-crystalline clusters inside the matrix and may affect the etch-resistive nature of the structure, but further investigations such as cross sectional TEM and EDX are needed.

5.2. GeSn Core-Shell Nanocrystal Formation

In Chapter 3, we showed reversible phase transformations of embedded $Ge_{1-x}Sn_x$ nanocrystals when they go through as-formed, PLM, and post-PLM RTA processes. It was also shown that the stable, equilibrium morphology consists of phase-separated bi-lobe shaped nanocrystals, and the interface energies between phases were estimated based on Young's equation in Chapter 2.4.3.

Specifically, for $Ge_{0.8}Sn_{0.2}$ nanocrystals, post-PLM RTA at 500 °C for 10 sec returned the homogeneously mixed structure back to the equilibrium bi-lobe structure as shown in Fig. 3.10. It was reproducible for a number of repetitive experiments except for an earlier experiment with slightly different TEM sample preparation conditions. It is worth discussing the results and implications.

TEM specimens are thinned down to ~10 μm in thickness before they are inserted into ion miller where spatially spreaded energetic argon ion beams (typically 5 keV) hit the specimen at low angle until a hole is drilled at the thinnest region. During the ion milling process, the sample stage is kept cold with liquid nitrogen to avoid ion beam heating effects and/or damage to the sample at elevated temperature. Most of the TEM specimens reported in this dissertation were made that way using a Fischione 1010 ion miller. For a few earlier experiments, a focused ion beam without a cold stage was used to make TEM samples. (Gatan PIPS) Although not measured or verified, it is believed that the specimen temperature reaches much higher values than when using the Fischione ion miller due to the high beam intensity and lack of a cold stage. In fact, the PIPS ion miller is approximately 10 times faster than Fischione. The implication is that the argon beam might affect the final morphology of the nanocrystals due to ion bombardment of the nanocrystals at an elevated temperature.

In Fig. 5.6. HAADF-STEM images show the results of the experiment: $Ge_{0.8}Sn_{0.2}$ nanocrystals annealed at 900 °C for 1 hour, PLM, and post-PLM RTA at 500 °C for 10 sec. Ion milling was performed in a Gatan PIPS ion miller with a focused argon ion beam. Surprisingly, it produced core-shell nanocrystals. They are clearly phase segregated into core and shell, and both Sn core-Ge shell and Ge core-Sn shell nanocrystals are observed as in (a) and (b), respectively. Although only one equilibrium configuration may exist for a specific embedded binary nanocrystals system as could be predicted by the magnitudes of the interface energies,[56] Strobel et al.[55] used a 3-D lattice Monte Carlo simulation to show that when the bond strength, thus the tendency of mixing between all elements is similar, the final structures are mainly determined by kinetic effects.

HRTEM images of the same specimen as in Fig. 5.6.(a) are presented in Fig. 5.7. They show that core-shell nanocrystals consist of a number of randomly oriented small grains, which suggests ion bombardments might have caused amorphization followed by recrystallization and/or rearrangements of the crystalline Ge/Sn phases. Although the formation mechanism of the core-shell GeSn nanocrystals is not well understood, and the processing control is rather poor, it may suggest that a kinetically limited structure can be created by ion beam irradiation as well as by controlling the cooling rate.

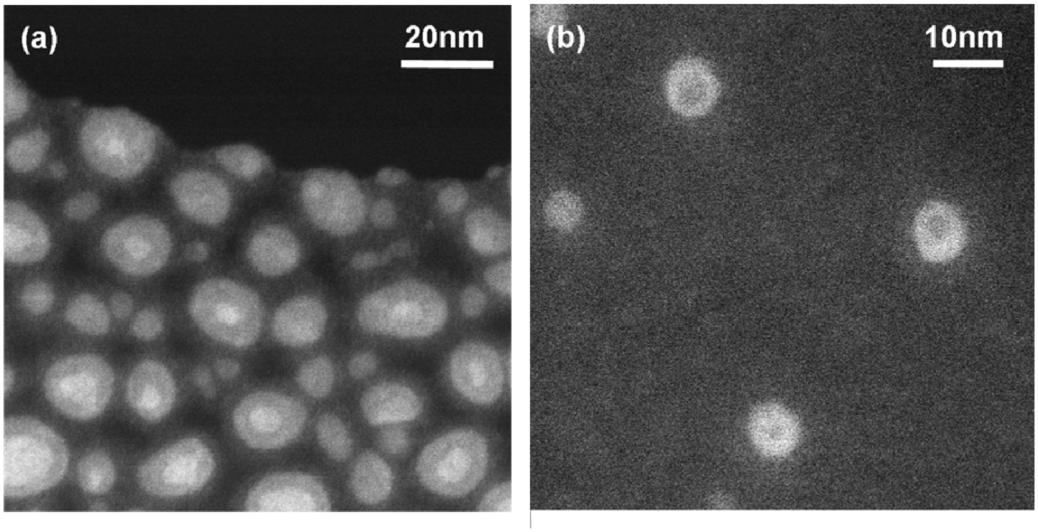

Figure 5.6. Planview HAADF-STEM images of core-shell nanocrystals. (a) Sn core-Ge shell and (b) Ge core-Sn shell nanocrystals.

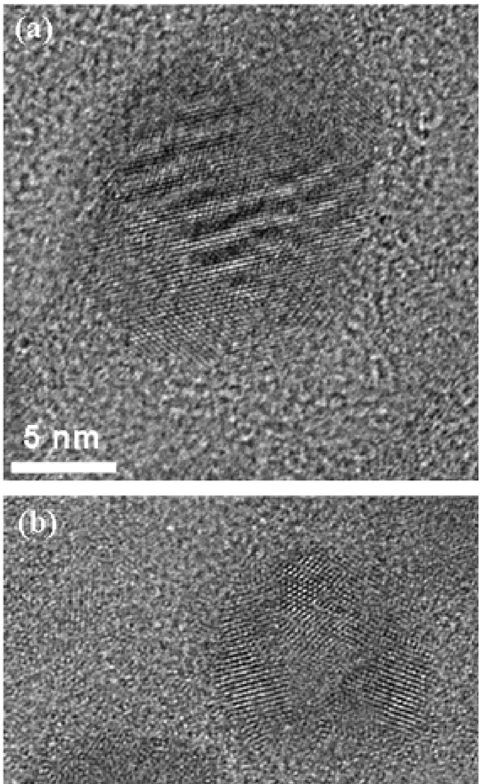

Figure 5.7. HRTEM images of the Sn core- Ge shell $Ge_{0.8}Sn_{0.2}$ nanocrystals. Moire fringes are observed in (a).

Chapter 6

Conclusions and Future Work

6.1. Conclusions

The research presented in this dissertation was focused mainly on understanding the formation and phase transformations of Ge based nanostructures using complementary characterization techniques and theoretical analysis.

IBS and sputtering methods to fabricate embedded nanocrystals were presented, and an experimental strategy based on theoretical simulation to narrow down the inherently wide size distribution of IBS method was suggested with preliminary experimental results. Demonstration of the size control, especially narrowing the distribution, would significantly accelerate utilization of IBS in making nanostructures and applying them to functional devices.

Formation of the GeSn binary eutectic alloy nanocrystals was shown, and its thermodynamic implications that are applicable to general binary eutectic alloy systems were presented. It was demonstrated that a metastable state could be formed with a single short laser pulse, and the composition dependent equilibrium and kinetic aspects of phase transformation were discussed. Based on the results, a new type of phase change material that enabled to tune phase equilibria and transition kinetics at the nanoscale - binary eutectic alloy nanostructures (BEANs) - was proposed. In one-dimensional BEANs, GeAu nanowires, composition dependent post-growth engineering produced various types of final morphologies due to the effectively infinite length for atomic diffusion in one direction. The presented BEANs approach provides potential implications for applications in phase change memory, optoelectronic, and electronic devices.

Looking ahead to the applications of BEANs to data storage, we note that at this time, it is not possible to characterize directly the transport properties of the bi-lobed and amorphous nanostructures. We note, however, that the resistivity between amorphous and crystalline Ge films differ by four orders of magnitude,[110] and there is theoretical evidence that the band gap of $Ge_{1-x}Sn_x$ can be reduced substantially from that of pure Ge.[111] Thus we expect that the transport and optical properties of the amorphous PLM structure will be different from those of the bi-lobed structure, and further that these differences can be tuned through a choice of composition.

6.2. Future Work

The composition dependent equilibrium and kinetic aspects of zero, and one dimensional binary eutectic alloy nanostructures (BEANs) were explored, but the precise origin and mechanism of each phenomenon are yet to be investigated. A good approach would be to explore the nanoscale phase diagram for a specific eutectic alloy system. As reported by Sutter et al.,[91] small dimensions and confined geometry can alter the bulk phase diagram. BEANs can provide an ideal platform to elucidate nanoscale phenomena and build a nanoscale phase diagram that could be used as a guideline to design nanoscale devices. Diffraction intensity studies on heating/cooling cycles of embedded GeSn and GeAu nanocrystals are in progress, and they will provide useful insights.

The desired characteristics of BEANs as potential applications to devices would be a large change in their structure dependent physical properties. Since IBS nanocrystals can be embedded practically in any medium, it is useful to explore the contrast between optical absorption, photoluminescence and/or reflectance of each structure. The positions of the bulk plasmon peaks were modified in our GeSn nanocrystals experiment, and it is very likely that the fundamental bandgaps have been modified as well. NWs serve best as a channel for carrier transport. Transport properties of different materials system will also be explored.

Appendices

A. Rutherford Backscattering Spectrometry

Rutherford backscattering spectrometry (RBS) is a powerful non-destructive method to measure the elemental, compositional, concentration distribution of multiple atomic species in the sample. A sample is bombarded with high energy He^+ ions generated from an accelerator. A very small fraction of the bombarding ions are backscattered by the atomic nuclei, and a combination of the backscattered ion energy, yield, and energy loss through the target provide the information to extract the atomic distribution. Each contribution can be described by the following step by step process.

1. Kinematic factor, K (atomic mass determination)
Elastic energy transfer from a projectile to a target atom can be calculated with simple collision kinematics. Using the law of conservation of energy and momentum, the kinematic factor K can be described as:

$$K_{m_2} = \frac{E_1}{E_o} = [\frac{\sqrt{(m_2^2 - m_1^2 \sin^2 \theta)} + m_1 \cos\theta}{(m_2 + m_1)}]^2 = K(\theta, m_2, m_1)$$

where E_o: incident ion energy, E_1: backscattered ion energy, m_1: incident ion mass, m_2: target element mass, θ: backscattering angle.

When $m_2 >> m_1$, $K_{m_2}(\theta = 180°) \sim 1$, and all the other values except for m_2 are either known or are directly measured, thereby the mass of the target element can be calculated. K_{m_2} for most elements is well known and tabulated. For multi-element targets, RBS spectra show multiple peaks corresponding to the elements in the target material.

2. Scattering cross-section, σ (quantitative analysis of atomic composition)
The probability of the elastic collision between the projectile and target atoms can be calculated to find the atomic composition of the sample from the measured relative spectral intensities. It requires the use of the differential scattering cross-section, $\frac{d\sigma}{d\Omega}$.

$$\frac{d\sigma}{d\Omega} = (\frac{Z_1 Z_2 e^2}{2E_o})^2 \frac{[\cos\theta + (1 - A^2 \sin^2 \theta)^{1/2}]^2}{\sin^4(\frac{\theta}{2})(1 - A^2 \sin^2 \theta)^{1/2}}$$

with Z_1, Z_2: atomic numbers of the incident and target atom, respectively,
σ: scattering cross-section, Ω: detector solid angle, A: backscattering yield.

The backscattering yield A is the measured spectral intensity in the experiment that in turn can be expressed as:

$$A = \sigma_{ave} \Omega N Q$$

where, σ_{ave} : average cross-section, Q : number of incident ions, N : atoms/cm^2.

Therefore, N can be calculated for each element, and the composition can be determined.

3. Energy loss, $\dfrac{dE}{dx}$ (depth perception)

Both incident and scattered ions lose energy as they pass through the sample mainly due to electronic stopping. This inelastic energy loss can be used to determine the depth of the atoms within the sample. Total energy loss of the projectile ΔE is expressed as:

$$\Delta E = KE_o - E_1 = \left(\frac{K}{\cos\theta_1}\frac{dE}{dx}\Big|_{E_o} + \frac{1}{\cos\theta_2}\frac{dE}{dx}\Big|_{KE_o}\right)t = [S_o]t$$

with θ_1, θ_2 : incident and scattered angle, respectively, S_o : effective stopping power, t: sample thickness. t can be expressed as:

$$t = \frac{\Delta E}{[S_o]} = \frac{\Delta E}{N[\varepsilon_o]}$$

where, ε_o is the stopping cross-section.

ε_o is obtained from the TRIM code or empirical energy loss data fitting, therefore the thickness or depth can be determined. More detailed information can be found in Ref.[112]

B. Extended X-ray Absorption Fine Structure

Extended x-ray absorption fine structure (EXAFS) is one of the regimes of a more general concept, x-ray absorption fine structure (XAFS). XAFS refers to the details of how x-rays are absorbed by atoms at energies near and above the core level binding energies of that atom. Basically, an atom's x-ray absorption probability is modulated by the presence of the neighboring atoms, and the resulting spectrum is sensitive to the oxidation state, coordination number, distances, and species of the atoms surrounding the selected element. Since XAFS has few constraints on the samples that can be studied, it is used in many fields including materials science, chemistry, and biology. Especially, crystallinity is not required, which makes it one of the most appropriate structural characterization techniques for amorphous materials. The basic principles are rather simple, but the accurate theoretical understanding is quite involved and still being developed. In this appendix, a brief introduction to the principles of EXAFS and data reduction process will be provided. A complete description can be found in Ref.[113-116]

XAFS is divided into two regimes: x-ray absorption near-edge spectroscopy (XANES) for energies within 30 eV from the absorption edge and EXAFS for energies well above the absorption edge. XANES is sensitive to the oxidation state and coordination chemistry while EXAFS is used to determine the distances, coordination numbers, and species of the neighboring atoms. When discussing x-ray absorption, the absorption coefficient μ has to be introduced using Beer's law:

$$I = I_o \exp(-\mu t)$$

with I_o: incident x-ray intensity, I : transmitted x-ray intensity, t: sample thickness.

At most x-ray energies, the x-ray absorption coefficient μ is a smooth function of energy except for the case where the x-ray energy is equal to that of the binding energy of a core electron. There is a sharp rise in μ, an absorption edge where the core electron is excited to the continuum state. In XAFS, we are concerned with the intensity of μ as a function of energy near and above the absorption edge. Specifically for EXAFS, we are interested in the oscillations of μ well above the edge, and we define the EXAFS fine structure function $\chi(E)$ as:

$$\chi(E) = \frac{\mu(E) - \mu_o(E)}{\Delta\mu_o(E)}$$

with $\mu(E)$: measured absorption coefficient, $\mu_o(E)$: smooth background function representing absorption from an isolated atom, $\Delta\mu_o(E)$: measured jump in the absorption $\mu(E)$ at the threshold energy E_o.

Since EXAFS is best understood in terms of the wave behavior of the photo-electron, it is common to convert $\chi(E)$ into $\chi(k)$ with the well-known relationship $k = \sqrt{\frac{2m(E - E_o)}{\hbar^2}}$. The different frequencies in the oscillations of $\chi(k)$ correspond to near neighbor coordination shells which can be described and modeled according to the EXAFS equation:

$$\chi(k) = \sum_j \frac{N_j e^{-2k^2\sigma_j^2} e^{-2R_j/\lambda(k)} f_j(k)}{kR_j^2} \sin[2kR_j + \delta_j(k)]$$

with $f(k)$: scattering amplitude, $\delta(k)$: phase-shift (both are scattering properties)
N : number of neighboring atoms, R : distance to the neighboring atom,
σ^2 : disorder in the neighbor distance.

Knowing $f(k)$ and $\delta(k)$ (typically from calculations using a program such as FEFF), the above EXAFS equation allows us to determine N , R , and σ^2 . Also, since scattering factors depend on Z of the neighboring atoms, EXAFS is also sensitive to the atomic species.

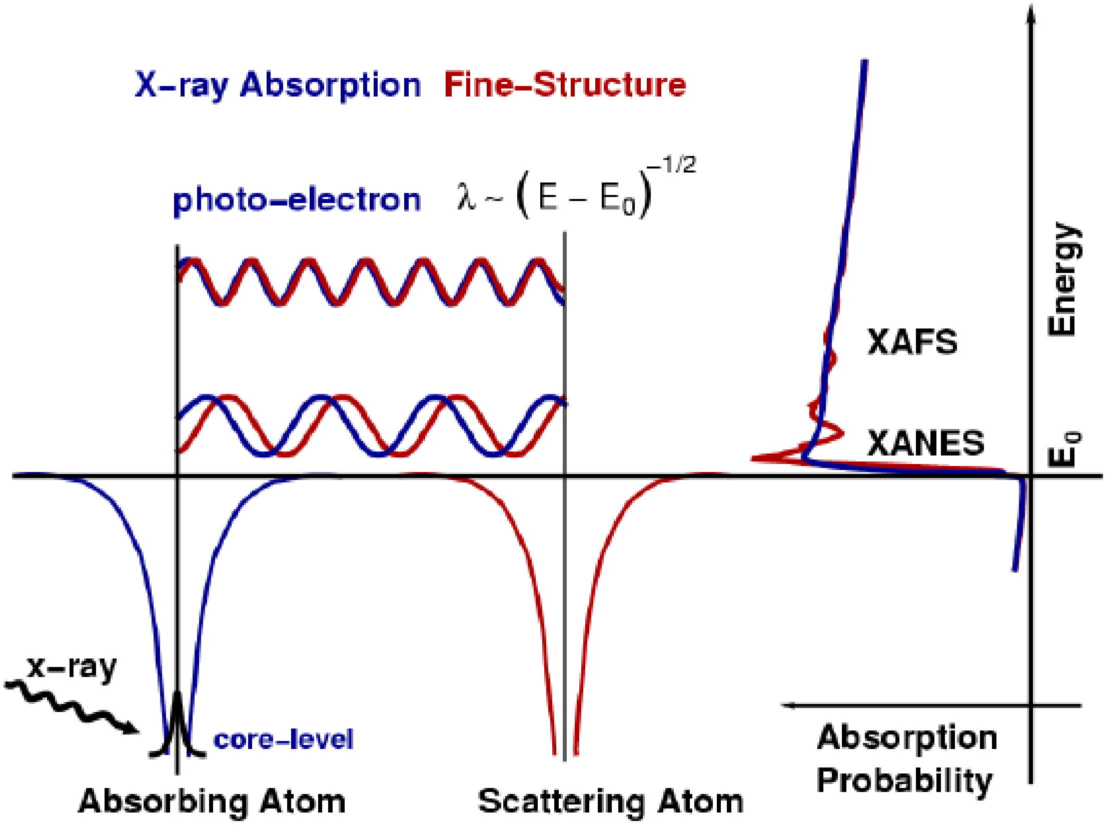

Figure B.1. Schematic diagrams of the XAFS process. The scattered photo-electron can return to the absorbing atom, modulating the amplitude and phase of the photo-electron wave function at the absorbing atom. This modulates $\mu(E)$, causing EXAFS.[113]

For EXAFS data reduction, it is natural to have Fourier transform involved because EXAFS oscillations consist of different frequencies that correspond to the different distances for each coordination shell. The data reduction process can be summarized as follows:

1. Convert the measured intensities to $\mu(E)$ and correct systematic errors, if any.
2. Subtract a smooth pre-edge function from $\mu(E)$ to remove instrumental background and absorption from other edges.

3. Identify E_o by taking the maximum derivative of $\mu(E)$.
4. Normalize $\mu(E)$ to go from 0 to 1, which represents the absorption of 1 x-ray.
5. Remove a smooth post-edge background function to approximate $\mu_o(E)$.
6. Isolate $\chi(k)$ from $\mu(E)$.
7. k -weight the $\chi(k)$ and Fourier transform into R -space.

The final process for EXAFS analysis is structural refinement through data modeling. Programs such as SixPACK and ATHENA/ARTEMIS are used. With the calculated $f(k)$ and $\delta(k)$, we can use the EXAFS equation to predict and modify N , R , and σ^2 , and change E_o until we find the best fit to the $\chi(k)$ data. Since Fourier transform is available, we can do the refinement in both k -space and R -space. When analyzing in R -space, the full complex $\chi(R)$ must be used. We can fit one shell at a time, and add them up for the final fit. Standard signal analysis tells us that the maximum numbers of free variables that can be effectively fit in a refinement depends on the considered k and R ranges. It turns out the maximum number of parameters that can be determined from an EXAFS spectrum is about $N_{\max} \Delta k \Delta R \pi$ for k -range Δk , and R -range ΔR .

Bibliography

[1] I. C. Freestone, N. Meeks, M. Sax, and C. Higgitt, "The Lycurgus Cup - A Roman Nanotechnology," *Gold Bulletin*, vol. 40, pp. 270-277, 2007.

[2] D. J. Barber and I. Freestone, "An investigation of the origin of the colour of the Lycurgus Cup by analytical transmission electron microscopy," *Archaeometry*, vol. 32, pp. 33-45, 1990.

[3] P. Buffat and J.-P. Borel, "Size effect on the melting temperature of gold particles," *Physical Review A*, vol. 13, pp. 2287 LP - 2298, 1976.

[4] A. N. Goldstein, C. M. Echer, and A. P. Alivisatos, "Melting in semiconductor nanocrystals," *Science*, vol. 256, pp. 1425, 1992.

[5] M. Schmidt, R. Kusche, B. von Issendorff, and H. Haberland, "Irregular variations in the melting point of size-selected atomic clusters," *Nature*, vol. 393, pp. 238-240, 1998.

[6] T. Castro, R. Reifenberger, E. Choi, and R. P. Andres, "Size-dependent melting temperature of individual nanometer-sized metallic clusters," *Physical Review B*, vol. 42, pp. 8548 LP - 8556, 1990.

[7] S. L. Lai, J. Y. Guo, V. Petrova, G. Ramanath, and L. H. Allen, "Size-Dependent Melting Properties of Small Tin Particles: Nanocalorimetric Measurements," *Physical Review Letters*, vol. 77, pp. 99 LP - 102, 1996.

[8] L. Landin, M. S. Miller, M.-E. Pistol, C. E. Pryor, and L. Samuelson, "Optical Studies of Individual InAs Quantum Dots in GaAs: Few-Particle Effects," *Science*, vol. 280, pp. 262-264, 1998.

[9] V. I. Klimov, A. A. Mikhailovsky, S. Xu, A. Malko, J. A. Hollingsworth, C. A. Leatherdale, H.-J. Eisler, and M. G. Bawendi, "Optical Gain and Stimulated Emission in Nanocrystal Quantum Dots," *Science*, vol. 290, pp. 314-317, 2000.

[10] S. Coe, W.-K. Woo, M. Bawendi, and V. Bulovic, "Electroluminescence from single monolayers of nanocrystals in molecular organic devices," *Nature*, vol. 420, pp. 800-803, 2002.

[11] S. Tiwari, F. Rana, H. Hanafi, A. Hartstein, E. F. Crabbe, and K. Chan, "A silicon nanocrystals based memory," *Applied Physics Letters*, vol. 68, pp. 1377-1379, 1996.

[12] D. N. Kouvatsos, V. Ioannou-Sougleridis, and A. G. Nassiopoulou, "Charging effects in silicon nanocrystals within SiO[sub 2] layers, fabricated by chemical vapor deposition, oxidation, and annealing," *Applied Physics Letters*, vol. 82, pp. 397-399, 2003.

[13] H. Kroemer, "Theory of a Wide-Gap Emitter for Transistors," *Proceedings of the IRE*, vol. 45, pp. 1535-1537, 1957.

[14] Z. I. Alferov and D. Z. Gabruzov, "Recombination radiation spectrum of GaAs with current excitation via p-n heterojunctions of GaP-GaAs, [English translation]," *Soviet Physics- Solid State*, vol. 7, pp. 1919, 1966.

[15] R. S. Friedman, M. C. McAlpine, D. S. Ricketts, D. Ham, and C. M. Lieber, "Nanotechnology High-speed integrated nanowire circuits," *Nature*, vol. 434, pp. 1085, 2005.

[16] P. Jarillo-Herrero, J. A. van Dam, and L. P. Kouwenhoven, "Quantum supercurrent transistors in carbon nanotubes," *Nature*, vol. 439, pp. 953-956, 2006.

[17] Y. Huang, X. Duan, Y. Cui, L. J. Lauhon, K.-H. Kim, and C. M. Lieber, "Logic Gates and Computation from Assembled Nanowire Building Blocks," *Science*, vol. 294, pp. 1313-1317, 2001.

[18] M. Law, D. J. Sirbuly, J. C. Johnson, J. Goldberger, R. J. Saykally, and P. Yang, "Nanoribbon Waveguides for Subwavelength Photonics Integration," *Science*, vol. 305, pp. 1269-1273, 2004.

[19] X. Wang, J. Zhuang, Q. Peng, and Y. Li, "A general strategy for nanocrystal synthesis," *Nature*, vol. 437, pp. 121-124, 2005.

[20] D. J. Milliron, S. M. Hughes, Y. Cui, L. Manna, J. Li, L.-W. Wang, and A. Paul Alivisatos, "Colloidal nanocrystal heterostructures with linear and branched topology," *Nature*, vol. 430, pp. 190-195, 2004.

[21] I. Gur, N. A. Fromer, M. L. Geier, and A. P. Alivisatos, "Air-Stable All-Inorganic Nanocrystal Solar Cells Processed from Solution," *Science*, vol. 310, pp. 462-465, 2005.

[22] D. V. Talapin and C. B. Murray, "PbSe Nanocrystal Solids for n- and p-Channel Thin Film Field-Effect Transistors," *Science*, vol. 310, pp. 86-89, 2005.

[23] T. Takagahara and K. Takeda, "Theory of the quantum confinement effect on excitons in quantum dots of indirect-gap materials," *Physical Review B*, vol. 46, pp. 15578 LP - 15581, 1992.

[24] H. I. Hanafi, S. Tiwari, and I. Khan, "Fast and long retention-time nano-crystal memory," *Electron Devices, IEEE Transactions on*, vol. 43, pp. 1553-1558, 1996.

[25] J. De Blauwe, "Nanocrystal nonvolatile memory devices," *Nanotechnology, IEEE Transactions on*, vol. 1, pp. 72-77, 2002.

[26] M. Wuttig and N. Yamada, "Phase-change materials for rewriteable data storage," *Nature Materials*, vol. 6, pp. 824-832, 2007.

[27] S. R. Ovshinsky, "Reversible Electrical Switching Phenomena in Disordered Structures," *Physical Review Letters*, vol. 21, pp. 1450 LP - 1453, 1968.

[28] S. Caravati, M. Bernasconi, T. D. Kuhne, M. Krack, and M. Parrinello, "Unravelling the Mechanism of Pressure Induced Amorphization of Phase Change Materials," *Physical Review Letters*, vol. 102, pp. 205502, 2009.

[29] K. Shportko, S. Kremers, M. Woda, D. Lencer, J. Robertson, and M. Wuttig, "Resonant bonding in crystalline phase-change materials," *Nature Materials*, vol. 7, pp. 653-658, 2008.

[30] C. Kim, D. Kang, T.-Y. Lee, K. H. P. Kim, Y.-S. Kang, J. Lee, S.-W. Nam, K.-B. Kim, and Y. Khang, "Direct evidence of phase separation in Ge[sub 2]Sb[sub 2]Te[sub 5] in phase change memory devices," *Applied Physics Letters*, vol. 94, pp. 193504, 2009.

[31] S. Raoux, H.-Y. Cheng, M. A. Caldwell, and H.-S. P. Wong, "Crystallization times of Ge--Te phase change materials as a function of composition," *Applied Physics Letters*, vol. 95, pp. 071910, 2009.

[32] E. Rutherford, "Retardation of the alpha particle from radium in passing through matter," *Philosophical Magazine Series 6*, vol. 12, pp. 134 - 146, 1906.

[33] W. Shockley, "Forming semiconductive devices by ionic bombardment." U.S. patent 2.787.564, 1954.

[34] G. W. Arnold and J. A. Borders, "Aggregation and migration of ion-implanted silver in lithia-alumina-silica glass," *Journal of Applied Physics*, vol. 48, pp. 1488-1496, 1977.

[35] J. F. Ziegler, J. P. Biersack, and U. Littmark, *The stopping and Range of Ions in Solids*. New York: Pergamon Press, 1985.

[36] *CRC Handbook of Chemistry and Physics*, 89 ed, 2008-2009.
[37] M. Fujii, S. Hayashi, and K. Yamamoto, "Growth of Ge microcrystals in SiO2 thin film matrices: a Raman and electron microscopic study," *Japanese Journal of Applied Physics*, vol. 30, pp. 687-694, 1991.
[38] Y. Maeda, "Visible photoluminescence from nanocrystallite Ge embedded in a glassy SiO2 matrix: Evidence in support of the quantum-confinement mechanism," *Physical Review B*, vol. 51, pp. 1658 LP - 1670, 1995.
[39] W. K. Choi, V. Ng, S. P. Ng, H. H. Thio, Z. X. Shen, and W. S. Li, "Raman characterization of germanium nanocrystals in amorphous silicon oxide films synthesized by rapid thermal annealing," *Journal of Applied Physics*, vol. 86, pp. 1398-1403, 1999.
[40] W. K. Choi, W. K. Chim, C. L. Heng, L. W. Teo, V. Ho, V. Ng, D. A. Antoniadis, and E. A. Fitzgerald, "Observation of memory effect in germanium nanocrystals embedded in an amorphous silicon oxide matrix of a metal-insulator- semiconductor structure," *Applied Physics Letters*, vol. 80, pp. 2014-2016, 2002.
[41] I. D. Sharp, Q. Xu, C. Y. Liao, D. O. Yi, J. W. Beeman, Z. Liliental-Weber, K. M. Yu, D. N. Zakharov, J. W. Ager, III, D. C. Chrzan, and E. E. Haller, "Stable, freestanding Ge nanocrystals," *Journal of Applied Physics*, vol. 97, pp. 124316, 2005.
[42] I. D. Sharp, "Structure and optical characterization of ion beam synthesized Ge nanocrystals," in *Department of materials science and engineering*: University of California, Berkeley, 2006.
[43] Q. Xu, "Synthesis and characterization of embedded Ge nanocrystals," in *Department of materials Science and Engineering*: University of California, Berkeley, 2006.
[44] H. Richter, Z. P. Wang, and L. Ley, "The one phonon Raman spectrum in microcrystalline silicon," *Solid State Communications*, vol. 39, pp. 625-629, 1981.
[45] I. H. Campbell and P. M. Fauchet, "The effects of microcrystal size and shape on the one phonon Raman spectra of crystalline semiconductors," *Solid State Communications*, vol. 58, pp. 739-741, 1986.
[46] S. Veprek, F.-A. Sarott, and Z. Iqbal, "Effect of grain boundaries on the Raman spectra, optical absorption, and elastic light scattering in nanometer-sized crystalline silicon," *Physical Review B*, vol. 36, pp. 3344 LP - 3350, 1987.
[47] G. Gouadec and P. Colomban, "Raman Spectroscopy of nanomaterials: How spectra relate to disorder, particle size and mechanical properties," *Progress in Crystal Growth and Characterization of Materials*, vol. 53, pp. 1-56, 2007.
[48] L. Ratke and P. W. Voorhees, *Growth and Coarsening*, 1st ed. ed. New York: Springer-Verlag, 2002.
[49] D. O. Yi, M. H. Jhon, I. D. Sharp, Q. Xu, C. W. Yuan, C. Y. Liao, J. W. Ager, E. E. Haller, and D. C. Chrzan, "Modeling nucleation and growth of encapsulated nanocrystals: Kinetic Monte Carlo simulations and rate theory," *Physical Review B*, vol. 78, 2008.
[50] C. W. Yuan, D. O. Yi, I. D. Sharp, S. J. Shin, C. Y. Liao, J. Guzman, J. W. Ager, E. E. Haller, and D. C. Chrzan, "Theory of Nanocluster Size Distributions from Ion Beam Synthesis," *Physical Review Letters*, vol. 102, 2009.
[51] N. Cowern and C. Rafferty, "Enhanced diffusion in silicon processing," *Mrs Bulletin*, vol. 25, pp. 39-44, 2000.
[52] C. W. Yuan, C. N. Boswell, S. J. Shin, C. Y. Liao, J. Guzman, J. W. Ager, E. E. Haller, and D. C. Chrzan, "Processing route for size distribution narrowing of ion beam synthesized nanoclusters," *Applied Physics Letters*, vol. 95, 2009.

[53] A. Meldrum, R. F. Haglund, L. A. Boatner, and C. W. White, "Nanocomposite materials formed by ion implantation," *Advanced Materials*, vol. 13, pp. 1431-+, 2001.

[54] P. Kluth, B. Hoy, B. Johannessen, S. G. Dunn, G. J. Foran, and M. C. Ridgway, "Co-Au core-shell nanocrystals formed by sequential ion implantation into SiO[sub 2]," *Applied Physics Letters*, vol. 89, pp. 153118, 2006.

[55] M. Strobel, K.-H. Heinig, and W. Moller, "Can core/shell nanocrystals be formed by sequential ion implantation? Predictions from kinetic lattice Monte Carlo simulations," *Nuclear Instruments and Methods in Physics Research Section B: Beam Interactions with Materials and Atoms*, vol. 148, pp. 104-109, 1999.

[56] C. W. Yuan, S. J. Shin, C. Y. Liao, J. Guzman, P. R. Stone, M. Watanabe, J. W. Ager, E. E. Haller, and D. C. Chrzan, "Structure map for embedded binary alloy nanocrystals," *Applied Physics Letters*, vol. 93, 2008.

[57] D. W. Jenkins and J. D. Dow, "Electronic properties of metastable GexSn1-x alloys," *Physical Review B*, vol. 36, pp. 7994 LP - 8000, 1987.

[58] G. He and H. A. Atwater, "Interband Transitions in SnxGe1-x Alloys," *Physical Review Letters*, vol. 79, pp. 1937 LP - 1940, 1997.

[59] V. R. D'Costa, C. S. Cook, A. G. Birdwell, C. L. Littler, M. Canonico, S. Zollner, J. Kouvetakis, and J. Menendez, "Optical critical points of thin-film Ge[sub 1 - y]Sn[sub y] alloys: A comparative Ge[sub 1 - y]Sn[sub y]/Ge[sub 1 - x]Si[sub x] study," *Physical Review B (Condensed Matter and Materials Physics)*, vol. 73, pp. 125207, 2006.

[60] Y. Nakamura, A. Masada, and M. Ichikawa, "Quantum-confinement effect in individual Ge[sub 1 - x]Sn[sub x] quantum dots on Si(111) substrates covered with ultrathin SiO[sub 2] films using scanning tunneling spectroscopy," *Applied Physics Letters*, vol. 91, pp. 013109, 2007.

[61] N. Naruse, Y. Mera, Y. Nakamura, M. Ichikawa, and K. Maeda, "Fourier-transform photoabsorption spectroscopy of quantum-confinement effects in individual GeSn nanodots," *Applied Physics Letters*, vol. 94, pp. 093104, 2009.

[62] D. B. Williams and C. B. Carters, *Transmission Electron Microscopy*. New York: Plenum Press, 1996.

[63] Q. Xu, I. D. Sharp, C. W. Yuan, D. O. Yi, C. Y. Liao, A. M. Glaeser, A. M. Minor, J. W. Beeman, M. C. Ridgway, P. Kluth, J. W. A. III, D. C. Chrzan, and E. E. Haller, "Large Melting-Point Hysteresis of Ge Nanocrystals Embedded in SiO[sub 2]," *Physical Review Letters*, vol. 97, pp. 155701, 2006.

[64] I. D. Sharp, D. O. Yi, Q. Xu, C. Y. Liao, J. W. Beeman, Z. Liliental-Weber, K. M. Yu, D. N. Zakharov, J. W. Ager, D. C. Chrzan, and E. E. Haller, "Mechanism of stress relaxation in Ge nanocrystals embedded in SiO ₂," *Applied Physics Letters*, vol. 86, pp. 63107, 2005.

[65] D. Lencer, M. Salinga, B. Grabowski, T. Hickel, J. Neugebauer, and M. Wuttig, "A map for phase-change materials," *Nature Materials*, vol. 7, pp. 972-977, 2008.

[66] S.-L. Wang, C.-Y. Chen, M.-K. Hsieh, W.-C. Lee, A. H. Kung, and L.-H. Peng, "Phase-change memory devices based on gallium-doped indium oxide," *Applied Physics Letters*, vol. 94, pp. 113503, 2009.

[67] F. Oki, Y. Ogawa, and Y. Fuyiki, "Effect of Deposited Metals on the Crystallization Temperature of Amorphous Germanium Film," *Japanese Journal of Applied Physics*, vol. 8, pp. 1056, 1969.

[68] S. R. Herd, P. Chaudhari, and M. H. Brodsky, "Metal contact induced crystallization in films of amorphous silicon and germanium," *Journal of Non-Crystalline Solids*, vol. 7, pp. 309-327, 1972.

[69] B. Ravel and M. Newville, "ATHENA, ARTEMIS, HEPHAESTUS: data analysis for X-ray absorption spectroscopy using IFEFFIT," *Journal of Synchrotron Radiation*, vol. 12, pp. 537-541, 2005.

[70] A. L. Ankudinov, B. Ravel, J. J. Rehr, and S. D. Conradson, "Real-space multiple-scattering calculation and interpretation of x-ray-absorption near-edge structure," *Physical Review B*, vol. 58, pp. 7565 LP - 7576, 1998.

[71] P. A. Temple and C. E. Hathaway, "Multiphonon Raman Spectrum of Silicon," *Physical Review B*, vol. 7, pp. 3685 LP - 3697, 1973.

[72] A. J. Williamson, C. Bostedt, T. vanBuuren, T. M. Willey, L. J. Terminello, G. Galli, and L. Pizzagalli, "Probing the Electronic Density of States of Germanium Nanoparticles: A Method for Determining Atomic Structure," *Nano Lett.*, vol. 4, pp. 1041-1045, 2004.

[73] G. V. M. Williams, A. Bittar, and H. J. Trodahl, "Crystallization and diffusion in progressively annealed a-Ge/SiO[sub x] superlattices," *Journal of Applied Physics*, vol. 67, pp. 1874-1878, 1990.

[74] T. J. Konno and R. Sinclair, "Crystallization of Silicon in Aluminum Amorphous-Silicon Multilayers," *Philosophical Magazine B*, vol. 66, pp. 749, 1992.

[75] Z. M. Wang, J. Y. Wang, L. P. H. Jeurgens, F. Phillipp, and E. J. Mittemeijer, "Origins of stress development during metal-induced crystallization and layer exchange: Annealing amorphous Ge/crystalline Al bilayers," *Acta Materialia*, vol. 56, pp. 5047-5057, 2008.

[76] O. Nast and A. J. Hartmann, "Influence of interface and Al structure on layer exchange during aluminum-induced crystallization of amorphous silicon," *Journal of Applied Physics*, vol. 88, pp. 716-724, 2000.

[77] F. Edelman, Y. Komem, M. Bendayan, and R. Beserman, "Initial crystallization stage of amorphous germanium films," *Journal of Applied Physics*, vol. 72, pp. 5153-5157, 1992.

[78] Z. Tan, S. M. Heald, M. Rapposch, C. E. Bouldin, and J. C. Woicik, "Gold-induced germanium crystallization," *Physical Review B*, vol. 46, pp. 9505 LP - 9510, 1992.

[79] G. Radnoczi, A. Robertsson, H. T. G. Hentzell, S. F. Gong, and M.-A. Hasan, "Al induced crystallization of a-Si," *Journal of Applied Physics*, vol. 69, pp. 6394-6399, 1991.

[80] J. M. Poate, J. Linnros, F. Priolo, D. C. Jacobson, J. L. Batstone, and M. O. Thompson, "Nonequilibrium segregation and trapping phenomena during ion-induced crystallization of amorphous Si," *Physical Review Letters*, vol. 60, pp. 1322 LP - 1325, 1988.

[81] C. M. Lieber, "Nanoscale science and technology : building a big future from small things," *MRS Bulletin*, vol. 28, pp. 486, 2003.

[82] A. Javey, "The 2008 Kavli Prize in Nanoscience: Carbon Nanotubes," *ACS Nano*, vol. 2, pp. 1329-1335, 2008.

[83] Z. L. Wang, "Nanostructures of zinc oxide," *Materials Today*, vol. 7, pp. 26-33, 2004.

[84] P. Yang, "The chemistry and physics of semiconductor nanowires," *MRS Bulletin*, vol. 30, pp. 85, 2005.

[85] J. C. Ho, R. Yerushalmi, Z. A. Jacobson, Z. Fan, R. L. Alley, and A. Javey, "Controlled nanoscale doping of semiconductors via molecular monolayers," *Nature Materials*, vol. 7, pp. 62-67, 2008.

[86] M. S. Gudiksen, L. J. Lauhon, J. Wang, D. C. Smith, and C. M. Lieber, "Growth of nanowire superlattice structures for nanoscale photonics and electronics," *Nature*, vol. 415, pp. 617-620, 2002.

[87] M. T. Bjork, B. J. Ohlsson, T. Sass, A. I. Persson, C. Thelander, M. H. Magnusson, K. Deppert, L. R. Wallenberg, and L. Samuelson, "One-dimensional Steeplechase for Electrons Realized," *Nano Letters*, vol. 2, pp. 87-89, 2002.

[88] H. Okamoto, "Reevaluation of Thermodynamic Models for Phase Diagram Evaluation," *Journal of phase equilibria*, vol. 12, pp. 623-643, 1991.

[89] D. Wang, R. Tu, L. Zhang, and H. Dai, "Deterministic One-to-One Synthesis of Germanium Nanowires and Individual Gold Nanoseed Patterning for Aligned Nanowire Arrays," *Angewandte Chemie International Edition*, vol. 44, pp. 2925-2929, 2005.

[90] N. Wang, Y. Cai, and R. Q. Zhang, "Growth of nanowires," *Materials Science and Engineering: R: Reports*, vol. 60, pp. 1-51, 2008.

[91] E. Sutter and P. Sutter, "Phase Diagram of Nanoscale Alloy Particles Used for Vapor-Liquid-Solid Growth of Semiconductor Nanowires," *Nano Letters*, vol. 8, pp. 411-414, 2008.

[92] J. von Borany, R. Grotzschel, K. H. Heinig, A. Markwitz, W. Matz, B. Schmidt, and W. Skorupa, "Multimodal impurity redistribution and nanocluster formation in Ge implanted silicon dioxide films," *Applied Physics Letters*, vol. 71, pp. 3215-17, 1997.

[93] T. Shimizu-Iwayama, D. E. Hole, and P. D. Townsend, "Optical properties of interacting Si nanoclusters in SiO2 fabricated by ion implantation and annealing," *Nuclear Instruments and Methods in Physics Research Section B: Beam Interactions with Materials and Atoms*, vol. 147, pp. 350-355, 1999.

[94] K. V. Shcheglov, C. M. Yang, K. J. Vahala, and H. A. Atwater, "Electroluminescence and photoluminescence of Ge-implanted Si/SiO[sub 2]/Si structures," *Applied Physics Letters*, vol. 66, pp. 745-747, 1995.

[95] Y.-C. King, T.-J. King, and C. Hu, "MOS memory using germanium nanocrystals formed by thermal oxidation of Si1-xGex," *International Electron Devices Meeting Technical Digest*, pp. 115-118, 1998.

[96] M. Fujii, O. Mamezaki, S. Hayashi, and K. Yamamoto, "Current transport properties of SiO[sub 2] films containing Ge nanocrystals," *Journal of Applied Physics*, vol. 83, pp. 1507-1512, 1998.

[97] A. Meldrum, K. S. Buchanan, A. Hryciw, and C. W. White, "Micropixelated Luminescent Nanocrystal Arrays Synthesized by Ion Implantation," *Advanced Materials*, vol. 16, pp. 31-34, 2004.

[98] K. Sun, S. Zhu, R. Fromknecht, G. Linker, and L. M. Wang, "Formation of single-layered Au nanoparticles in Au ion implanted TiO2 and SrTiO3," *Materials Letters*, vol. 58, pp. 547-550, 2004.

[99] I. Berbezier, A. Karmous, A. Ronda, T. Stoica, L. Vescan, R. Geurt, A. Olzierski, E. Tsoi, and A. G. Nassiopoulou, "Two-dimensional arrays of ordered, highly dense and ultra-small Ge nanocrystals on thin SiO2 layers," *Journal of Physics: Conference Series*, vol. 10, pp. 73-76, 2005.

[100] I. D. Sharp, Q. Xu, D. O. Yi, C. Y. Liao, J. W. Ager, J. W. Beeman, K. M. Yu, J. T. Robinson, O. D. Dubon, D. C. Chrzan, and E. E. Haller, "A Chemical Approach to 3-D Lithographic Patterning of Si and Ge Nanocrystals," presented at Materials Research Society, 2005.

[101] S. A. Nepijko, M. Klimenkov, H. Kuhlenbeck, and H.-J. Freund, "Transmission electron microscopy study of platinum clusters on Al[sub 2]O[sub 3]/NiAl(110) under the influence of electron irradiation," *Journal of Vacuum Science & Technology A: Vacuum, Surfaces, and Films*, vol. 17, pp. 577-583, 1999.

[102] G. Lulli, P. G. Merli, and M. V. Antisari, "Solid-phase epitaxy of amorphous silicon induced by electron irradiation at room temperature," *Physical Review B*, vol. 36, pp. 8038 LP - 8042, 1987.

[103] M. Klimenkov, W. Matz, and J. v Borany, "In situ observation of electron-beam-induced ripening of Ge clusters in thin SiO/sub 2/ layers," *Nuclear Instruments & Methods in Physics Research Section B-Beam Interactions with Materials & Atoms*, vol. 168, pp. 367-74, 2000.

[104] N. Jiang, J. Qiu, A. L. Gaeta, and J. Silcox, "Nanoscale modification of optical properties in Ge-doped SiO[sub 2] glass by electron-beam irradiation," *Applied Physics Letters*, vol. 80, pp. 2005-2007, 2002.

[105] G. S. Chen, C. B. Boothroyd, and C. J. Humphreys, "Novel fabrication method for nanometer-scale silicon dots and wires," *Applied Physics Letters*, vol. 62, pp. 1949-51, 1993.

[106] G. S. Chen, C. B. Boothroyd, and C. J. Humphreys, "Electron-beam-induced damage in amorphous SiO/sub 2/ and the direct fabrication of silicon nanostructures," *Philosophical Magazine A-Physics of Condensed Matter Defects & Mechanical Properties*, vol. 78, pp. 491-506, 1998.

[107] M. Takeguchi, R. Tanaka, and K. Furuya, "Fabrication and analysis of the nanometer-sized structure of silicon by ultrahigh vacuum field emission transmission electron microscope," presented at Elsevier. Applied Surface Science, vol.146, no.1-4, May 1999, pp.257-61. Netherlands., 1999.

[108] D. Xi-wen, M. Takeguchi, M. Tanaka, and K. Furuya, "Formation of crystalline Si nanodots in SiO/sub 2/ films by electron irradiation," *Applied Physics Letters*, vol. 82, pp. 1108-10, 2003.

[109] M. L. Knotek and P. J. Feibelman, "Stability of ionically bonded surfaces in ionizing environments," *Surface Science*, vol. 90, pp. 78-90, 1979.

[110] P. Nath, V. Dutta, and K. L. Chopra, "Effects of alloying on the transport properties of amorphous and crystalline Ge films," *Journal of Physics C: Solid State Physics*, vol. 12, pp. L203-L208, 1979.

[111] K. Alberi, J. Blacksberg, L. D. Bell, S. Nikzad, K. M. Yu, O. D. Dubon, and W. Walukiewicz, "Band anticrossing in highly mismatched Sn[sub x]Ge[sub 1 - x] semiconducting alloys," *Physical Review B (Condensed Matter and Materials Physics)*, vol. 77, pp. 073202, 2008.

[112] W. K. Chu, J. W. Mayer, and M. A. Nicolet, *Backscattering Spectrometry*. New York: Academic Press, 1978.

[113] M. Newville, "Fundamentals of XAFS." University of Chicago, 2004.

[114] D. C. Koningsberger and R. Prins, "Chemical Analysis," vol. 92: John Wiley & Sons, 1988.

[115] E. A. Stern, S. M. Heald, and E. E. Koch, "Handbook of Synchrotron Radiation," North-Holland, 1983, pp. 995-1014.

[116] J. Als-Nielsen and D. McMorrow, *Elements of Modern X-ray Physics*: John Wiley & Sons, 2001.